National Technical University of Athens

School of Mechanical Engineering

Fluids Section

Parallel CFD & Optimization Unit

# A Steady-State CFD Approach for the Prediction of Aerodynamically Induced Noise in Automotive HVAC Systems

Diploma Thesis

**Ioannis Chondromatidis**

Academic Supervisor:

K. C. Giannakoglou, Professor NTUA

Industrial Supervisor:

Antoine Delacroix, Senior Manager TME

Athens, 2024

# Acknowledgements

**National Technical University of Athens**
School of Mechanical Engineering
Parallel CFD & Optimization Unit

---

## A Steady-State CFD Approach for the Prediction of Aerodynamically Induced Noise in Automotive HVAC Systems

---

Diploma Thesis

**Ioannis Chondromatidis**

Academic Supervisor: K.C. Giannakoglou, Professor NTUA

Industrial Supervisor: Antoine Delacroix, Senior Manager TME

# Abstract

As the automotive industry pivots towards electric and hybrid vehicles to meet global sustainability objectives, a new era of innovation and transformation is underway. Consumer preferences increasingly prioritize vehicle comfort, prompting manufacturers to address vehicle noise, a critical factor influencing passenger satisfaction. Among the various sources of vehicle noise, Heating Ventilation and Air Conditioning (HVAC) systems stand out, particularly in Battery Electric Vehicles and Hybrid Electric Vehicles, where stationary conditions amplify HVAC noise in the absence of wind and road noise. Automotive manufacturers have recognized this challenge and have committed resources to advance HVAC duct systems.

The computational expense of Computational Aeroacoustics poses a significant challenge in accurately predicting noise generated by fluid flow. Numerical methods like Computational Fluid Dynamics require substantial computational resources and time due to the complexity of solving equations governing fluid dynamics and acoustics. Consequently, achieving timely and cost-effective predictions of noise emissions, particularly in complex engineering systems such as automotive HVAC ducts, remains challenging.

This diploma thesis endeavors to assess a cost-effective computational technique for predicting aerodynamically induced noise in automotive HVAC systems. Employing a steady-state CFD approach using OpenFOAM®, integrating the Reynolds – Averaged Navier Stokes equations and Proudman's acoustic analogy, offers computational efficiency by maintaining an acceptable prediction accuracy. Comparison of computed results with empirical data obtained from measurements enables validation. The thesis, organized into chapters encompassing airborne acoustics, CFD HVAC duct modelling, correlation with experimental data, and aeroacoustic design countermeasures analysis, reflects collaborative efforts between academia and industry.

A significant portion of this research was conducted during a six-month industrial placement at Toyota Motor Europe (TME) in Brussels, Belgium.

**Εθνικό Μετσόβιο Πολυτεχνείο**
Σχολή Μηχανολόγων Μηχανικών
Μονάδα Παράλληλης Υπολογιστικής Ρευστοδυναμικής & Βελτιστοποίησης

# Υπολογιστικό Μοντέλο βασισμένο σε Χρονικά Μόνιμες Εξισώσεις για την Πρόλεξη Αεροδυναμικά Επαγόμενου Θορύβου σε Συστήματα Κλιματισμού Αυτοκινήτων

Διπλωματική Εργασία

**Ιωάννης Χονδρωματίδης**

Ακαδημαϊκός Επιβλέπων: Κ.Χ. Γιαννάκογλου, Καθηγητής ΕΜΠ

Βιομηχανικός Επιβλέπων: Antoine Delacroix, Senior Manager TME

# Περίληψη

Καθώς η αυτοκινητοβιομηχανία στρέφεται προς τα ηλεκτρικά και υβριδικά οχήματα για να ανταποκριθεί στους παγκόσμιους στόχους βιωσιμότητας, μια νέα εποχή καινοτομίας και μετασχηματισμού είναι σε εξέλιξη. Οι προτιμήσεις των καταναλωτών δίνουν όλο και μεγαλύτερη έμφαση στην άνεση του οχήματος, γεγονός που οδηγεί τους κατασκευαστές σε ενέργειες για την αντιμετώπιση του επαγόμενου θορύβου. Ανάμεσα στις διάφορες πηγές θορύβου ενός οχήματος, τα συστήματα Θέρμανσης, Αερισμού και Κλιματισμού (HVAC) ξεχωρίζουν, ιδίως στα Αμιγώς Ηλεκτρικά και τα Υβριδικά Ηλεκτρικά Οχήματα, όπου ειδικά σε συνθήκες ακινησίας του οχήματος κυριαρχεί ο θόρυβος του συστήματος κλιματισμού σε απουσία εξωτερικών πηγών θορύβου. Οι αυτοκινητοβιομηχανίες έχουν αναγνωρίσει αυτήν την πρόκληση και αφιερώνουν πόρους για την εξέλιξη των συστημάτων κλιματισμού.

Το κόστος της Υπολογιστικής Αερακουστικής αντιπροσωπεύει ένα σημαντικό εμπόδιο στην ακριβή πρόλεξη του θορύβου που προκαλείται από τη ροή ρευστών. Οι παραδοσιακές αριθμητικές μέθοδοι όπως η Υπολογιστική Ρευστοδυναμική απαιτούν σημαντικούς υπολογιστικούς πόρους και, συνεπώς, χρόνο λόγω της πολυπλοκότητας της επίλυσης των εξισώσεων που διέπουν τη ροή των ρευστών και την ακουστική. Συνεπώς, η επίτευξη ορθών και οικονομικών προβλέψεων των εκπομπών θορύβου, ιδιαίτερα σε πολύπλοκα μηχανικά συστήματα όπως οι αγωγοί των αυτοκινήτων, παραμένει ιδιαίτερα απαιτητική.

Η διπλωματική εργασία έχει ως στόχο την ανάπτυξη μιας οικονομικής υπολογιστικής μεθόδου για την πρόλεξη του αεροδυναμικά επαγόμενου θορύβου στα συστήματα κλιματισμού επιβατικών αυτοκινήτων. Αναπτύσσεται ένας επιλύτης που χρησιμοποιεί χρονικά μόνιμες εξισώσεις ροής επιλυόμενες στο περιβάλλον του OpenFOAM®, που ενσωματώνει τις εξισώσεις Reynolds – Averaged Navier Stokes και την ακουστική αναλογία του Proudman, ελαχιστοποιώντας το υπολογιστικό κόστος χωρίς να θυσιάζεται η ακρίβεια των αποτελεσμάτων πέραν ενός αποδεκτού ορίου. Το μοντέλο επικυρώνεται από πειραματικά δεδομένα που λαμβάνονται από πραγματικές μετρήσεις. Τα κεφάλαια της εργασίας πραγματεύονται την αερακουστική θεμελίωση, τη μαθηματική μοντελοποίηση των εξισώσεων ροής, την υπολογιστική αντιμετώπιση των αγωγών, τη σύγκριση με πειραματικά δεδομένα και την αερακουστική ανάλυση σχεδιαστικών λύσεων, αντικατοπτρίζοντας έτσι την επίδραση της ακαδημαϊκής έρευνας στη βιομηχανία.

Μεγάλο τμήμα αυτής της έρευνας διεξήχθη κατά τη διάρκεια μιας εξαμηνιαίας βιομηχανικής πρακτικής άσκησης στην Toyota Motor Europe (TME) στις Βρυξέλλες, Βέλγιο.

# Table of Contents

# Abbreviations

**BEVs:** Battery Electric Vehicles

**CAA:** Computational Aeroacoustics

**CFD:** Computational Fluid Dynamics

**DFT:** Discrete Fourier Transform

**DNC:** Direct Noise Computation

**EVs:** Electric Vehicles

**FD:** Finite Differences

**FEM:** Finite Element Method

**FVM:** Finite Volume Method

**FW-H:** Ffowcs Williams – Hawkings

**HEVs:** Hybrid Electric Vehicles

**HVAC:** Heating Ventilation and Air-Conditioning

**KPI:** Key Performance Indicator

**LHS:** Left-Hand Side

**NIE:** Noise Index Estimation

**NTUA:** National Technical University of Athens

**OAPSD:** Overall Power Spectral Density

**OASPL:** Overall Sound Pressure Level

**PCOpt:** Parallel CFD & Optimization Unit

**PDE:** Partial Differential Equation

**PSD:** Power Spectral Density

**RANS:** Reynolds-Averaged Navier-Stokes

**RHS:** Right-Hand Side

**SPL:** Sound Pressure Level

**TKE:** Turbulent Kinetic Energy

**TME:** Toyota Motor Europe

**w.r.t.:** with respect to

# Chapter 1

# Introduction

In the field of automotive engineering, a prominent trend observed among car manufacturers is their unwavering commitment to enhancing efficiency and minimizing noise levels in their vehicles. Acknowledging the growing concerns surrounding environmental sustainability and driver comfort, manufacturers are directing their investments towards pioneering technologies and design methodologies to redefine the standards achievable on the road. Efficiency has emerged as a central focus for car manufacturers, spurred by a global emphasis on reducing carbon emissions and optimizing fuel consumption. Consequently, this drive has spurred the development of cutting-edge powertrain solutions, including hybrid and electric systems, as well as the integration of lightweight materials and aerodynamic refinements. These initiatives not only contribute to a more environmentally conscious footprint but also yield vehicles that are inherently more energy-efficient and economically viable in the long run.

Nevertheless, in today's automotive landscape, a new challenge has surfaced, particularly with the proliferation of hybrid and electric vehicles: the issue of induced noise. This challenge is particularly pronounced in such vehicles due to the absence of an internal combustion engine.

The concept of passenger fatigue induced by noise exposure is not a recent discovery. Landström [27] conducted experiments with drivers who operated vehicles for extended durations, ranging from 8 to 10 hours with a one-hour break, during which they were exposed to additional low-frequency sounds from car speakers for 5-minute intervals. The results indicated that theta waves, associated with heightened fatigue levels, were generally elevated during exposure to higher pressure levels (corresponding to higher acoustic power).

Moreover, an investigation of the relationship between sound frequency, power level (measured in dBA[1]), and the source of the sound was carried out [8]. The findings illustrated the widespread impact of noise-induced fatigue across various domains. Additionally, a 25% increase was observed in the risk of hypertension with a 5 dBA rise in aircraft noise exposure [55].

Other researchers [3] explored the effects of traffic noise exposure on coronary heart disease, concluding that environments with sound levels exceeding 65-70 dBA escalate the risk of heart disease and myocardial infarction by 10 to 50%. In a survey involving 6000 inhabitants around two military airbases in Japan, individuals exposed to noise levels of 70 dBA or higher displayed higher rates of mental instability [18].

Despite the abundance of evidence, it is essential to recognize that prolonged exposure to a noisy environment inevitably leads to mental fatigue. This is particularly significant in the context of global driving accidents. Increased mental fatigue is associated with physiological arousal,

---

[1] dBA is a modification of the dB scale that incorporates weighted frequencies to better reflect the sensitivity of the human ear. In general, more weight is applied at the frequency range of 500Hz to 10kHz.

decreased sensorimotor functions, and impaired information processing. This assertion is supported by an investigation of motorway accidents, which revealed the involvement of fatigued drivers in 11% of the incidents. Sleep or fatigue contributed to approximately 20% of fatal crashes involving trucks [16]. A comprehensive literature review covering both in-depth and questionnaire-based analyses, identified fatigue as a contributing factor in 15 to 20% of truck-related accidents [1].

## 1.1 Noise in Automotive Applications

In contemporary times, it is apparent that consumers increasingly consider the comfort level offered by a vehicle when making purchasing decisions. Consequently, the automotive sector is placing greater emphasis on addressing vehicle noise, given its substantial impact on passenger comfort.

To elaborate further, the primary sources of vehicle noise generation, as shown in **figure 1.1-1** can be categorized as follows:

1. Wind (or external aerodynamic) noise
2. Road noise
3. Powertrain noise
4. Heating Ventilation and Air Conditioning (HVAC) noise
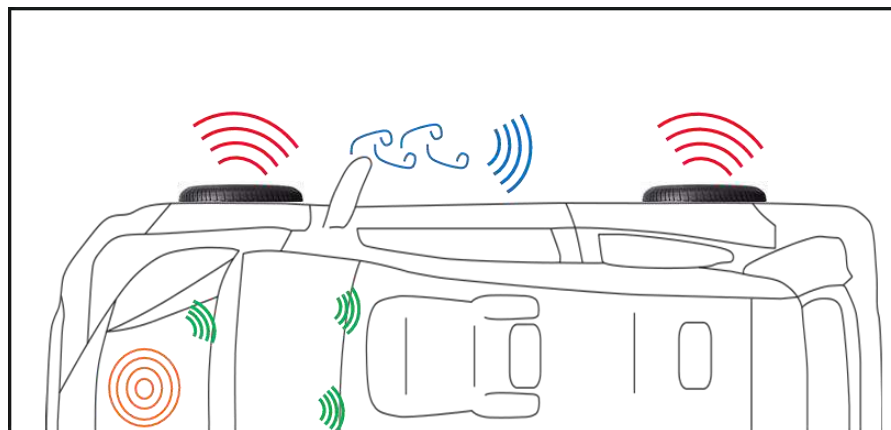


**Figure 1.1-1:** Generation of noise emissions in automotive applications. (Image claimed from TME).

This phenomenon is particularly pronounced in Battery Electric Vehicles (BEVs) and Hybrid Electric Vehicles (HEVs), wherein certain scenarios amplify the prominence of HVAC noise as the predominant source. This is attributed to the cessation of wind and road noise when the vehicle is stationary, as these noises are contingent upon vehicle motion (see **figure 1.1-2**). Moreover, in such vehicle types, powertrain noise is negligible or absent. Consequently, all automotive industries, including Toyota, have opted to allocate resources towards research, comprehension, and advancement of HVAC duct systems.
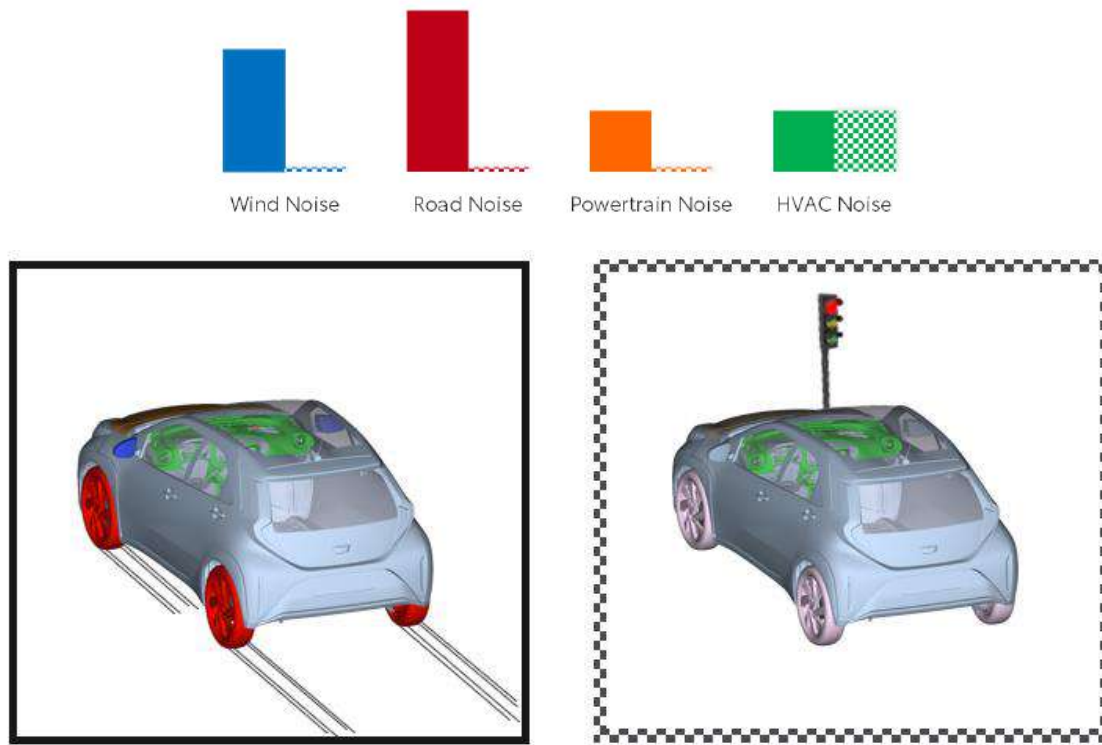
**Figure 1.1-2:** Noise source intensity comparison for BEVs and HEVs during motion (left) and stationary (right). Solid bars represent motion conditions, while checkered bars depict stationary conditions. (Image claimed from TME).

## 1.2   HVAC Aerodynamic Noise

HVAC noise comprises two distinct components: noise stemming from the rotating components, primarily the fan, and that from the stationary parts, consisting of the blower segment. Between these two, the first generates harmonic noise, which is generated by mechanical vibrations of components such as the blower motor, transmitted through solid parts and emitted as airborne sound, while the second induces aerodynamic noise, which is produced as a result of the airflow and its interactions with the solid boundaries (**figure 1.2-1**).
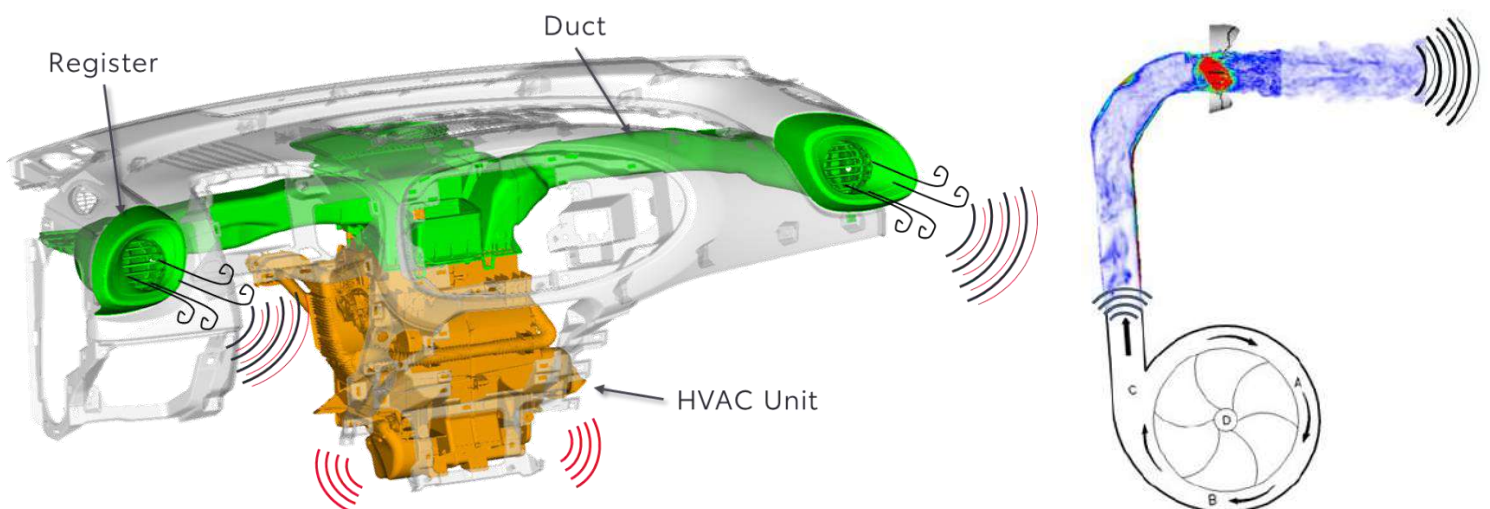


**Figure 1.2-1:** The assembly of the HVAC system consisting of the HVAC unit and the duct sub-assembly (left). Generation of aerodynamically induced noise inside the duct (right). (Image claimed from TME).

Given that the HVAC unit is typically sourced externally and undergoes infrequent updates, the point of emphasis is directed towards mitigating the noise from the stationary elements. However, space constraints necessitate a compact ducting system design, often characterized by sharp edges and sudden changes in cross-section. These design features significantly impact noise generation by inducing turbulent airflow structures.

The primary focus of this diploma thesis is the geometry of the HVAC duct illustrated in **figure 1.2-2**, situated within the driver's side instrument panel of a Toyota passenger vehicle. This system comprises the duct, which directs air from the central HVAC unit to the register. The register includes a rotating blade array designed to guide the airflow and regulate the flow rate. Given that other duct geometries were also analysed throughout this diploma thesis, this particular duct will hereafter be referred to as the "side-duct of car 1".



**Figure 1.2-2:** The blower assembly of side-duct of car 1 with its components.

# 1.3    HVAC Noise Index Estimation – Previous Work

For instance, as of May 2023, the established protocol within automotive companies such as Toyota Motor Europe (TME) for examining HVAC-induced noise is solely reliant on conducting experimental measurements within the vehicle cabin (**figure 1.3-1**). Regrettably, this approach lacks a simulation method capable of forecasting HVAC cabin noise. Consequently, the endeavor to create a quieter duct is burdened with heightened costs, prolonged timelines, and inefficiencies. Recognizing this challenge, there's a pressing need to pioneer the development of a simulation tool to address this gap, as such a tool would not only streamline the development process but also enhance the overall efficacy of noise reduction strategies within HVAC systems.
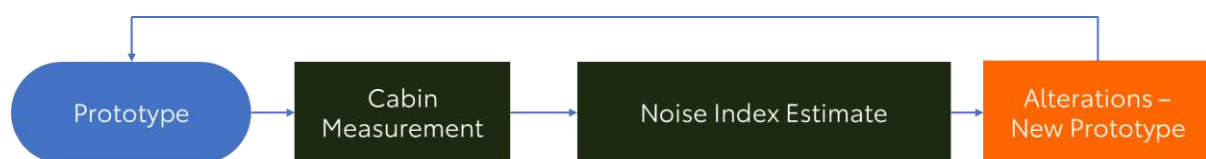


**Figure 1.3-1:** Flow chart of initial HVAC Noise Index Estimation Workflow.

Recognizing the aforementioned challenge, a proactive solution was devised, employing a direct computational approach grounded in compressible unsteady Computational Fluid Dynamics (CFD) [36]. This approach aims to simultaneously address both sound propagation and the underlying flow dynamics responsible for its generation within the same computational domain. The implementation leveraged the OpenFOAM® CFD toolbox along with custom Python™ utilities for post-processing the acoustic signals derived from unsteady CFD simulations, in the context of a diploma thesis [36]. It is pertinent to note that this diploma thesis serves as a continuation of this prior work, and thus, further elaboration on these aspects will be omitted in this section, as they will be recurrently referenced throughout the thesis.

The primary objective of this diploma thesis is to evaluate the efficacy of a cost-effective Computational AeroAcoustic (CAA) technique for predicting noise in automotive HVAC systems, while assessing the problematic accuracy of the CFD model of [36] in the high-frequency region. The aim is to develop a method capable of providing accurate predictions to guide the aeroacoustic design of HVAC ducts, with particular emphasis on aerodynamic noise originating from the flow within stationary HVAC components, all while adhering to time efficiency constraints. Within this framework, a steady-state CFD approach is conceptualized and subsequently implemented using OpenFOAM® [39], by numerically solving the Reynolds Averaged Navier Stokes (RANS) equations. The computed results are then juxtaposed with empirical data obtained from real-world measurements conducted through experimental setups.

The choice of a steady-state approach in this context is driven by several key considerations. By employing a steady-state methodology, the temporal terms in the governing equations are completely ignored, allowing the focus to be placed solely on the spatial distribution of the flow variables. This simplification leads to a significant reduction in computational cost and resource requirements. Consequently, the steady-state solvers used in this approach are computationally inexpensive, enabling faster convergence and reduced simulation times. Furthermore, this approach is well-suited for preliminary design and optimization stages, where multiple iterations and design variations need to be evaluated rapidly. By leveraging this approach, it becomes feasible for the engineer to conduct extensive parametric studies and sensitivity analyses, thereby guiding the design process effectively without incurring prohibitive computational costs, hence offering a balanced compromise between accuracy and computational efficiency.

## 1.4   The OpenFOAM® Software

The software used in this diploma thesis is OpenFOAM® (Open source Field Operation And Manipulation) [39]. It is an open-source software written in C++ programming language that has the ability to solve problems in parallel through the openMPI protocol, which is an implementation of the public domain MPI (Message Passing Interface) protocol [5]. It is a versatile tool that can simulate a wide range of fluid dynamics problems, including laminar and turbulent flows, multiphase flows, heat transfer, and chemical reactions. OpenFOAM® employs a finite volume method to solve the governing equations of fluid flow, providing the users with a wide range of solvers and models, including turbulence models, as well as pre- and post-processing tools for mesh generation, visualization, and data analysis.

## 1.5   Thesis Structure

The present text is structured as follows:

- ✓ Chapter 2: Introduction to airborne acoustics and its computational application in automotive contexts. The fundamental properties of sound transmission in the air are described, with emphasis in the effect of the unsteady flow character. Familiarization with the most widely used acoustic analogies and explanation of Proudman's analogy in the case of quadrupolic and dipolic noise.

- ✓ Chapter 3: Brief presentation of the Reynolds-Averaged Navier–Stokes equations and the $k - \varepsilon$ turbulence model employed in the context of the diploma thesis, with comments on the wall functions approach as a cost reduction mechanism. CFD modeling of the HVAC duct. Mesh generation, the definition of the boundary conditions and the selection of the discretization schemes in the OpenFOAM® environment are discussed.

- ✓ Chapter 4: Initial correlation of the steady-state CFD model with experimental data from previous studies. Elucidation of the primary differences between the unsteady and steady-state approaches regarding data processing, computational cost, identification of an effective comparison technique for CFD validation purposes and demonstration of the proof of concept for the Proudman's Acoustic Analogy model in the case of the HVAC duct.

- ✓ Chapter 5: Development of a noise source identification method able to visualize high acoustic power concentration both in the computational domain and in the surface of a given geometry. Aeroacoustic analysis of a design countermeasure proposed for noise reduction in a Toyota passenger car's side HVAC duct with the use of the steady-state CFD model. Performance prediction based on the validation of the model with previous experimental information.

- ✓ Chapter 6: Description of the experimental setup and noise measurement procedure for automotive blower performance evaluation, in the anechoic chamber. Presentation of the measured geometries and concise description of the model and microphones alignment for correct signal capturing. Subtraction of the background noise generated from the experimental assembly.

- ✓ Chapter 7: Post processing of the experimental measurements for CFD comparison compatibility. Investigation of the effect of various experimental sensitivity parameters in the quality of the results. Final correlation of the steady-state CFD model with new experimental measurements and evaluation of the design modification with real-life data.

- ✓ Chapter 8: Conclusions and suggestions for future research.

# Chapter 2:

# Aerodynamic Noise

Sound is defined as fluctuations in pressure within an elastic medium, induced by the vibration of a surface or turbulent fluid motion. It travels as longitudinal waves, characterized by alternating compressions and rarefactions within the medium. Working with air, these pressure oscillations occur above and below the atmospheric pressure, as depicted in **figure 2-1** [23].
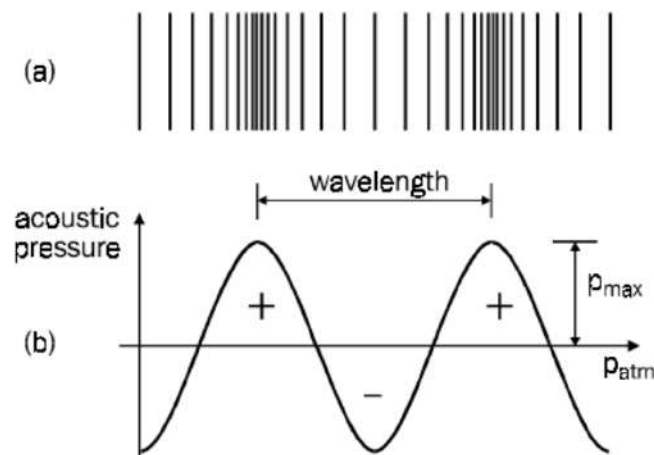


**Figure 2-1:** Representation of a sound wave. (a) Compressions and rarefactions caused in air by the sound wave. (b) Graphic representation of pressure variations above and below atmospheric pressure [23].

The term noise is used to describe any unwanted or undesirable sound that interferes with normal activities or causes discomfort or annoyance.

Aerodynamic noise, also known as aeroacoustic noise, is defined as the noise caused by the motion of gases or air, in particular. It is specifically concerned with the study of sound resulting from the interaction between the airflow and solid surfaces, typically in the context of aerodynamic or fluid dynamic systems.

A flow field that includes sound propagation can be interpreted as a superposition of an acoustic disturbance field $(p', \rho')$ to an ambient state, which is the undisturbed flow state $(p_0, \rho_0, T_0, u_0)$ (i.e. in the absence of said disturbances) [43].

$$p = p_0 + p', \rho = \rho_0 + \rho' \qquad (2\text{-}1)$$

The equation that describes the propagation of acoustic waves, in a uniform medium, assuming isentropic propagation [13] and adopting the acoustic linearization approximation, is the linear wave equation [23]. It can be derived from the linearization of the Euler or the Navier-Stokes equations.

$$\frac{\partial^2 p'}{\partial x_i^2} - \frac{1}{c^2}\frac{\partial^2 p'}{\partial t^2} = 0 \qquad (2\text{-}2a)$$

$$p' = c^2 \rho', c^2 = \left(\frac{\partial p}{\partial \rho}\right)_0 \qquad (2\text{-}2b)$$

The speed of sound is defined as the partial derivative of pressure w.r.t. density, at ambient conditions.

## 2.1 Lighthill's Acoustic Analogy

In acoustics, an analogy is a theoretical framework that simplifies the problem of sound generation and propagation by relating the sound field to source terms derived from fluid dynamic equations. This approach leverages established fluid dynamic principles to study acoustic phenomena, facilitating predictions of noise generated by turbulent flows. Unlike direct computation, which involves solving the full set of governing equations through detailed numerical simulations, an acoustic analogy infers solutions by drawing parallels between complex acoustic problems and more familiar fluid dynamic systems. This methodology reduces computational complexity and provides valuable insights based on fluid dynamics theories.

Lighthill's Acoustic Analogy [30] establishes a direct link between fluid flow fluctuations and resulting acoustic emissions. It suggests that aerodynamic noise stems from converting kinetic energy within the fluid flow into acoustic energy due to turbulent fluctuations. This process assumes turbulent eddies as the primary source of noise generation, manifesting as fluctuating volume accelerations.

The core principle of Lighthill's Analogy involves decomposing fluid flow into mean and fluctuating components. The mean flow signifies the steady fluid motion, while the fluctuating component represents turbulent variations overlaid on the mean flow.

According to this model, turbulent eddies' fluctuating volume acceleration serves as a distributed sound source in the fluid medium. Mathematically, this source term is derived from the product of fluctuating velocity and the gradient of mean flow velocity [30].

$$\frac{\partial^2 \rho'}{\partial t^2} - c_\infty^2 \frac{\partial^2 \rho'}{\partial x_j^2} = \frac{\partial^2 T_{ij}}{\partial x_i \partial x_j} \qquad (2.1\text{-}1)$$

The RHS in the above expression consists of the spatial derivatives of the Lighthill tensor, defined as

$$T_{ij} = \rho v_i v_j + (p - p_\infty) - (\rho - \rho_\infty)c_\infty^2 \delta_{ij} - \sigma_{ij} \qquad (2.1\text{-}2)$$

where $\delta_{ij}$ denotes the Kronecker delta, $\sigma_{ij}$ the viscous stress tensor and $v_i$ the ith component of the velocity field.

**Equation 2.1-1** can be written in integral form, by integrating over the volume $V$ containing the sound sources:

$$\rho'(\boldsymbol{x}, t) = \frac{1}{4\pi c_\infty^2} \int_V \frac{\partial^2 T_{ij}}{\partial x_i \partial x_j} \frac{1}{|\boldsymbol{x} - \boldsymbol{y}|} dy \qquad (2.1\text{-}3)$$

Lighthill's tensor models aeroacoustic phenomena such as:

- ✓ **Turbulent shear layers**, similar to those occurring at the boundaries of separated flow regions or around bluff bodies, which generate intense fluctuations in volume acceleration, contributing to aerodynamic noise production.
- ✓ **Vortex Shedding** behind blunt bodies or within wake flows that induce fluctuating velocity gradients and pressure fluctuations, leading to the emission of sound waves.
- ✓ **Wake Turbulence** behind moving objects.

## 2.2 Curle's Acoustic Analogy

Curle's Acoustic Analogy, pioneered by John Curle during the mid-20th century, offers an alternative framework for comprehending the origins of aerodynamic noise [10]. A notable distinction between Curle's approach and Lighthill's lies in their focal points regarding noise generation mechanisms. Curle's analogy places heightened significance on the direct impact of surface sources, including vortices emitted from solid boundaries or discontinuities within the flow field.

Furthermore, a prominent variance emerges in the mathematical depiction of acoustic sources. While Lighthill's Analogy attributes sound generation primarily to the fluctuating volume acceleration linked with turbulent eddies, represented through Lighthill's stress tensor, Curle's approach adopts surface-based singularities such as vortex sheets or compact sources. These singularities are incorporated directly into the governing equations to illustrate the acoustic sources, and their influence is localized to specific regions within the flow, directly interacting with the acoustic field.

The acoustic density fluctuations at location $\boldsymbol{x}$ and time $t$, owing to a flow field $p, u_i, \rho$ can be calculated using

$$
\begin{aligned}
\rho'(\boldsymbol{x}, t)c_\infty^2 = &\iint_S \left[\frac{\partial(\rho v_j)}{\partial \tau}\right]_{\tau=\tau^*} \frac{n_j}{4\pi|\boldsymbol{x} - \boldsymbol{y}|} dS(\boldsymbol{y}) - \\
&- \frac{\partial}{\partial x_i} \iint_S \left[p_{ij} + \rho v_i v_j\right]_{\tau=\tau^*} \frac{n_j}{4\pi|\boldsymbol{x} - \boldsymbol{y}|} dS(\boldsymbol{y}) + \\
&+ \frac{\partial^2}{\partial x_i \partial x_j} \iiint_V \left[T_{ij}(\boldsymbol{y}, \tau)\right]_{\tau=\tau^*} \frac{1}{4\pi|\boldsymbol{x} - \boldsymbol{y}|} dV(\boldsymbol{y})
\end{aligned}
\qquad (2.2\text{-}1)
$$

The stationary integration volume $V$ comprises the region where sound is generated by the flow, while $S$ encompasses all solid boundaries within $V$ and includes the external boundary of $V$, if present. The outward normal vector $\boldsymbol{n}$ pertains to surface $S$ and the stress tensor is expressed as $p_{ij} = (p - p_\infty)\delta_{ij} - \sigma_{ij}$. Notably, the integrals in **equation 2.2-1** are calculated w.r.t. vector $\boldsymbol{y}$ inside the volume $V$, at the retarded time $\tau = \tau^* = t - \frac{|x-y|}{c_\infty}$. This time discrepancy between $t$

and $\tau$ represents the duration for an acoustic disturbance generated at location $\boldsymbol{y}$ to propagate to the receiver $\boldsymbol{x}$.

Curle's analogy, as expressed in **equation 2.2-1**, is derived under the assumption of a direct line of sight between every point within volume $V$ and the receiver location $\boldsymbol{x}$, neglecting any indirect sound paths due to scattering effects [12]. However, in scenarios involving more intricate geometries where these assumptions are not applicable, alternative formulations [32], [33], [34], [35] employing Green's functions [12], [15], [56] can be utilized. It should be noted that this limitation, stemming from the assumption of a direct line of sight, represents a significant drawback of Curle's acoustic analogy.

However, both Lighthill's and Curle's analogies have the significant disadvantage of the temporal derivative terms, which require an unsteady solution and, therefore, massively increase the computational time.

## 2.3 Ffowcs Williams – Hawkings Acoustic Analogy

The FW-H acoustic analogy involves enclosing the sound sources with a control surface that is mathematically represented by a function, $f(x, t) = 0$. The acoustic signature at any observer position can be obtained from the FW-H equation [2]:

$$p'(\boldsymbol{x}, t) = \frac{\partial}{\partial t} \int_{f=0} \left[ \frac{Q_i n_i}{4\pi |\boldsymbol{x} - \boldsymbol{y}|} \right]\Bigg|_{\tau_e} dS -$$

$$-\frac{\partial}{\partial x_i} \int_{f=0} \left[ \frac{L_{ij} n_j}{4\pi |\boldsymbol{x} - \boldsymbol{y}|} \right]\Bigg|_{\tau_e} dS + \frac{\partial^2}{\partial x_i \partial x_j} \int_{f>0} \left[ \frac{T_{ij}}{4\pi |\boldsymbol{x} - \boldsymbol{y}|} \right]\Bigg|_{\tau_e} dV \qquad (2.3\text{-}1)$$

where $|_{\tau_e}$ denotes evaluation at the emission time $\tau_e$ and $V$ represents the volume outside the control surface. The source terms under the integral sign are:

$$Q_i = \rho(u_i - v_i) + \rho_0 v_i \qquad (2.3\text{-}2)$$

$$L_{ij} = \rho u_i (u_j - v_j) + P_{ij} \qquad (2.3\text{-}3)$$

The vectors $\boldsymbol{u}$ and $\boldsymbol{v}$ are the flow and the surface velocities, respectively. The compression tensor $P_{ij}$ is defined as:

$$P_{ij} = (p - p_0)\delta_{ij} - \sigma_{ij} \qquad (2.3\text{-}4)$$

The three source terms in the formal definition of $p'(x, t)$ are known as the thickness ($Q_i$, monopole), loading ($L_{ij}$, dipole) and quadrupole ($T_{ij}$) source terms, respectively.

The FW-H acoustic analogy is used in applications involving axisymmetric intake geometries with a spatially repetitive pressure distribution at the inlet. There, the 3D steady flow equations can be solved in a rotating frame of reference close to the bodies [37].

The use of the FW–H analogy requires, though, unsteady flow fields. These are generated by rotating the computed steady (in the rotating frame) flow fields, i.e., through a transformation to the absolute frame [37]. As a result, the computational cost increases significantly, therefore the use of this model in steady flow applications is not suggested.

While other acoustic analogies exist, they were not pertinent to the scope of this diploma thesis. Nevertheless, they are acknowledged for completeness. Among these are Phillips' acoustic analogy [42] and Goldstein's generalized acoustic analogy [14].

## 2.4 Categorization of Noise Sources

The three right-hand-side terms of **equation 2.2-1** are considered as different aeroacoustic noise sources and are often classified based on their radiation characteristics into monopole, dipole, and quadrupole sources, each representing distinct mechanisms of sound generation. Monopole sources, which emit sound equally in all directions, are primarily dependent on variations in the mass flux $\rho u_j n_j$ [12]. Examples of monopole sources in aerodynamics include vibrating surfaces and exhaust pipes, where the rapid alternation of volumetric flow leads to isotropic sound waves [11].

Dipole sources depend on the loading of, and the convected momentum through, surface $S$ $\left(p_{ij} + \rho v_i v_j\right)$. In areas where surface $S$ expresses solid boundaries, term $\rho v_i v_j n_j$ vanishes thus rendering the fluid – solid force the only contributor. Dipole noise sources thus arise in areas where time – varying forces are applied on solid boundaries, such as turbulent wall interactions [11]. They are characterized by the cancellation of sound radiation in one direction due to the opposing phases of two closely spaced sources and are often associated with the shedding of vortices from bluff bodies. The alternating vorticity of shedding vortices creates pressure fluctuations, resulting in preferential sound radiation perpendicular to the flow direction [40]. By employing the chain rule for the spatial derivative appearing in the second term

$$\frac{\partial f(\tau^*)}{\partial x_i} = \frac{\partial \tau^*}{\partial x_i}\left[\frac{\partial f(\tau)}{\partial \tau}\right]_{\tau=\tau^*} \tag{2.4-1}$$

and given that $\tau^* = t - \frac{|x-y|}{c_\infty}$,

$$\frac{\partial \tau^*}{\partial x_i} = -\frac{(x_i - y_i)}{|x - y|c_\infty} \tag{2.4-2}$$

When the sound-generating region is acoustically compact, meaning that the distance between any two points in that region is negligible compared to their distance to the observer, the terms

$(x_i - y_i)$ and $|x - y|$ can be approximated as $x_i$ and $|x|$ respectively, yielding an alternative, simplified form, of the dipole contribution:

$$(\rho'(x,t)c_\infty^2)_{dipole} \approx \frac{x_i}{4\pi|x|^2 c_\infty} \iint_S \left[\frac{\partial p_{ij}n_j}{\partial \tau}\right]_{\tau=\tau^*} dS(y) \qquad (2.4\text{-}3)$$

The above expression indicates that dipole noise is exclusively attributed to variations in the net surface force $p_{ij}n_j$, encompassing both isotropic pressure and viscous stresses.

Quadrupole sound sources involve the interaction of four monopole sources arranged in specific configurations and appear in areas of intense shear in fluids, such as in the case of a jet, discharging into an otherwise quiescent fluid [11]. They rely on fluctuating stresses in the shear layer, arising from turbulent mixing of fluid regions with greatly different velocities [11], [56]. Once again, a similar relation can be derived for the quadrupole contribution:

$$(\rho'(x,t)c_\infty^2)_{quadrupole} \approx \frac{x_i x_j}{4\pi|x|^3 c_\infty} \iiint_V \left[\frac{\partial^2 T_{ij}}{\partial \tau^2}\right]_{\tau=\tau^*} dV(y) \qquad (2.4\text{-}4)$$

where $T_{ij}$ stands for the Lighthill stress tensor. Lighthill [30] showed that in the case of negligible heat transfer within the flow, the stress tensor is equal to

$$T_{ij} = \rho v_i v_j + \mathcal{O}(M^2) \qquad (2.4\text{-}5)$$

The latter is of great importance, as it states that for low Mach number applications the approximation of $T_{ij} = \rho v_i v_j$ is sufficient. Moreover, Curle [10] showcased that the ratio of acoustic intensities of quadrupolar to dipolar noise generated by turbulence near solid bodies, follows roughly

$$\frac{I_{quadrupole}}{I_{dipole}} \propto \left(\frac{U}{c_\infty}\right)^2 = M^2 \qquad (2.4\text{-}6)$$

Therefore, in low Mach number flows in the presence of solid boundaries, the contribution of dipole sources is much more dominant than those of the quadrupole ones. In the context of the diploma thesis, the effect of these two sources in the accuracy of the computations is separately examined.

## 2.5 Proudman's Acoustic Analogy

Building on the work of Lighthill [30], Proudman [46] derived analytical expressions to approximate the sound intensity of homogenous, isotropic turbulence for low Mach numbers in terms of the kinetic energy of the Turbulent Kinetic Energy (TKE) and its dissipation rate. It should be noted that in a long, straight section of an HVAC duct with fully developed turbulence, the latter may approach isotropy in the core region of the flow, away from the walls. This is because, in fully developed turbulence, the energy distribution among different scales can become more uniform. Additionally, according to Kolmogorov's hypothesis [24], at sufficiently small scales (in the inertial subrange), turbulence tends to become isotropic regardless of the larger-scale anisotropy.

According to this analogy, the rate of change of momentum in the flow field is related to the rate of acoustic power radiated into the surrounding medium [46]. By integrating **equation 2.1-1**, the acoustic power can be expressed as:

$$P(\boldsymbol{x}, t) = \frac{1}{4\pi} \int_V \left[ \frac{\partial}{\partial t} \left( \rho u_i u_j \right) - \frac{\partial}{\partial x_i} \left( p_{ij} + \rho u_i u_j \right) + \frac{\partial^2}{\partial x_i \partial x_j} T_{ij} \right] \frac{1}{|\boldsymbol{x} - \boldsymbol{y}|} dV(\boldsymbol{y}) \qquad (2.5\text{-}1)$$

According to Proudman's analogy, the acoustic intensity resulting from flow-induced phenomena can be represented using the conventional steady-state variables of turbulent kinetic energy (TKE), $k$, and dissipation rate, $\varepsilon$, commonly employed in CFD. This method offers a notable advantage as it allows for the estimation of flow-induced noise using steady-state CFD, making approaches based on Proudman's analogy significantly more computationally efficient compared to those relying on Lighthill's analogy. The computational efficacy of flow noise predictions utilizing Proudman's analogy renders the technique highly appealing for comparative design investigations [9]. However, it should be noted that without an unsteady solution, the frequency spectrum cannot be obtained and therefore tonal noise is not detectable.

The sources of flow noise can be represented as the sum of volume and surface components as follows:

$$P = P_s + P_V = \int_S p_s(\boldsymbol{y}_b) dS + \int_V p_V(\boldsymbol{y}) dV \qquad (2.5\text{-}2)$$

where $P$ is the total acoustic power generated by the flow. $p_s(\boldsymbol{y}_b)$ and $p_v(\boldsymbol{y})$ are respectively the surface component (dipole) and volume component (quadrupole). $\boldsymbol{y}$ and $\boldsymbol{y}_b$ are the position vectors of the volumetric and surface source points, respectively. Esimates for $p_s$ and $p_v$ can be given as:

$$p_V(\boldsymbol{y}) = A\rho\varepsilon(\boldsymbol{y}) \left( \frac{\sqrt{k(\boldsymbol{y})}}{c} \right)^5 \qquad (2.5\text{-}3a)$$

$$p_s(\boldsymbol{y}_b) = B\rho \left(\frac{k_0(\boldsymbol{y}_b)}{c}\right)^3 \tag{2.5-3b}$$

where $c$ is the speed of sound and $\rho$ is the fluid density. $k(\boldsymbol{y})$ and $\varepsilon(\boldsymbol{y})$ are the turbulent kinetic energy and dissipation rate at $\boldsymbol{y}$, respectively. $k_0(\boldsymbol{y}_b)$ is the kinetic energy of the fluctuating component of the friction velocity evaluated at $\boldsymbol{y}_b$. $A, B$ are constants to be determined by model calibrations. The expression for $p_V(\boldsymbol{y})$ comes from the work of Proudman [46] on the noise generated by isotropic turbulence. $p_V(\boldsymbol{y})$ is readily computed using the values for $k$ and $\varepsilon$ from the outcome of the CFD run. From the aforementioned, it becomes evident that a two-equation turbulence model needs to be employed. The expression for $p_s(\boldsymbol{y}_b)$ is derived from the scaling laws of aerodynamic noise and recognising that it corresponds to a dipole noise source, as presented by Skvortsov et al. [51].

In the standard $k - \varepsilon$ turbulence model of Launder and Spalding [29] the relationship between the turbulent shear stress $\tau$ and $k$ is:

$$\tau_w = \rho \sqrt{C_\mu k} \tag{2.5-4}$$

where $C_\mu$ is a constant coefficient of the turbulence model. Using this relationship, $k_0$ is defined as:

$$k_0(\boldsymbol{y}_b) = \frac{\tau_{t_0}(\boldsymbol{y}_b)}{\rho\sqrt{C_\mu}} \tag{2.5-5}$$

$\tau_{t_0}(\boldsymbol{y}_b)$ is the fluctuating component of the wall shear stress at $\boldsymbol{y}_b$ and is defined as:

$$\tau_{t_0}(\boldsymbol{y}_b) = \tau_0(\boldsymbol{y}_b)\frac{\nu_t}{\nu} \tag{2.5-6}$$

where $\tau_0(\boldsymbol{y}_b)$ is the mean wall shear stress at $\boldsymbol{y}_b$, $\nu$ is the kinematic viscosity of the fluid and $\nu_t$ is the turbulent kinematic viscosity and is taken from the computational cell adjacent to the wall. Hence, a final expression for $k_0(\boldsymbol{y}_b)$ is given by:

$$k_0(\boldsymbol{y}_b) = \tau_0(\boldsymbol{y}_b)\frac{\nu_t}{\rho\nu\sqrt{C_\mu}} \tag{2.5-7}$$

All quantities on the right-hand-side of **equation 2.5-6** can readily be obtained from a steady-state CFD analysis, therefore reducing the computational demands.

## 2.6 Brief Description of Direct Noise Computation

Since this diploma thesis builds upon the work of [36], which was conducted as a part of another diploma thesis in the PCOpt of NTUA, a concise overview of the CFD model utilized in this research will be provided.

In general, Direct Noise Computation (DNC) is a method predicting both the aerodynamic/hydrodynamic and the acoustic field simultaneously, by directly solving the unsteady compressible Navier – Stokes equations [4], [56]. In DNC, both the flow mechanisms responsible for sound generation and the propagating perturbations of pressure and density that make-up sound are resolved simultaneously, using CFD, in the same computational domain. The necessity for a compressible CFD formulation is dictated by the nature of sound since it's expressed by perturbations in the pressure and density fields [36] (see **figure 2.6-1**).
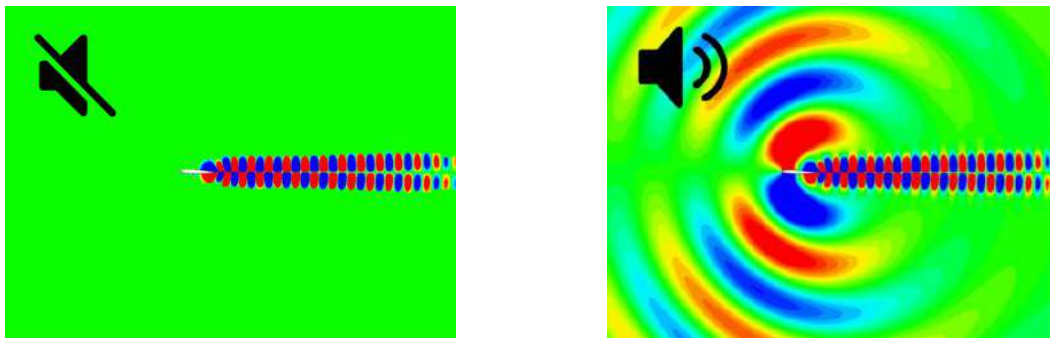


**Figure 2.6-1:** Propagation of a sound wave. Incompressible CFD model – absence of wave propagation (left). Compressible CFD model – formation of acoustic waves (right) [47]. The necessity for a compressible CFD approach for sound wave capturing.

DNC is considered the most accurate method up to date, since it does not rely on any model for sound capturing, except in some cases a turbulence model for the flow [56].

Although the DNC is the only method that can directly compute the induced noise, it has a significant drawback: When compared to other CFD applications, such as any acoustic analogy, it tends to be very computationally demanding. In particular, the aeroacoustic simulation of a typical HVAC duct, for a time step of $2 \cdot 10^{-5}$ sec, requires approximately 4 days on 512 processors based on the work of [36] (see **figure 2.6-2**). Especially if someone takes into consideration that the design of a part is an iterative process, the total computational and time cost become non – affordable.
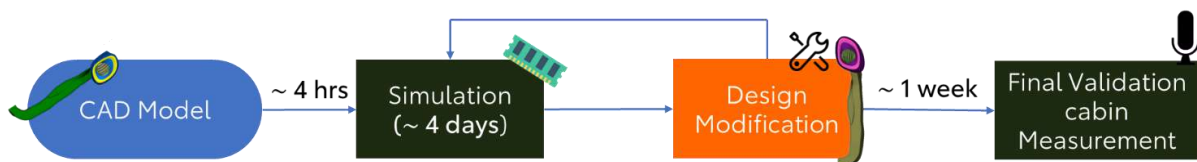


**Figure 2.6-2:** Typical workflow for the aeroacoustic development of an HVAC duct.

As a result, the need for the development of a viable, lower cost CFD model, yet with sufficient accuracy, becomes necessary. Therefore, a steady-state, incompressible CFD model utilizing the RANS equations and Proudman's acoustic analogy was developed, managing to significantly reduce run time from approximately 4 days to just 1.5 hour on 512 CPUs, while maintaining accuracy within 4% compared to experimental measurements.

# Chapter 3:

# CFD Modeling

## 3.1 The Navier – Stokes Equations for Incompressible Flows

The Navier – Stokes equations are a set of highly complex non – linear partial differential equations that describe the motion of a fluid in a continuous medium. For incompressible fluid flow problems, they consist of the conservation of mass and momentum.

### 3.1-1 Continuity Equation

The continuity equation describes the conservation of mass in a fluid flow. It states that the rate of change of mass within a control volume must be equal to the net mass flux across the control volume's boundaries. Mathematically, the continuity equation for incompressible flows is expressed as [60]:

$$\nabla \cdot \boldsymbol{u} = \frac{\partial u}{\partial x} + \frac{\partial v}{\partial y} + \frac{\partial w}{\partial z} = 0 \qquad (3.1\text{-}1)$$

### 3.1-2 Conservation of Momentum

The conservation of momentum, which is equivalent to Newton's second law, states that the total momentum of a system remains constant unless acted upon by external forces. For incompressible turbulent flows, the conservation of momentum is expressed as [26]:

$$u_j \frac{\partial u_i}{\partial x_j} = -\frac{\partial p}{\partial x_i} + \frac{\partial}{\partial x_j}\left[\nu\left(\frac{\partial u_i}{\partial x_j} + \frac{\partial u_j}{\partial x_i}\right)\right] \qquad (3.1\text{-}2)$$

where $p$ is the pressure divided by the fluid's density, $\nu$ is the fluid's kinematic viscosity and $\nu_t$ is the fluid's turbulent kinematic viscosity.

## 3.2 The RANS (Reynolds Averaged Navier – Stokes) Equations

The Reynolds-averaging method depends on the decomposition of each instant independent variable $f(x, y, z, t)$ of the problem to a sum of its time averaged value $\bar{f}(x, y, z)$ and its fluctuation $f'(x, y, z)$, as seen in **figure 3.2-1**. The time-averaged value of the fluctuations $\bar{f'} = 0$ [45]. The independent velocity and pressure variables are expressed as:

$$u_i = \bar{u}_i + u_i' \tag{3.2-1}$$
$$p = \bar{p} + p' \tag{3.2-2}$$

So, for incompressible flows, the conservation of momentum equation according to Reynolds is transformed to [45]:

$$\bar{u}_j \frac{\partial \bar{u}_i}{\partial x_j} = \frac{\partial}{\partial x_j}\left[-\bar{p}\delta_{ij} + v\left(\frac{\partial \bar{u}_i}{\partial x_j} + \frac{\partial \bar{u}_j}{\partial x_i}\right) - \overline{u'_i u'_j}\right] \tag{3.2-3}$$

where $\delta_{ij} = \begin{cases} 1 & i = j \\ 0 & i \neq j \end{cases}$ is the delta Kronecker [61].
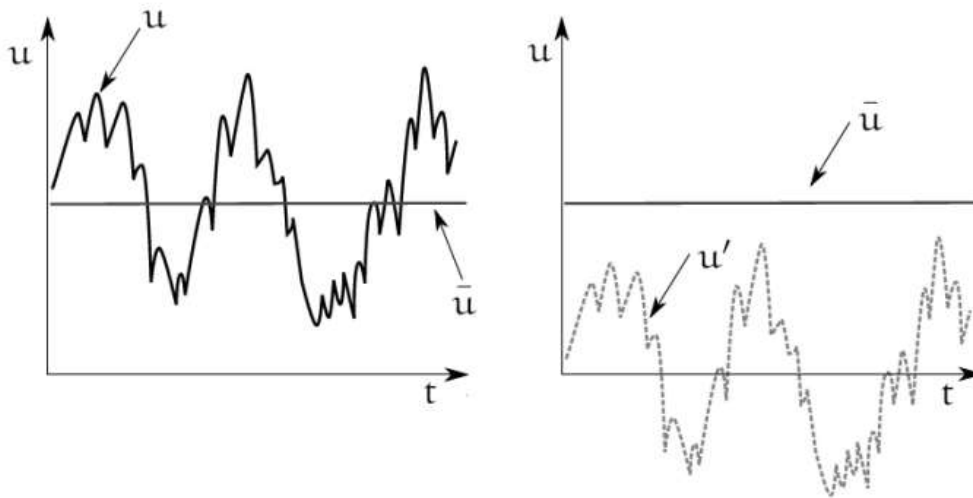


**Figure 3.2-1:** Instantaneous velocity consisting of the average value $\bar{u}$ and the disturbance $u'$. On the right – hand side, $\bar{u}' = 0$.

During the time – averaging of the conservation of momentum equation, an additional term called the Reynolds stress represented as $-\overline{u'_i u'_j}$ emerges. This term is modeled following the Boussinesq hypothesis, which postulates that the fluctuations in density due to turbulence are negligibly small compared to the mean density, and hence can be disregarded except for their contribution to the Reynolds stress. This hypothesis simplifies the modeling of turbulent flows by allowing the Reynolds stress to be modeled as a linear function of the mean velocity gradients. Specifically, the Boussinesq hypothesis assumes that the Reynolds stress is proportional to the product of the mean

velocity gradients and a constant, which is referred to as the turbulent kinematic viscosity $v_t$. In order to calculate this term, it is necessary to employ a turbulence model. The Boussinesq hypothesis is expressed as follows [50]:

$$-\overline{u_i' u_j'} = v_t \left( \frac{\partial \bar{u}_i}{\partial x_j} + \frac{\partial \bar{u}_j}{\partial x_j} \right) - \frac{2}{3} k \delta_{ij} \tag{3.2-4}$$

where $k = \frac{1}{2} \overline{u_i' u_j'}$ is the turbulent kinetic energy [20].

Substituting the Boussinesq hypothesis into **equation 3.2-3** the final formulation of the RANS equations is acquired:

$$\bar{u}_j \frac{\partial \bar{u}_i}{\partial x_j} = \frac{\partial}{\partial x_j} \left[ -\bar{p} \delta_{ij} + v \left( \frac{\partial \bar{u}_i}{\partial x_j} + \frac{\partial \bar{u}_j}{\partial x_i} \right) + v_t \left( \frac{\partial \bar{u}_i}{\partial x_j} + \frac{\partial \bar{u}_j}{\partial x_j} \right) - \frac{2}{3} k \delta_{ij} \right] \tag{3.2-5}$$

## 3.3 Turbulence Models

Turbulence models in RANS simulations are mathematical models that are used to describe the effects of turbulence on the mean flow. There are several types of turbulence models that differ in the level of detail they capture about the turbulent flow. The models that utilize the Boussinesq hypothesis, as stated in **paragraph 3.2**, are called eddy viscosity models. They are based on the concept of turbulent eddies, which are assumed to act like molecular viscosity but with a larger coefficient of viscosity. The choice of turbulence model depends on the level of accuracy required for a given simulation and the computational resources available and consist of three categories, often referred to as "grades". These grades are based on the complexity of the turbulence model and the level of turbulence that it can accurately predict. These are [28]:

1. Zero – equation models: These models assume a fixed eddy viscosity and are the simplest of the turbulence models. They are typically used for low Reynolds number flows, where turbulence effects are relatively small. The calculation of the turbulent kinematic viscosity is achieved by algebraic equations that connect the flow variables.
2. One – equation models: These models solve for the turbulent kinetic energy or its dissipation rate using one Partial Differential Equation (PDE). They are more complex than zero -equation models and are often used for boundary layer and shear flows.
3. Two – equation models: These models solve for both the turbulent kinetic energy and its dissipation rate using two PDEs. They are the most widely used turbulence models and are suitable for a wide range of applications including industrial and environmental flows.

In this diploma thesis, the $k - \varepsilon$ model is used, which is a two – equation model.

## 3.4 The $k - \varepsilon$ Turbulence Model

The $k - \varepsilon$ turbulence model is likely the most common model used in CFD to simulate mean flow characteristics for turbulent flow conditions. It is a two – equation model that gives a general

description of turbulence by means of two transport equations (PDEs) [58]. The first transported variable is the turbulent kinetic energy (TKE) $k$ and the second one is the rate of dissipation of TKE $\varepsilon$. The underlying assumption of this model is that the turbulent viscosity is isotropic, in other words, the ratio between Reynolds stress and mean rate of deformations is the same in all directions [28], [58].

The $k - \varepsilon$ model has been tailored specifically for planar shear layers and recirculating flows. This model is one of the most widely used and validated turbulence model with applications ranging from industrial to environmental flows, which explains its popularity. It is usually useful for free – shear layer flows with relatively small pressure gradients, such as the airflow inside the HVAC duct, as well as in confined flows where the Reynolds shear stresses are most important. It can also be stated as the simplest turbulence model for which only initial and/or boundary conditions needs to be supplied [58].

The TKE $k$ is given by the following PDE:

$$\frac{\partial(ku_j)}{\partial x_j} = \frac{\partial}{\partial x_j}\left[\frac{v_t}{\sigma_k}\frac{\partial k}{\partial x_j}\right] + 2v_t E_{ij}E_{ij} - \varepsilon \qquad (3.4\text{-}1)$$

while the dissipation of TKE $\varepsilon$ can be resolved by the following equation:

$$\frac{\partial(\varepsilon u_j)}{\partial x_j} = \frac{\partial}{\partial x_j}\left[\frac{v_t}{\sigma_\varepsilon}\frac{\partial \varepsilon}{\partial x_j}\right] + C_{1\varepsilon}\frac{\varepsilon}{k}2v_t E_{ij}E_{ij} - C_{2\varepsilon}\frac{\varepsilon^2}{k} \qquad (3.4\text{-}2)$$

where

$u_j$ represents the velocity component in the corresponding direction

$E_{ij}$ represents the component of the rate of deformation

$v_t$ represents the turbulent kinematic viscosity and is equal to:

$$v_t = \rho C_\mu \frac{k^2}{\varepsilon}$$

The constant values used in the standard $k - \varepsilon$ model of this thesis are [6], [58]:

$$C_\mu = 0.09$$

$$C_1 = 1.44$$

$$C_2 = 1.92$$

$$C_{3,RDT} = 0.0$$

$$\sigma_k = 1.0$$

$$\sigma_\varepsilon = 1.3$$

## 3.5 Wall functions

Wall functions are an essential component of many CFD simulations involving turbulent flows, cooperating with the turbulence model used. These functions provide a means of accounting for the effects of turbulent forces near the walls of the simulation domain, without requiring a highly resolved mesh in those regions. By incorporating empirical relationships between the near – wall behaviour of the velocity and turbulent quantities, such as the boundary layer thickness and friction velocity, wall functions can accurately predict the velocity profile in the near-wall region, while still allowing for a coarser mesh in the outer region of the flow. In general, wall functions can compute directly or indirectly the value of the turbulent viscosity at the near-wall cells and store it as a boundary condition in the next iteration of mean values calculation.

As illustrated in **figure 3.5-1**, accurately resolving a boundary layer would require a large number of mesh elements. This would result in an increased number of equations in the final linear system to be solved, leading to a significant increase in the overall computational time. In order to address this issue, wall functions are introduced into the model. By utilizing experimental velocity profiles and some additional assumptions, wall functions can accurately compute the quantities in the first cell center normal to the walls of the object being simulated. Experimental data is used because attempting to model the boundary layer using a discretized scheme or piecewise linear approach would result in a significant error due to the steep gradients near the wall. Therefore, an accurate analytical representation of the boundary layer is required.
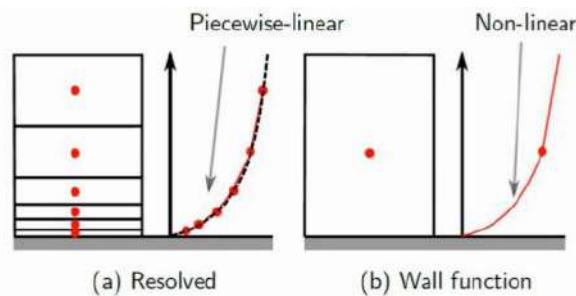


**Figure 3.5-1:** Comparison between fully resolved boundary layer and wall functions approach [57].

In fully turbulent flows, boundary layers have a thickness of a few millimeters. Initially, wall functions were designed to operate for $y^+$ values between 30 and 300. However, modern tools have enabled the use of wall functions that work effectively in the viscous sublayer, log law region, and even buffer region. It is worth noting that in the buffer region, the modelling of one equation of the boundary layer $y^+ = f(u^+)$ is subject to certain assumptions that may affect the accuracy of the results in some cases.
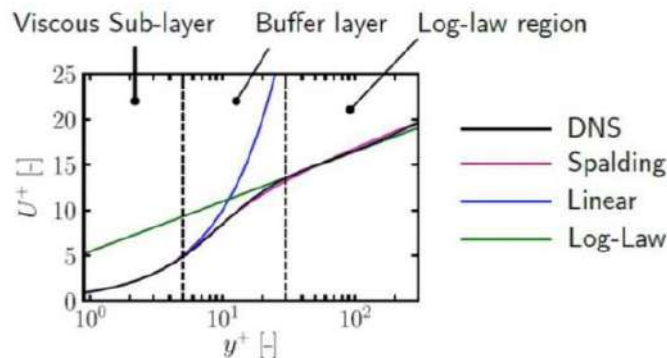


**Figure 3.5-2:** The wall functions approach in all regions of the boundary layer [57].

The parameter $y^+$ denotes the dimensionless distance between the first cell of the boundary layer and the wall and can be interpreted as a local Reynolds number. It is defined as $y^+ = \frac{yu_\tau}{\nu}$

where $u_\tau = \sqrt{\frac{\tau_w}{\rho}}$, defined as the square root of the ratio of wall shear stress and fluid's density, is the shear velocity. Accordingly, $U^+$ is a dimensionless velocity which is defined as $U^+ = \frac{u}{u_\tau}$ and used to normalize the velocity profile in the near-wall region. It is often used in conjunction with $y^+$ to determine the shear velocity at the first cell from the wall through the $U^+$ and $y^+$ relationship, or any other suitable unit depending on the equations and models employed in each specific case and calculation.

The equations that define each portion of **figure 3.5-2** are:

For the viscous sublayer $(1 \leq y^+ \leq 5)$:

$$U^+ = y^+ \Rightarrow \frac{u}{u_\tau} = \frac{yu_\tau}{\nu} \tag{3.5-1}$$

For the logarithmic region $(30 \leq y^+ \leq 300)$:

$$U^+ = \frac{1}{k}\ln(y^+) + C \Rightarrow \frac{u}{u_t} = \frac{1}{k}\ln\left(\frac{yu_t}{\nu}\right) + C \tag{3.5-2}$$

where $C = 5$.

Considering that the buffer zone is neglected, exactly at the intersection of the two previously mentioned regions, both equations are hold. We therefore get that at the logarithmic region:

$$y_c^+ = \frac{1}{k}\ln(y_c^+) + C \tag{3.5-3}$$

The latter equation can be solved using the Newton – Raphson method, thus obtaining the value of $y_c^+$. Following this, the identification of the region in which the point of the computation is performed resides is needed. In order to do that, an initial assumption that the point lies in the viscous sublayer is made. With the use of the velocity field from the previous iteration, the value of $u_t$ is obtained from **equation 3.5-1**, thus computing the value of $y^+$. If the computed $y^+$ value is smaller than $y_c^+$, then the initial assumption is correct. Otherwise, the point lies in the logarithmic region and **equation 3.5-2** should be used for the computation of $u_\tau$ [25].

If the point adjacent to the wall lies within the logarithmic region (which should be the case when using a high – Reynolds turbulence model) where the production and dissipation of the turbulent kinetic energy are approximately equal [25], [52] the turbulence model – specific variables can be computed using the following equations:

$$k = \frac{u_\tau^2}{\sqrt{C_\mu}} \tag{3.5-4}$$

and

$$\varepsilon = \frac{u_\tau^3}{\kappa y} \tag{3.5-5}$$

where $\kappa = 0.41$ is the von – Karman constant.

The previous equations are derived by taking into account that the shear stress at the wall is equal to

$$\tau_w = (\nu + \nu_t)\frac{\partial u_i}{\partial x_j}n_j \tag{3.5-6}$$

# 3.6 Wall Treatment in OpenFOAM®

In the OpenFOAM® environment, wall functions for $k$ and $\varepsilon$ are implemented using equations similar to those described previously, but with slight modifications [20], [31]. The methodology involves computing the velocity gradient at the wall using finite differences to determine the friction velocity $u_\tau$, i.e.

$$\left[\frac{\partial u_i}{\partial x_j}\right]^f n_j = \left[\frac{\partial u_i}{\partial n}\right]^f = \frac{u_i^f - u_i^c}{y} \tag{3.6-1}$$

where $\vec{n}$ is the normal to the wall vector with a direction from the fluid to the wall. $u_i^c$ is the velocity at the center of the cell adjacent to the wall (which is considered to be parallel to the wall) and $u_i^f$ the parallel to the wall velocity at the cell's face (thus $u^f$ is equal to zero). This process employs the velocity values at the center of cells adjacent to the wall and faces of the cells to derive accurate gradients. However, on meshes with high Reynolds numbers, approximating the velocity derivatives in the first cells adjacent to the wall can be challenging. Therefore, to ensure the accuracy of the wall shear stress predictions, an additional equation is employed,

$$\tau_w = u_\tau^2 = (\nu + \nu_t)\left|\frac{\partial u_i}{\partial n}\right| \tag{3.6-2}$$

Initially, a zero Neumann boundary condition is enforced on $k$. Subsequently, $\varepsilon$ undergoes an initial computation of a weighting factor $W$, which depends on the number of the faces belonging

to the cell currently being considered to which the boundary condition will be applied. Following this, the value of $\varepsilon$ at the center of each cell neighboring the wall is equated [31].

$$\varepsilon = \frac{1}{W} \sum_{f=i}^{w} \left( \frac{C_\mu^{\frac{3}{4}} k^{\frac{3}{2}}}{\kappa y_i} \right) \tag{3.6-3}$$

where $k$ is the value of the turbulent kinetic energy at the same cell center and $i$ refers to the number of cells in the wall – normal direction. The value of $y^+$ at the first cell adjacent to the wall depends on the turbulent kinetic energy and is computed from

$$y^+ = C_\mu^{0.25} y \sqrt{\frac{k}{\nu}} \tag{3.6-4}$$

Ultimately, the computation of $\nu_t$ relies on the distance of the cell from the wall. Initially, the dimensionless distance, denoted as $y_c^+$, is computed using a specified equation. If the center of cells adjacent to the wall resides within the viscous sublayer, indicated by $y_c^+ > y^+$, $\nu_t$ is assigned a value of zero.

## 3.7   The SIMPLE Algorithm

In the case of steady flow, there is no need to fully resolve the linear pressure-velocity coupling, as the changes between consecutive solutions are no longer small [7]. In such instances, the SIMPLE algorithm (Semi-Implicit Method for Pressure-Linked Equations) developed by [40] is used. An approximation to the velocity field is obtained by solving the momentum equation. Continuously, the pressure gradient term is computed using the pressure distribution from the previous iteration or an initial guess and after that, the pressure equation is formulated and solved in order to obtain the new pressure distribution. Velocities are corrected and a new set of conservative fluxes is computed. The discretized momentum equation and pressure correction equation are solved implicitly, where the velocity correction is solved explicitly [7].

In greater detail, the SIMPLE Algorithm consists of the following steps:

1. Definition of the boundary conditions.

2. Computation of the velocity and pressure gradients.

3. Iteration on the discretized momentum equation to compute the intermediate velocity field.

4. Computation of the uncorrected mass fluxes at faces.

5. Iteration on the pressure correction equation to produce cell values of the pressure correction.

6. Update of the pressure field: $p^{k+1} = p^k + \omega \cdot p'$, where $\omega$ is the under-relaxation factor for pressure.

7. Update of the boundary pressure corrections $p'_b$.

8. Correction of the face mass fluxes: $\dot{m}_f^{k+1} = \dot{m}_f^* + \dot{m}_f'$.

9. Correction of the cell velocities: $\vec{v}^{k+1} = \vec{v}^* - \frac{Vol\nabla p'}{\vec{a}_P^v}$, where $\nabla p'$ is the gradient of the pressure corrections, $\vec{a}_P^v$ is the vector of central coefficients for the discretized linear system representing the velocity equation and $Vol$ is the cell volume.

10. Update of density due to pressure change.

To facilitate convergence, the fields were initialized by solving the potential flow model using the potentialFoam solver in the OpenFOAM® environment, while the flow problem was resolved using simpleFoam.

## 3.8   Boundary Conditions

The boundary conditions define the interactions between the fluid flow and the solid surfaces, and how the flow conditions alter across the boundaries. The variables that the boundary conditions will be imposed upon for the RANS equation with the $k - \varepsilon$ model are the velocity $(u)$, pressure $(p)$ and the turbulence model's variables $(k, \varepsilon)$.

In the case of a typical HVAC duct, the boundary surfaces appearing in a computational domain are split into three categories: The inlet surfaces of the domain $S_I$, the outlet surfaces $S_O$ and the solid wall boundaries $S_W$. The boundary conditions for $u_i, p, k, \varepsilon$ for the respective boundary patch are the following:

**Inlet:**

At the inlet, velocity is imposed by a constant volumetric flux, or a constant surface normal velocity is defined.

Static pressure is defined by a zero Neumann boundary condition.

The turbulence model's variable $k$ is approximated depending on the turbulence intensity $I$ and the freestream velocity magnitude $u$ at the inlet as follows:

$$k = \frac{3}{2}(uI)^2 \qquad\qquad (3.8\text{-}1)$$

while $\varepsilon$ is approximated depending on the user – defined inlet eddy viscosity ratio $\left.\frac{\nu}{\nu_t}\right|_{inlet}$ :

$$\varepsilon = C_\mu \frac{k^2}{\nu} \cdot \left(\left.\frac{\nu}{\nu_t}\right|_{inlet}\right)^{-1} \tag{3.8-2}$$

**Outlet:**

A zero Neumann condition is imposed to the velocity components on the outlet boundaries, based on the assumption that the flow field is fully – developed when reaching them.

Static pressure is set to a constant imposed value, equal to 0 in terms of manometric pressure for convenience.

A zero Neumann boundary condition is imposed to the turbulence model's variables $k$ and $\varepsilon$.

**Walls:**

The solid walls are treated using wall functions.

The boundary conditions used for each boundary patch are summarized below:

| Variable | Symbol | Type | Value |
|---|---|---|---|
| Volumetric Flow Rate | $\dot{V}$ | Flow rate Inlet Velocity | $V_0 \ m^3/h$ |
| Pressure | $p$ | Zero gradient | - |
| Turbulent Kinetic Energy | $k$ | Fixed value | $0.015 \ J/kg$ |
| Dissipation of Turbulent Kinetic Energy | $\varepsilon$ | Fixed value | $0.134073 \ m^2/s^3$ |

**Table 3.8-1:** Boundary conditions for the inlet patch for the steady-state HVAC case.

| Variable | Symbol | Type |
|---|---|---|
| Velocity | $U$ | Zero gradient |
| Pressure | $p$ | Fixed value $(p = 0)$ |
| Turbulent Kinetic Energy | $k$ | Zero gradient |
| Dissipation of Turbulent Kinetic Energy | $\varepsilon$ | Zero gradient |

**Table 3.8-2:** Boundary conditions for the outlet patch for the steady-state HVAC case.

| Variable | Symbol | Type |
|---|---|---|
| Velocity | $U$ | Wall function |
| Pressure | $p$ | Zero Gradient |
| Turbulent Kinetic Energy | $k$ | Wall function |
| Dissipation of Turbulent Kinetic Energy | $\varepsilon$ | Wall function |

**Table 3.8-3:** Boundary conditions for the wall patch for the steady-state HVAC case.

## 3.9 Discretization Schemes

Term "discretization schemes" refers to the mathematical methods used to transform the continuous governing equations of fluid flow into discrete algebraic equations. The accuracy of the discretization scheme used is an essential factor that determines the level of precision of the numerical solution, as well as its convergence. The discretization schemes used in this thesis are hybrid for the gradient, adapting their order based on local flow conditions (cellLimited or faceLimited Gauss Linear). They use second-order formulation in regions with smooth gradients but revert to first-order near sharp gradients to maintain stability and prevent oscillations. This makes them hybrid schemes, effectively blending second-order accuracy with first-order stability. Second order schemes were used both for the divergence (bounded Gauss linearUpwind) and for the Laplacian terms (Gauss linear limited).

Generally, higher order schemes enhance the accuracy of the simulation, as they can approximate the solution to a higher degree of precision. This results in a reduction of truncation errors, which are the errors caused by the approximation of continuous equations with discrete equations. Second-order schemes can handle steeper gradients in the solution, which is important for simulating complex phenomena accurately. The improved accuracy provided by second-order schemes can lead to faster convergence of the numerical solution, as well as more accurate results overall. The residuals plot for a typical simulation can be seen in **figure 3.9-1**. The latter proves that a typical HVAC duct simulation can be faced as a steady-state problem, as the flow inside the geometry is stabilized.
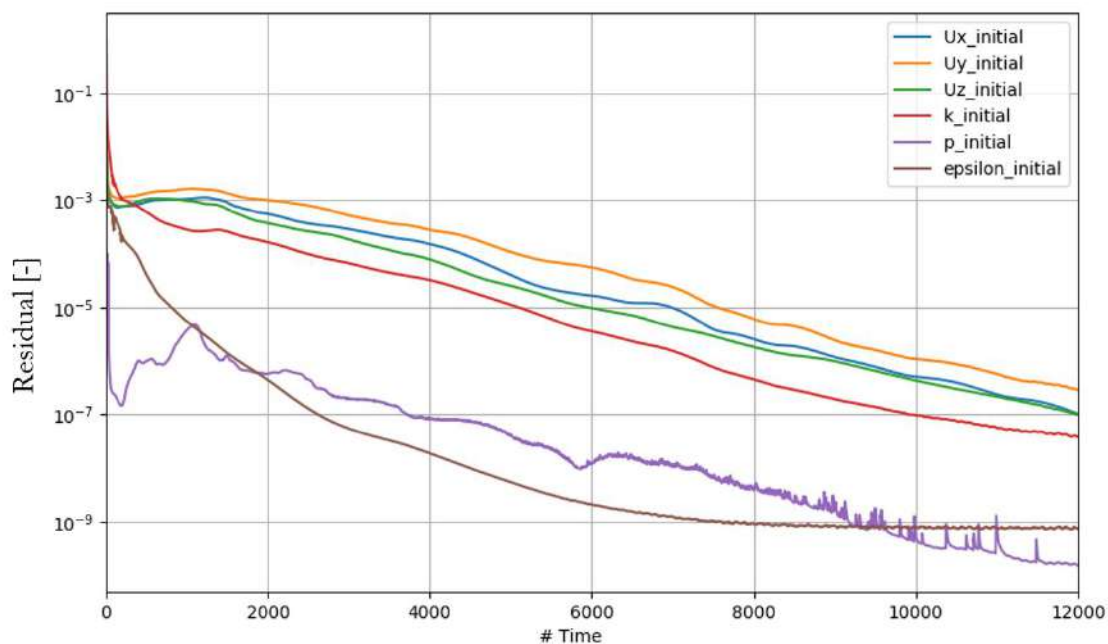


**Figure 3.9-1:** Typical convergence plot for 2nd order schemes for the benchmark HVAC duct steady-state Proudman CFD model.

# 3.10 Mesh Generation

As a first step for the implementation of the simulation, a computational domain is created, as seen in **figure 3.10-1**. It is important to note that the HVAC duct is isolated from the vehicle's instrument panel and is analyzed independently. A bulbous structure serves as an artificial inlet patch, designed specifically for computational purposes, connecting to an intermediary funnel that directs airflow into the main duct configuration within the passenger vehicle. Downstream of this duct, a bell-shaped plenum is positioned as the outlet boundary through which the airflow is discharged. It is noted that the jet exiting the blower assembly is located at the center of the plenum. Furthermore, two refinement zones are designated in the wake of the blower, where the mesh is significantly denser. However, the second zone features reduced mesh refinement in comparison to the first one, as the sound intensity diminishes, thereby reducing computational cost.
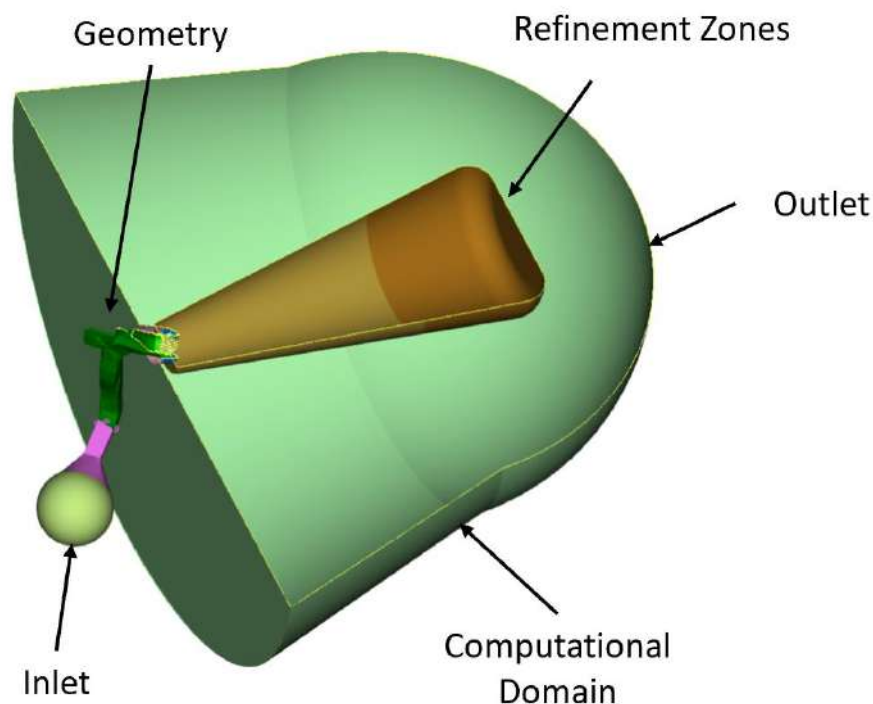


**Figure 3.10-1:** The computational domain. Presentation of the artificial inlet bulbous structure (yellow), the inlet extrusion (pink), the discharge plenum (light green) serving as the outlet boundary patch and the HVAC side-duct of car 1 (dark green) as explained in **paragraph 1.2**. Refinement zones 1 (light orange) and 2 (dark orange) are also introduced, with dense and coarse refinement respectively.

The computational mesh was generated following a surface-to-volume approach, with the use of a commercial meshing software provided by TME. It consists of regions of locally uniform hexahedral cells. The meshing procedure begins with the generation of a uniform mesh made up of cubes of edge length $h_0$, which are then refined in specified regions, up to a predefined refinement level. Each refinement level $n$ is attained by performing $n$ consecutive subdivisions of the initial cubic cells of edge height $h_0$ into 4 equal cubic cells. Therefore, the edge length of a cubic cell of refinement level $k$ is equal to $h_k = \frac{h_0}{2^k}$ [36]. Finally, in the near wall regions, inflation layers are introduced.

A mesh sensitivity analysis was conducted to determine the appropriate base cell size. Typically, a finer mesh enhances the accuracy of capturing the flow field surrounding a geometry, albeit at the expense of increased computational time. The objective was to find a balance between achieving accurate results and minimizing computational costs, thereby optimizing the efficiency of the simulation model. Ultimately, a base cell size of $h = 2.5\ mm$ was selected, resulting in a reduction in the number of elements from approximately 31 million in the corporate benchmark mesh to just under 20 million, representing a reduction in computational cost of about $35\%$.
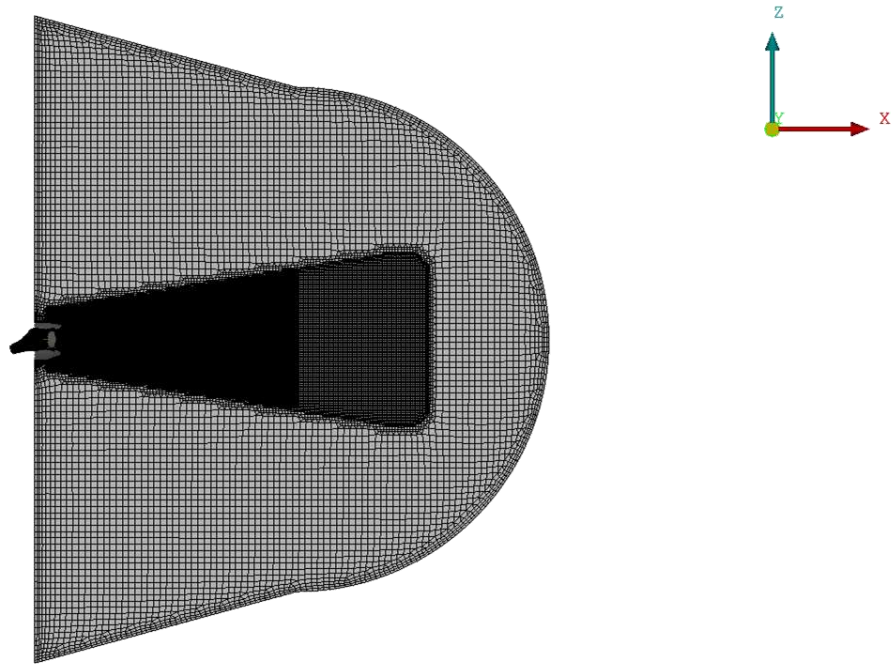


**Figure 3.10-2:** Computational mesh with base cell value $h = 2\ mm$ at $y = 0$.

The mesh around the most delicate parts of the simulated assembly such as the blades of the register channelling the airflow towards the passenger as depicted in **figure 1.2-2**, is composed of hexahedral cells with minimum height of $0.4\ mm$ (e.g. the register's blades) in order to ensure the integrity of the geometry. Moreover, there are two refinement zones in the wake of the blower, where the mesh is gradually getting coarser, as the sound intensity diminishes by the square of the distance. The first zone, closer to the geometry, consists of cells with a height of $3.1\ mm$, while the second one has an average cell height of $6.2\ mm$. At the outlet, the density of the mesh was significantly reduced to save computational resources, as there should not be any flow field phenomena of significant interest or importance in that region, resulting in a cell of average height of $24.4\ mm$.

As anticipated, a denser mesh is unnecessary outside these refinement regions because no airflow is expected to pass through them, owing to the design of the register's housing outlet. By decreasing the number of cells outside the area of interest, significant reduction of the required computational resources is accomplished.
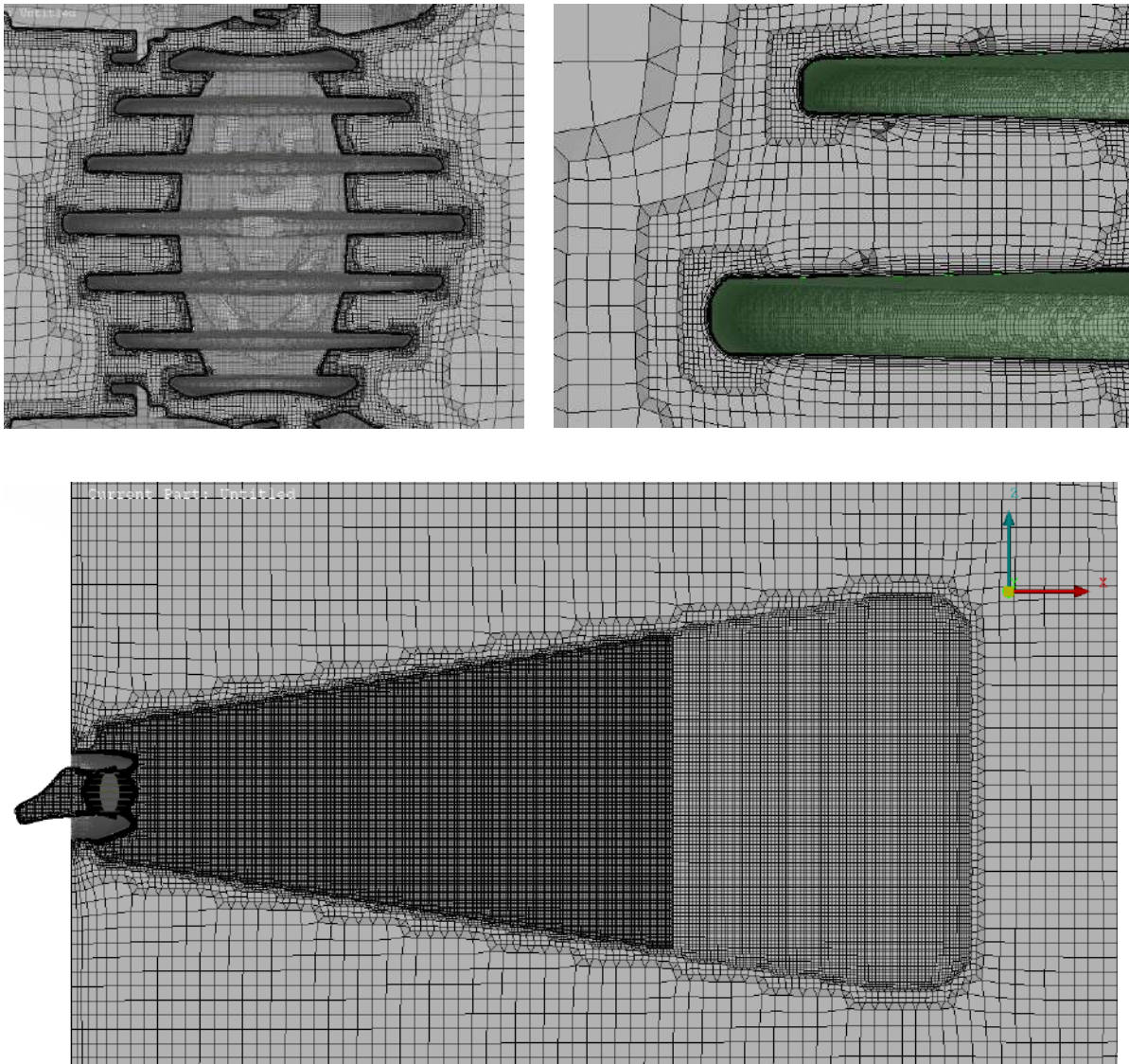
**Figure 3.10-3:** Various levels of refinement across the computational domain at $y = 0$. Close up view on the register (up left) and the register's blades (up right). Duct's outlet and register assembly (bottom).
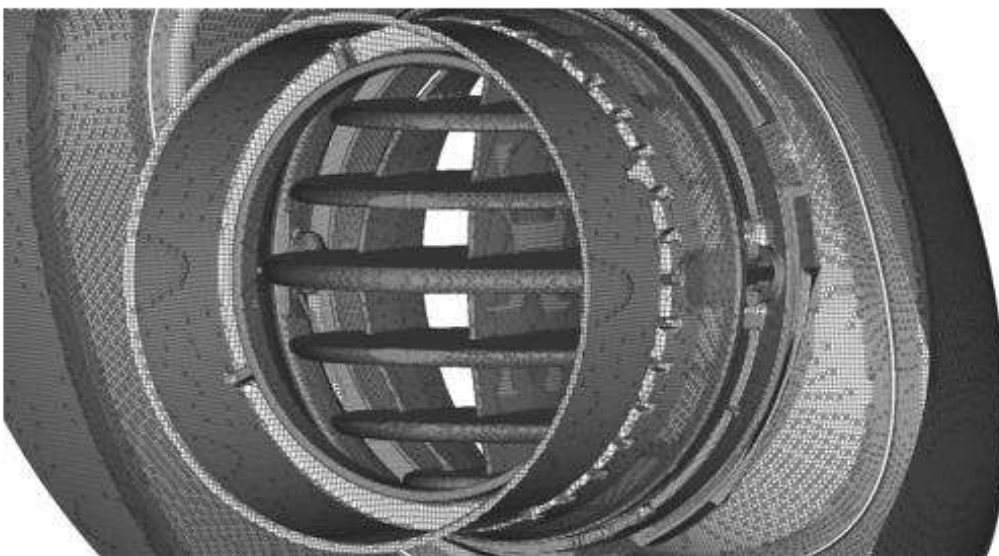


**Figure 3.10-4:** Surface mesh around the register and its housing of side-duct of car 1.

# Chapter 4:

# Calibration of Steady-State Model with Previous Experimental Measurements

Developing a suitable and effective approach to compare the outcomes of the steady-state CFD model with both the compressible simulation and experimental results from the work of [36], carried out as part of a diploma thesis in the PCOpt of NTUA, was a key consideration. The main disadvantage of the compressible model of [36] lies within its failure to accurately predict the noise in the high frequency region, as illustrated in **figure 4-1**.
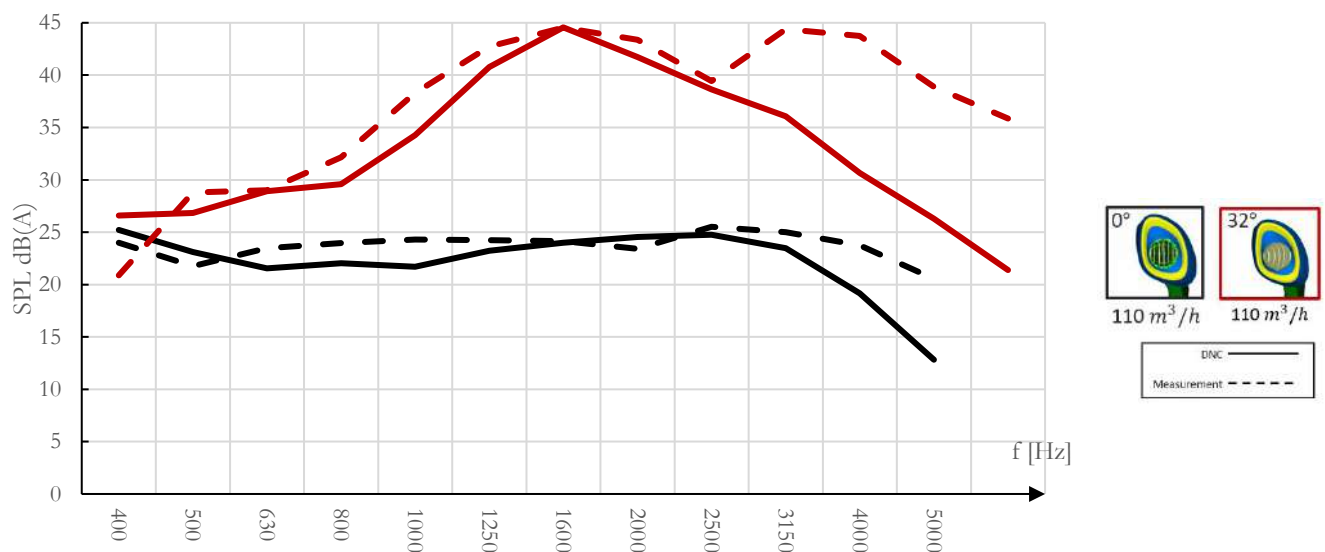


**Figure 4-1:** Prediction of aerodynamically induced noise for two configurations of the side-duct of car 1 [36]. Comparison between the compressible DNC model (compact line) versus experimental measurement (dashed line). Significant drop of accuracy in the high frequency region. Wall clock time of simulation ≈ 4 days on 512 CPUs.

The main goal of the steady-state model, which from now on will be referred to as the "proposed CFD model," in terms of accuracy, was to provide a more satisfactory correlation with the experiment than that of the DNC of [36]. Furthermore, this comparison aimed to facilitate the accuracy of the proposed model, with the feedback obtained being utilized to inform subsequent stages of the research process.

## 4.1 Noise Index Estimation in Experiment and DNC

The term "Noise Index Estimation" (NIE) pertains to the standardized methodology for assessing sound intensity using relevant metrics. A standardized procedure was developed by [36] specifically for isolated HVAC duct configurations, as detailed in **section 1.3**. This approach involved the capture of noise through pressure perturbations using experimental probes, commonly referred to as probes. Subsequently, these perturbations were transformed into Sound Pressure Level (SPL) values.

The SPL, i.e. the pressure fluctuations observed at any point in space, is a logarithmic scale measured in decibels and is a valuable tool for comparison of various sound measurements [11], [21], [48]. This is given by:

$$SPL(dB) = 10 \log_{10}\left(\frac{p_{rms}}{p_{ref}}\right)$$

(4.1-1)

It is defined using the acoustic root-mean-squared (RMS) pressure (**equation 4.1-2**) and a reference pressure, the latter being equal to $2 \cdot 10^{-5} \, Pa$ for measurements in air [11], [21]. The RMS pressure is defined as the square root of the mean squared pressure at each point [21]:

$$p_{rms} = \sqrt{\bar{p}^2}$$

(4.1-2)

$$\bar{p}^2 = \lim_{T\to\infty}\left[\frac{1}{T}\int_{t_0}^{t_0+T} p'^2(t)dt\right]$$

(4.1-3)

For the computation of term $p'^2(t)$ an unsteady, compressible CFD model is required.

As the DNC model and the experiment of [36] follow a similar philosophy, wherein noise generation and propagation are directly computed through perturbations in the pressure and density fields using a compressible fluid approach, the same NIE criterion as described in **section 1-3** is applicable in both of them. Consequently, a brief overview of the noise capturing technique employed in the unsteady, compressible DNC model will now be outlined.

The pressure field resulting from compressible DNC simulations contains both convective pressure fluctuations, expressing convected flow structures and acoustic pressure fluctuations, expressing sound waves [17], [54]. In other words, pressure fluctuations in the field can be expressed as a superposition of two components:

$$p' = p_c' + p_a'$$

(4.1-4)

where $p_c'$ is the convective component and $p_a'$ the acoustic one.

The $p_c'$ component arises from pressure gradients associated with eddies carried by the flow and is commonly termed pseudo-sound. This designation stems from its absence of certain defining attributes of sound, such as non-adherence to the wave equation. In order to compare numerical results with experimental data, it is preferable to concentrate solely on genuine sound. Therefore, in the context of DNC, the acoustic perturbations must be isolated from the raw computed pressure field.

The DNC model of [36] computes pressure fluctuations, which are then recorded and stored using 8 linear probe arrays of a length denoted as $L$, consisting of 512 sampling points each (see **figure 4.1-1**). These arrays are strategically positioned near the jet exit of the blower. Subsequent to storage, the wavenumber filtering method is applied to isolate the acoustic component of these fluctuations. The positioning of the array centers is arranged to align with the respective locations of the microphones utilized in the experimental setup. The acoustic pressure recorded at these designated probes accurately reflects the corresponding measurements obtained in real-life scenarios.
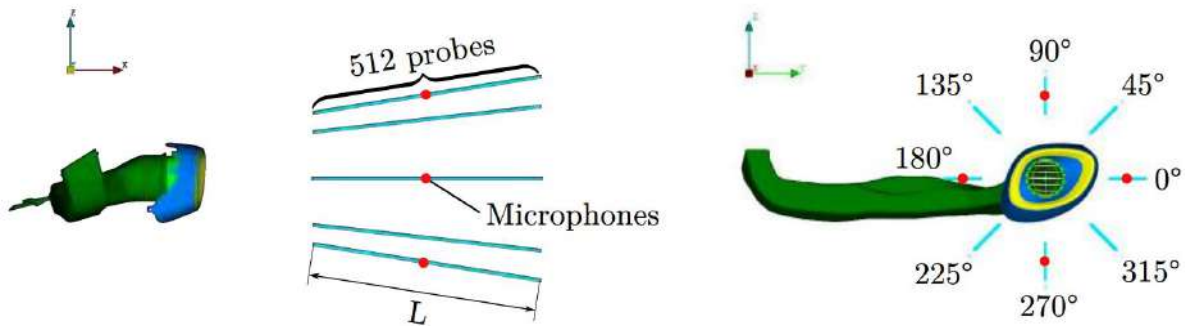


**Figure 4.1-1:** Positioning of 8 linear probe arrays of length $L$ consisting of 512 sampling points for pressure fluctuation propagation capturing downstream of the side-duct of car 1, as proposed by [36]. The center of the 4 cardinal ones coincides with the microphone positions of the measurements.

Having acquired the desired acoustic pressure over time, the corresponding SPL graph in the frequency spectrum can be extracted, consisting of constituent frequencies and their respective amplitudes, resulting in a direct comparison of the simulation results with the original experimental measurements.

## 4.2   Noise Index Estimation in a Steady-State model

Given that the proposed model lacks temporal resolution and, consequently, does not provide information on the frequency spectrum, direct comparison between Proudman's findings, experimental data, and DNC results of [36] is not possible. Hence, an alternative criterion that disregards transient effects must be chosen for comparison purposes.

The total SPL or OASPL (Overall SPL) is a metric that represents the total sound emission in the DNC and experimental applications. It is defined as the integral of the RMS pressure divided by a reference pressure, over the frequency spectrum [38]:

$$OASPL = 10 \log_{10} \left( \sum_{i=1}^{m} \frac{|\hat{p}|}{p_{ref}} \right) \tag{4.2-1}$$

Where $\hat{p}$ is the SPL value per frequency and $m$ is the number of discrete frequencies, defined by the respective temporal discretization.

As Proudman's acoustic analogy does not directly compute acoustic pressure, an alternative approach was adopted to capture comparable information, indicative of the overall acoustic emission within a specified domain. This involved integrating the acoustic power $(P_{ac})$ per unit volume across the entire computational domain. Dividing this integrated term by a reference power value yields a dimensionless quantity, which can be expressed in units of dBA:

$$OAPSD = 10 \log_{10} \left( \sum_{i=1}^{n} \frac{P_{ac}}{P_{ref}} \right) \tag{4.2-2}$$

where $n$ is the number of cells of the computational mesh and $P_{ref} = 10^{-12} \frac{W}{m^3}$ is the reference power. Term $P_{ac}$ refers to the acoustic power computed by Proudman's acoustic analogy, utilizing the formula described in **section 5.1** for the volumetric and the surface term respecrively and is derived from a steady-state solution.

## 4.3 Steady-State Model Calibration with DNC and Existing Measurements

A series of simulations was conducted in the context of this diploma thesis using various volumetric flow rates, including one case with a tilted register[2], as showcased in **figure 4.3-1**, to simulate geometric variation effects, which would represent a modification of the duct's design during the development period. The results obtained from the proposed CFD model were then compared with experimental measurements [36]. It is important to note that the specific positioning of the measurement locations significantly influences the observed phenomenon's intensity. Therefore, it is emphasized that for the particular experiment, the microphone or probe was positioned 500 mm downstream of the blower's outlet, measured from a vertical plane aligned with the outer edge of the register. The outcomes of this comparison are depicted in **figure 4.3-2**.
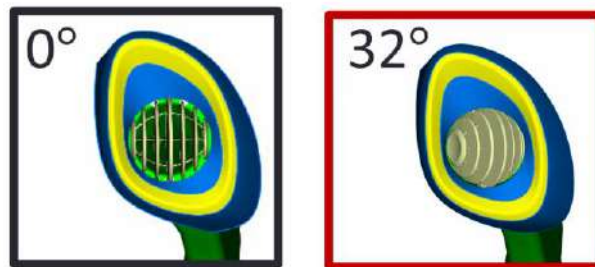


**Figure 4.3-1:** Rotation of the register of side-duct of car 1. Nominal positioning (left) versus $32°$ tilted configuration (right).

---

[2] The HVAC duct design enables the passenger to adjust the orientation of the register blades, directing the airflow towards a preferred target, such as the face or upper body, or away from it as desired.
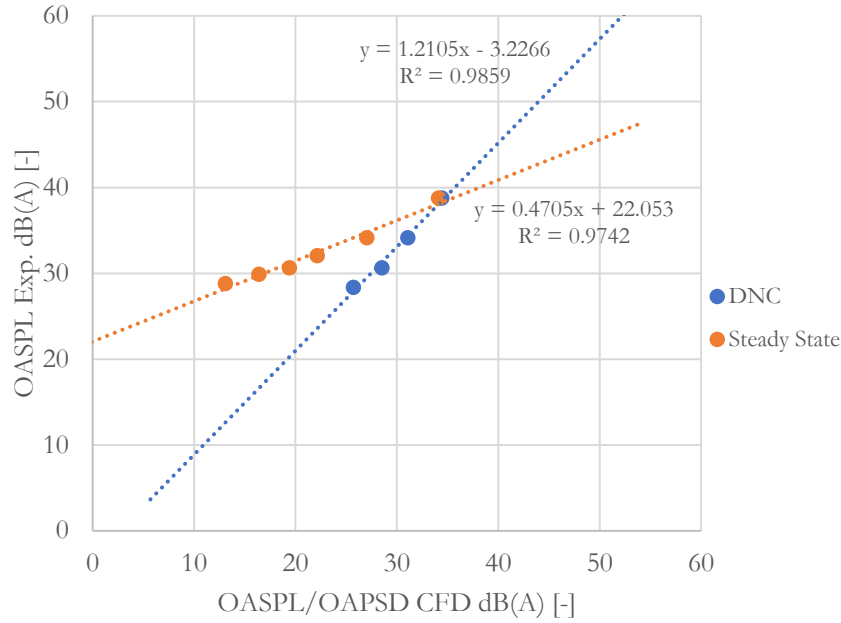
**Figure 4.3-2:** Calibration of the CFD models of [36] (blue) and the proposed one (orange) with the experiment of [36] for probe location of 500 mm.

In the graph of **figure 4.3-2**, the horizontal axis denotes the OASPL or OAPSD value derived from each CFD model, whereas the vertical axis represents the corresponding OASPL value obtained from the experimental measurement [36]. This representation method allows for the examination of the correlation between each CFD model and the value measured in the laboratory, considering the latter's representativeness of reality. Both quantities are dimensionless, have a logarithmic scaling and exhibit a linear relationship with the experiment.

Following a linear interpolation process for each dataset, two-line equations are generated, each accompanied by a linear correlation factor $R^2$. This factor is of extreme importance, as it signifies whether the CFD quantities exhibit an expected pattern, allowing for their prediction based on the assumption that they disperse around this line equation. Both correlation factors exceed 97%, indicating a robust linear correlation between the quantities represented on the horizontal and vertical axes. This finding holds significant importance, as it enables the establishment of a direct link between the output of a CFD case regarding the OASPL or OAPSD value and the anticipated actual value, through a straightforward projection on the linear interpolation equation.

Moreover, the interpolation line can be transformed using an algebraic method to convert it into the bisector of the first and third quadrants. This adjustment ensures that the CFD result closely aligns with the experimental value, thereby facilitating the comparison of the two Key Performance Indicators (KPIs). This transformation enables the evaluation of both the relative as well as the absolute deltas among two or more ducts and understand how much quieter or noisier each one is in real life.

To transform the line one has to multiply every point's abscissa by its slope and add the constant term. In general, if $y = ax + b$ is the linear equation, then $x_i' = ax_i + b$, where $i$ is the specific point of the line, $a$ is the slope of the line equation and $b$ is the constant term, should be the corrected abscissa of each point. As a result, the diagram of **figure 4.3-3** is created:
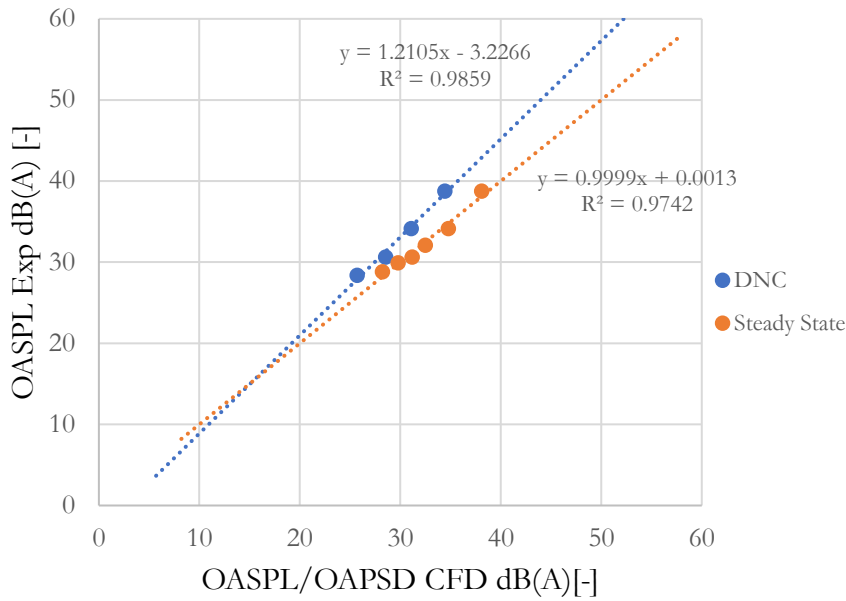
**Figure 4.3-3:** Algebraic transformation of the steady-state CFD line. The DNC line remains unchanged for the purpose of direct comparison.

The impact of the calibration on the model's line is particularly apparent in the chart of **figure 4.3-4,** which directly juxtaposes the OASPL values obtained from the raw integration and the corrected acoustic power results with those from the experiment across three selected cases: Case 1 refers to the original register configuration as depicted in **figure 4.3-1** for a volumetric flow rate of $\dot{V} = 110 \frac{m^3}{h}$, case 2 represents the tilted register variation for the same flow rate and finally case 3 is the original configuration for $\dot{V} = 140 \frac{m^3}{h}$. Additionally, the DNC results of [36] are included in the same chart as a benchmark. It is evident that when the correction is applied, the disparity between the CFD simulations and the experimental data is notably diminished, underscoring the necessity of employing the aforementioned calibration technique.
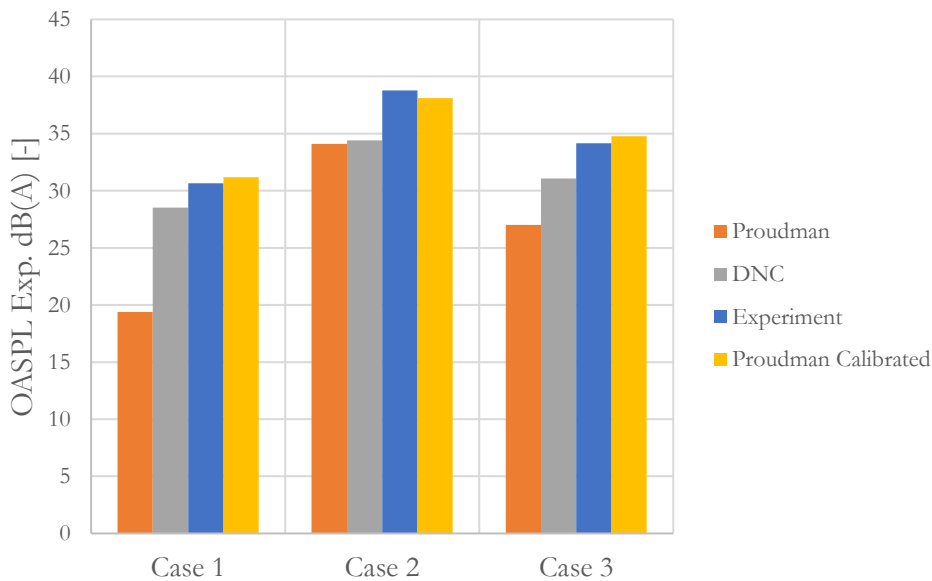


**Figure 4.3-4:** Absolute OASPL values for each CFD model and the experiment of [36] for three different configurations. Calibration of steady-state model after the projection to the linear interpolation equation.

After this calibration, the relative error between the experiment and the newly developed steady-state model was limited within the range of 0.52-2.24%, achieving excellent accuracy.

Upon careful consideration, it was decided to utilize the data set corresponding to microphone placement 1 meter downstream of the blower as a best-practice approach. This decision was based on its alignment with the typical observation distance within a vehicle's cabin. However, due to the predominant use of a 500 mm probe location in the DNC simulations of [36], achieving consistency between the two CFD models was not feasible. Consequently, for comparative purposes between the CFD models, the prior correlation should be retained. However, when projecting the results to the experimental data, the correlation showcased in **figure 4.3-5** was applied:
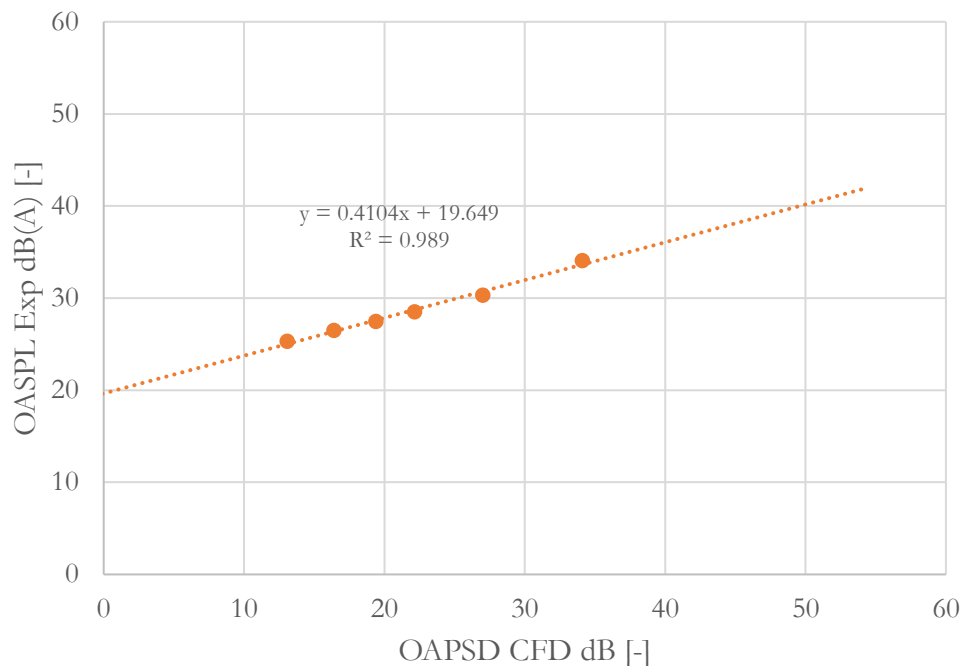


**Figure 4.3-5:** Calibration of the new CFD model with the experiment of [36] for probe location of 1000 $mm$.

Consequently, the calibration coefficient and the constant parameter for aligning the findings of the steady-state model with the corresponding experimental data for a probe location of 1000 mm are as follows:

$$G_V = 0.4104 \text{ and } b_V = 19.649$$

The further $G_V$ deviates from the bisector value ($G_V = 1$), the more challenging it becomes for the engineer to assess the duct's performance relative to the anticipated real value prior to transformation. Hence, the essence of the transformation is increased. Additionally, while the current methodology may be effective for the specific HVAC duct, its applicability to other geometries remains to be evaluated. Last but not least, a notable limitation of this approach is the inability to determine whether the model underestimates or overestimates the computed results within a region of uncertainty.

# Chapter 5:

# Design of a Noise Reduction Countermeasure

## 5.1   Visualization of Noise Sources

After assessing the accuracy of the simulation model, the potential of visual information from post-processing fields in guiding the aeroacoustic development or even the optimization of an HVAC duct was explored separately. Specifically, the objective was to determine whether modifying features of the geometry that appear to generate high acoustic power could positively impact the overall acoustic performance. To achieve this goal, the following two KPIs that aim to visualize noise sources were primarily utilized:

The first KPI involves the volumetric component of Proudman's acoustic power, which calculates the acoustic power resulting from the volume of isotropic turbulence using the theory outlined in **paragraph 2.5**. It computes the acoustic power per unit volume in each cell of the mesh, denoted as $P_V$ $\left[\frac{W}{m^3}\right]$, in terms of TKE $k$ and its dissipation $\varepsilon$ according to **equation 5.1-1**:

$$P_V = \alpha_\varepsilon \rho \varepsilon M_t^5 \tag{5.1-1}$$

In this formula, $\rho$ is the fluid's density, $M_t = \frac{\sqrt{2k}}{c}$ is the relative Mach number, where $c$ is the speed of sound and finally $\alpha_\varepsilon = 0.1$ is a model constant.

The previous quantity is also output in a dimensionless, logarithmic scale using:

$$L_{P_V} = 10 \log_{10}\left(\frac{P_V}{P_{ref}}\right) \tag{5.1-2}$$

where $P_{ref} = 1e^{-12} \left[\frac{W}{m^3}\right]$ is a reference power value per unit of volume.

The value of $L_{P_V}$ in every cell is stored, resulting in the Proudman Field, as depicted in **figure 5.2-3**.

The second KPI is referred to as the surface term of Proudman's acoustic analogy and was developed in the context of this diploma thesis using the Paraview open-source post-processing and flow visualization software [41]. This development was deemed necessary because, in low Mach number flows, dipole noise sources originating from the surfaces of solid boundaries tend

to dominate over quadrupole (volumetric) sources. The representation of the surface term per unit area, computed at each cell of the mesh, is determined by **equation 2.5-3b**. Afterwards, the surface term is converted into a dimensionless quantity with a logarithmic scale using:

$$L_{P_S} = 10 \log_{10} \frac{P_S}{P_{ref}}$$

(5.1-2)

In a similar fashion, the value of $L_{P_S}$ in every cell of the geometry's surface mesh is stored, resulting in the Proudman surface representation, as depicted in **figure 5.2-1**.

Both KPIs provide valuable insights into the mechanisms of noise generation. To ensure the safe and accurate modification of design features, it is imperative to consult both indicators. Red areas highlight regions of high acoustic power, effectively pinpointing the features that contribute the most to noise generation inside the duct and ultimately to the passengers' ears.

## 5.2   Design Modification of HVAC Duct

By observing the post-processing figures of the duct, it was noted that a specific edge, perpendicular to the register's housing, had the most detrimental effect on the overall performance of the duct. This observation is evident in the plot depicting the logarithmic magnitude of the acoustic power field over the duct's surface.
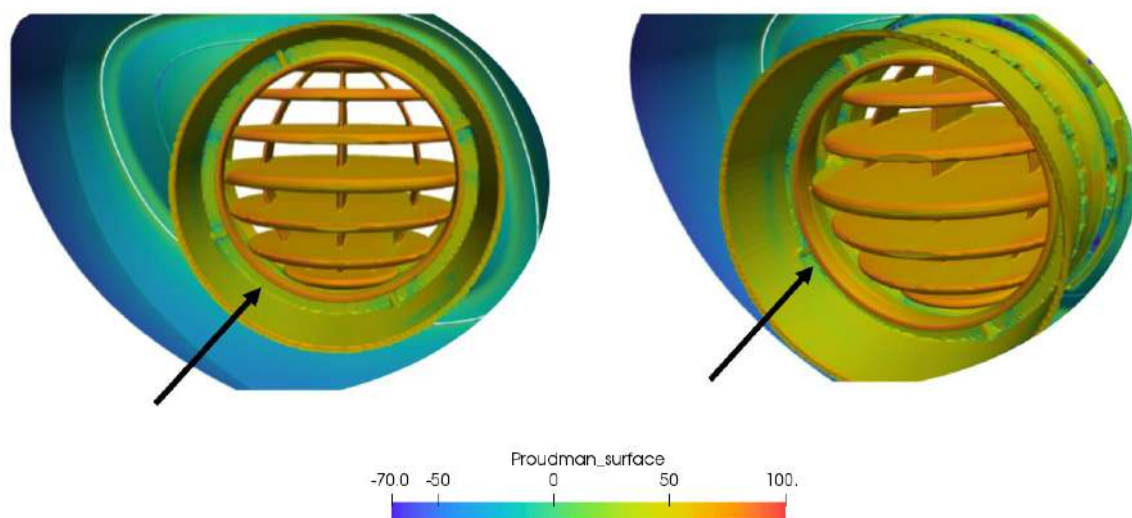


**Figure 5.2-1:** Proudman's acoustic power representation at the register's surface. Perpendicular edge on the register's housing and its effect on noise generation.

From now on this perpendicular edge will be referred to as "ring" due to its circular symmetry.

After consulting the mechanical design department it was found out that this feature was manufactured to support some porous material, which was placed there to absorb sound

emisssions. Hence, it was decided to remove this feature, to measure its impact. This led to the design specification showcased in **figure 5.2-2**:



**Figure 5.2-2:** Original register's housing (left) versus no ring design modification (right).

In order to understand in depth the effect of the countermeasure, the flow field for various quantities is hereby presented side to side for the original and modified registers.

Initially, the Proudman field, as depicted in **figure 5.2-3**, illustrates a notable rise in acoustic power around the ring feature. This occurrence arises due to the edge serving as a stagnation point for the flow, where the fluid interfaces with the solid boundary, leading to noise generation. Furthermore, the interaction between this feature and the blades appears to exert a significant influence on the intensity of the phenomenon.
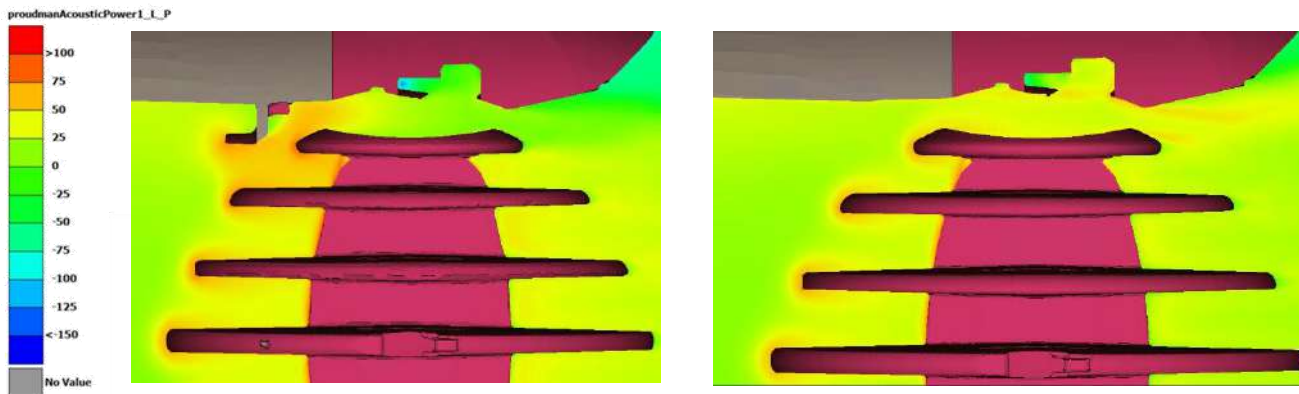


**Figure 5.2-3:** Proudman Field at the symmetry plane. Effect of ring removal on acoustic power.

The aforementioned observations can be substantiated by examining the k field of the turbulence model, as showcased in **figure 5.2-4**, which characterizes the turbulence intensity within the flow. The initial design configuration results in the formation of a recirculation bubble in the wake of the ring, impacting the performance of the outer blades and consequently amplifying the acoustic emission. Following the design alteration, noticeable reductions in the vortical structures near the ring and upper blade region are apparent, indicating an improvement in the airflow patterns and a corresponding reduction in acoustic disturbances.
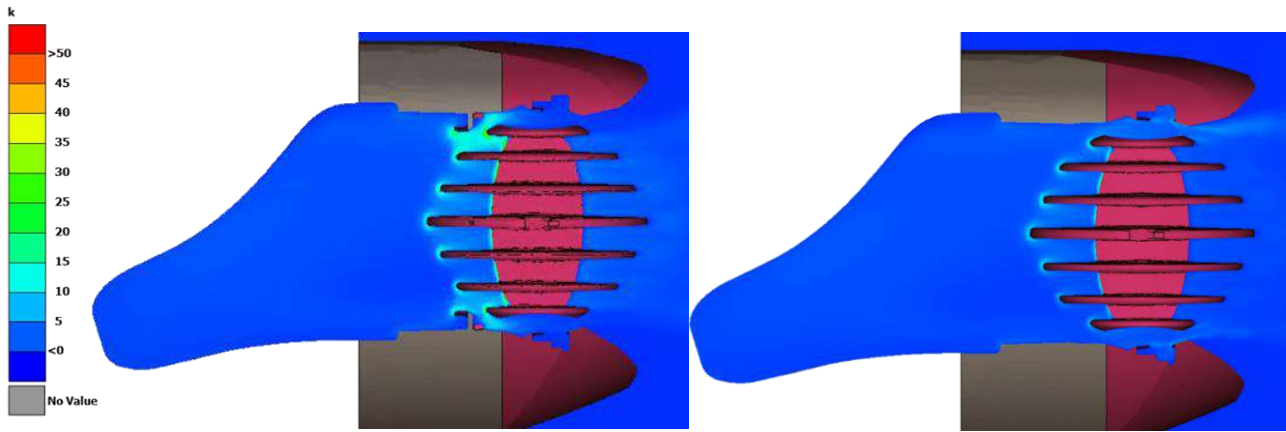
**Figure 5.2-4:** $k$ field at the symmetry plane. Significant decrease of vortical structures at the ring – blade region.

Eliminating this feature resulted in an enlargement of the cross-sectional area at the inlet of the register, leading to a localized decrease in velocity magnitude (**figure 5.2-5**) due to the principles outlined in the continuity equation. As the acoustic power is directly proportional to the Mach number, the overall acoustic emission experienced a notable reduction as a consequence, which can be observed in **figure 5.2-6**.
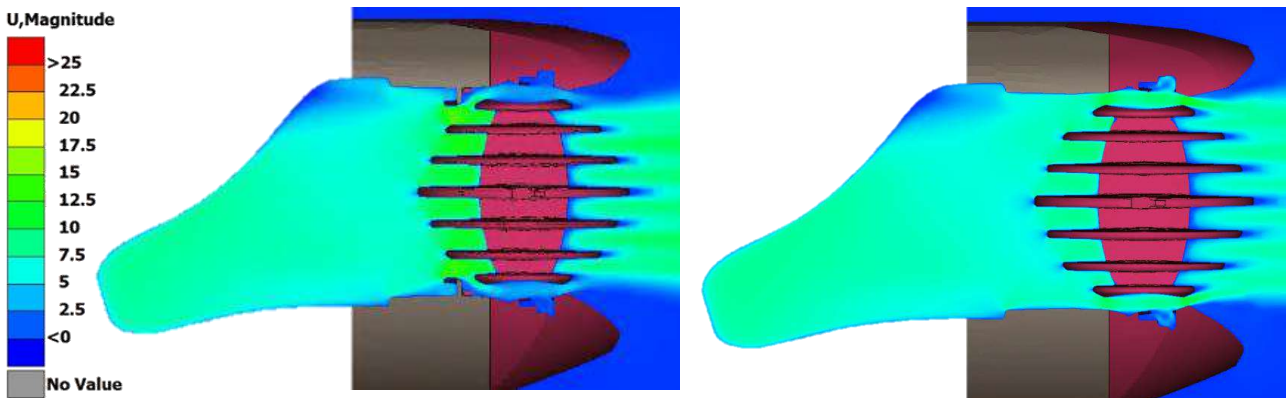


**Figure 5.2-5:** Velocity field at the symmetry plane. Evident decrease of the magnitude of velocity at the register's inlet.
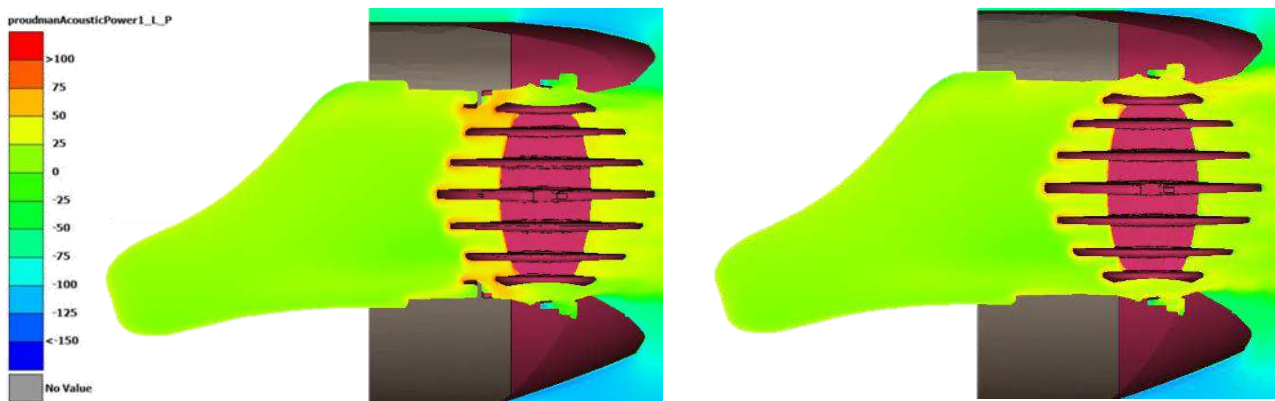


**Figure 5.2-6:** Proudman Field at the symmetry plane. Overall decrease of the acoustic power at the inlet of the blade area

## 5.3 Evaluation of Design Modification Based on Previous Experiment

Following the qualitative assessment of the ring's removal, it is useful to quantify its impact. Utilizing the metrics outlined in **section 4.3** and referencing the calibration factor established through the analysis of the experimental measurements of [36], the OAPSD values for both design configurations were computed and are presented in **figure 5.3-1**.

The steady-state model predicted a reduction of 4.1 dBA in sound emission for the design countermeasure compared to the nominal configuration, corresponding to a relative improvement of 14.73%. This reduction in total sound emission is contrasted with the difference observed between the original configuration and the scenario of the tilted register as outlined in **section 4.3**. The latter represents a real-world case demonstrating a notable increase in sound perceived by passengers.
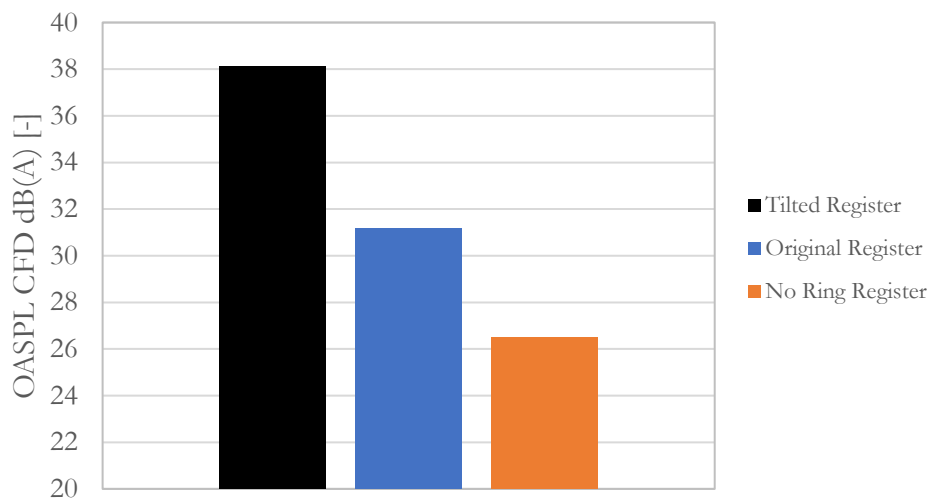


**Figure 5.3-1:** Ring's effect compared to the nominal configuration and 32-degree tilted register as described in **section 4.3**.

Subsequently, the necessity for validating the design countermeasure with experimental measurements became evident.

# Chapter 6:

# Experimental Measurements

To ascertain the correlation between the proposed model and real-world conditions for other HVAC ducts, a sequence of experimental measurements was conducted in the context of this diploma thesis. The primary objective of the experiment was twofold: to assess the accuracy of the simulation and explore its potential for future development. Additionally, ensuring the repeatability of the experiment compared to the measurements of [36] was crucial for directly comparing the results to the original correlation.

## 6.1   Experimental Setup

Based on the insights gained from the experiment of [36], a standardized configuration was established for measuring HVAC ducts outside of the vehicle cabin, as depicted in **figure 6.1-1**. An airflow generator is employed to supply airflow to a pipeline assembly connected to the test piece. Given the objective of solely measuring the aerodynamic noise originating from the HVAC duct, stringent measures are taken to minimize interference from other sources of background noise. The primary sources of background noise, notably aerodynamic fan noise and mechanical noise resulting from vibrations, emanate from the equipment used for generating airflow.
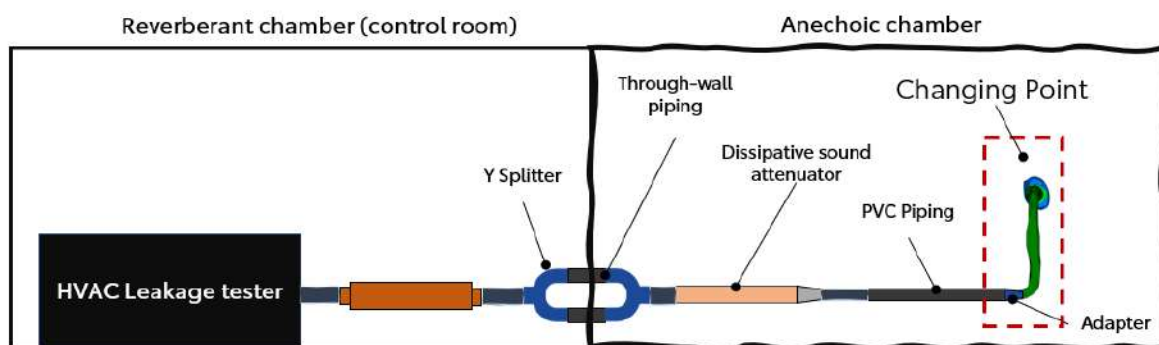


**Figure 6.1-1:** Experimental setup for measurement of aerodynamically induced noise in isolated HVAC ducts.

To mitigate the potential transmission paths of background noise to the receiver locations, precautions are taken to isolate the test setup from extraneous noise sources. The test piece is situated in an anechoic chamber or separate rooms housing the airflow generator, thereby

minimizing the influence of background noise from both inside and outside the ducting. Flexible piping is utilized for channeling airflow between the airflow generator and the test piece, mitigating the transmission of noise through rigid connections. Additionally, two sound attenuators are inserted into the airflow path to attenuate sound propagation within the conducted airflow. Ensuring a fully developed turbulent profile at the blower inlet is crucial, achieved by positioning a 4-meter-long, rigid, circular, straight tube immediately preceding the blower. A cone is placed before the tube to induce turbulence tripping. Lastly, a customized adapter, fabricated using 3D rapid prototyping, facilitates the connection between the blower and the rigid tube.

## 6.2  Test Piece Geometries

A diverse range of HVAC ducts were subjected to simulation and subsequent testing. The blowers, situated in the instrument panels of three Toyota passenger cars, are categorized into two groups:

The side ducts which are located on each side of the instrument panel and consist of the following:

The side-duct of car 1 encompasses the original geometry utilized in the development of the CFD model. As detailed earlier, a countermeasure was devised to mitigate noise in this duct. Consequently, two distinct configurations were examined for this duct: The original configuration, which is the official duct mounted on the vehicle and is presented in **figure 6.2-1** and the modified one, which is the design alteration proposed by investigating the Proudman field of the CFD model, as described in **paragraph 5.2**. The perpendicular, circular edge removed can be seen in **figure 6.2-2**.
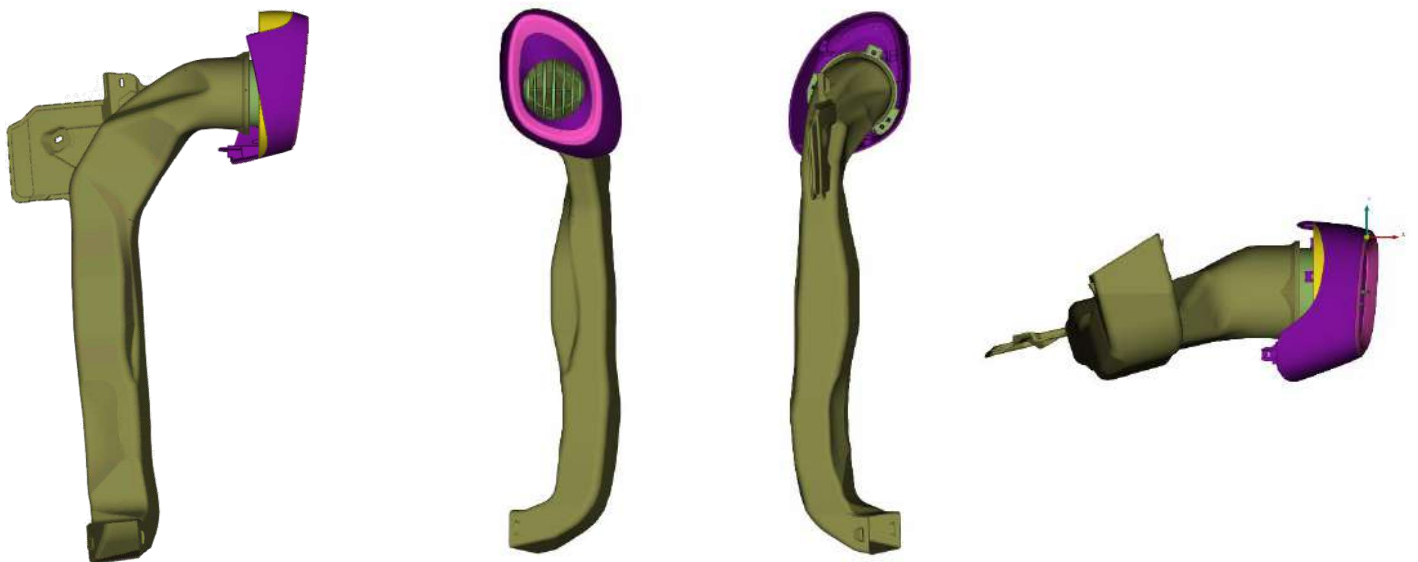


**Figure 6.2-1:** Side-duct assembly of car one.

**Figure 6.2-2:** Original register's housing (left) versus no ring design modification (right).

The side-duct of car 2, depicted in **figure 6.2-3**, has a smaller, circular register and an "S-shaped" duct. **Figure 6.2-4** depicts the side duct of car 3, notable for its distinctive orthogonal register and characterized by a coarse grid of blades.



**Figure 6.2-3:** Side-duct assembly of car two.



**Figure 6.2-4:** Side-duct assembly of car three.

The second category is the center ducts which are located on the center of the instrument panel. Center duct of car 2 is shown in **figure 6.2-5** and the one of car 3 is shown in **figure 6.2-6**.
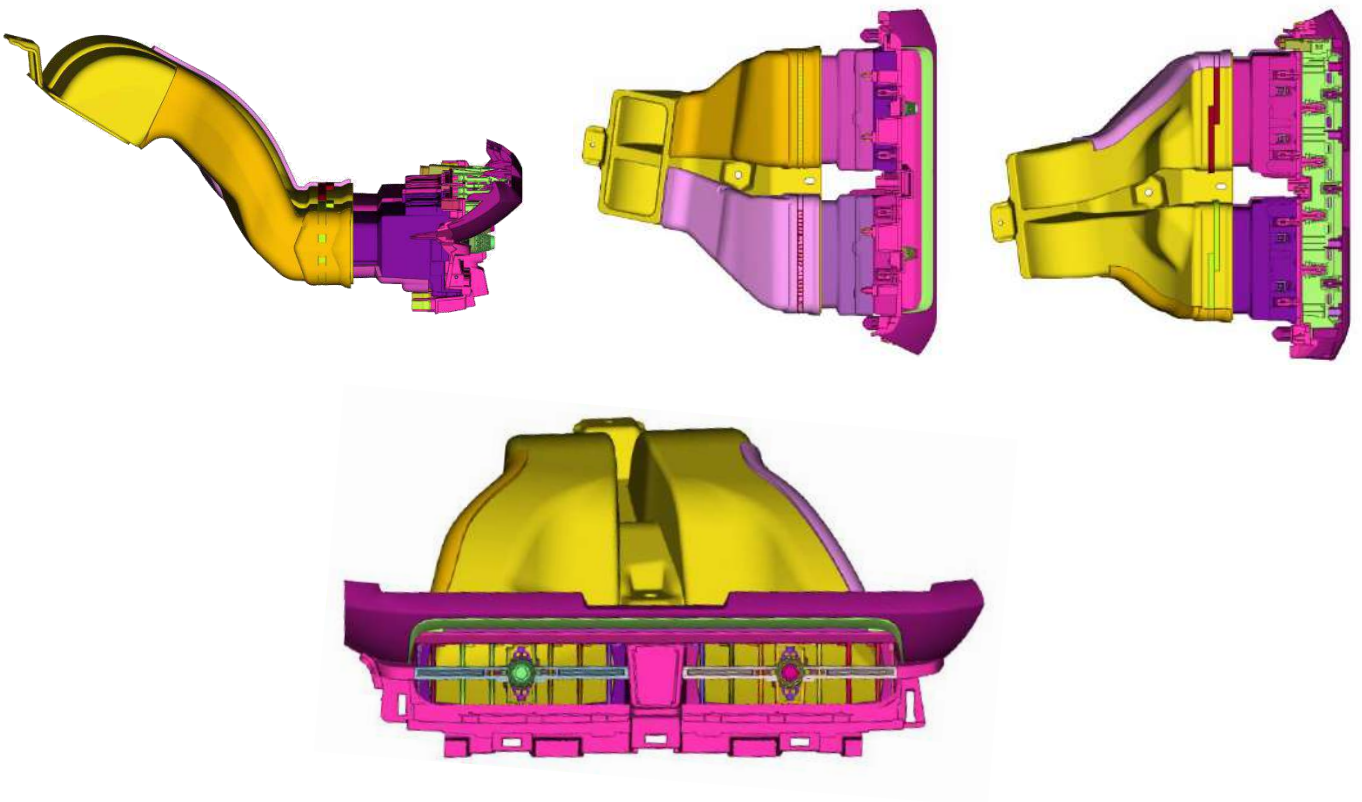


**Figure 6.2-5:** Center-duct assembly of car two.
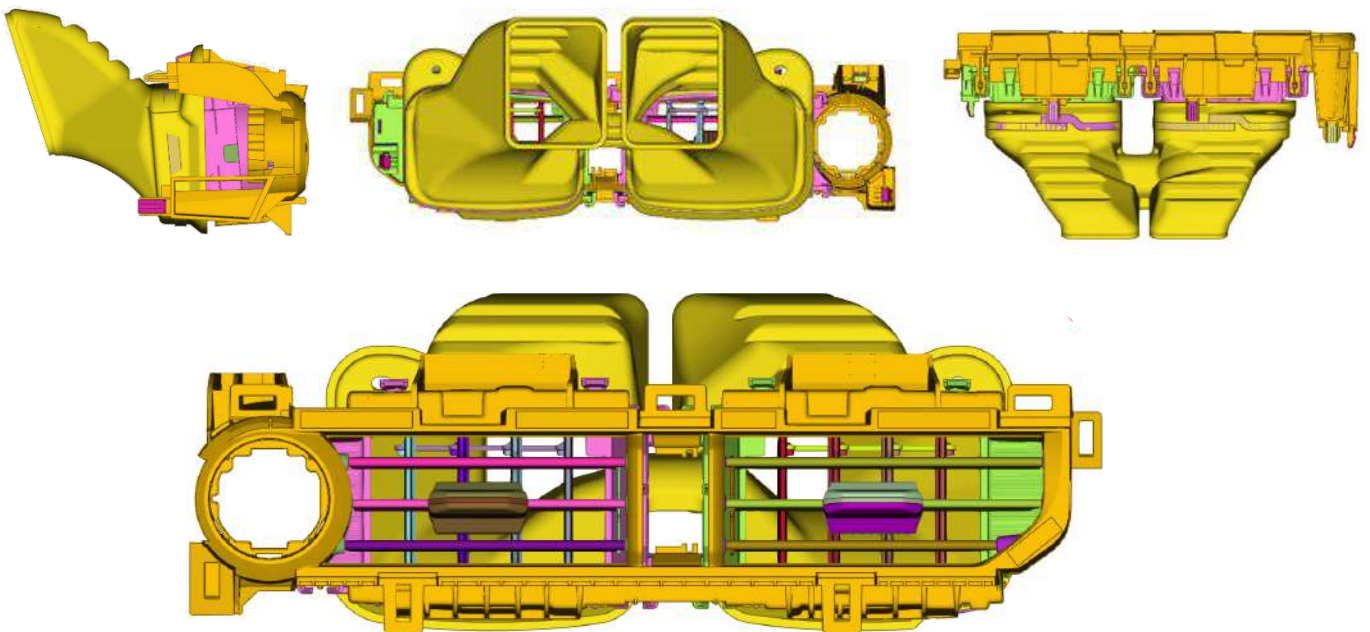


**Figure 6.2-6:** Center-duct assembly of car three.

## 6.3 Microphone Arrangement and Alignment

Four and a half-inch omnidirectional condenser microphones were utilized to ensure measurement independence from directional biases. These microphones were strategically positioned at four cardinal locations relative to an axis perpendicular to the center of the plane defined by a reference face, specifically chosen as the outlet section of the duct, located 1 meter downstream. Positioned 210 millimeters apart from each other, the microphones were arranged in a cross formation, as showcased in **figure 6.3-1**.

To guarantee precise microphone placement, a laser cross was employed. This apparatus produces two intersecting light beams, one vertical and one horizontal. The center of the resulting cross was aligned with the center of the register, representing the desired measurement point (the average of the four microphones). Prior to measurements, the microphones were aligned with these beams to ensure accurate positioning of the measurement points. Additionally, the same device was utilized to align the blades of the register with the vertical axis, corresponding to the nominal design configuration of the HVAC duct. This process is shown in **figure 6.3-2**.

Moreover, foam covers were utilized, to eliminate pseudo sound, meaning recording of pressure fluctuations caused by the non-uniform convected pressure field.
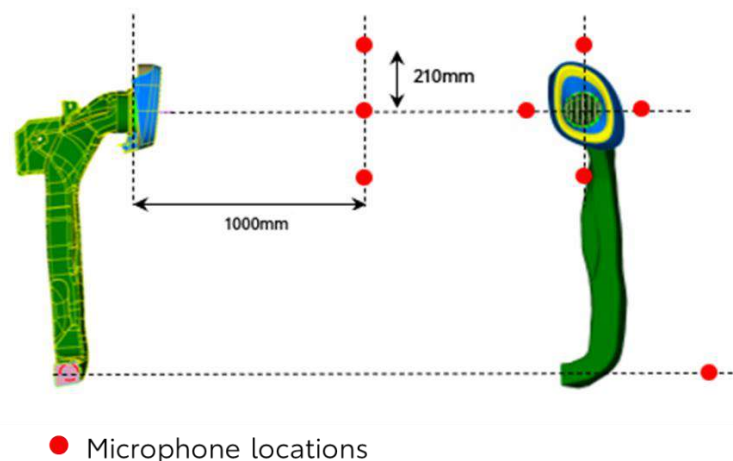


**Figure 6.3-1:** Positioning of microphones downstream of the blower assembly.



**Figure 6.3-2:** Alignment of test piece and microphones with the use of a laser cross.

## 6.4  Signal Analysis

The recordings were conducted using a modular 6-channel analogue-to-digital converter/acquisition system. To minimize random statistical errors, five independent measurements were performed for each tested configuration. Signals captured by each microphone were processed individually using a commercial sound post-processing software provided by TME, to extract the sound pressure spectrum in SPL units. The parameters utilized for this processing are outlined in **table 6.4-1**.

| Parameter | Value |
|---|---|
| Measurement length | 10 $sec$ |
| Sampling rate $f_s$ | 48 $kHz$ |
| Number of samples per measurement | 8192 |
| Windowing | Hanning Window 50% overlap |
| Frequency resolution | 5.86 $Hz$ |

**Table 6.4-1:** Summary of the experimental parameters used for the recording of sound measurements

The human ear does not perceive all frequencies of sound equally. It is most sensitive to mid – frequency sounds (around 2 to 5 kHz) and less sensitive to very low and very high – frequency sounds. The latter means that sounds at the medium frequencies need to have higher SPL levels to be perceived as equally loud as mid – frequency sounds.

In acoustics, the term weighting refers to the process of adjusting the sensitivity of sound level measurements to account for the human ear's varying sensitivity to different frequencies. A – weighting is the most commonly used frequency weighting and it mimics the frequency response of the human ear at moderate listening levels. The A – weighting curve provides a way to calculate sound levels that more closely approximate the perceived loudness of sounds, taking into account the non – linear relationship between sound pressure level and perceived loudness. It reduces the sensitivity to very low and very high frequency sounds, emphasizing mid – frequency sounds. A – weighting allows for measurements that correlate more closely with human perception of sound, which is crucial for accurately assessing noise exposure inside a vehicle's cabin.

It is underlined that throughout the context of this diploma thesis, the A – weighting function has been used in the post processing of the acoustic pressure signals.

## 6.5  Evaluation of Background Noise

Despite efforts outlined in **section 6.1** to mitigate background noise propagation in the experimental setup, a notable amount of extraneous sound reaching the microphones, unrelated to the blower segment, persists. As the computational model solely encompasses the geometries of the duct and register, omitting the remainder of the experimental pipeline, this additional noise is not accounted for and thus must be eliminated from the measurements.

To address this issue, the sound produced by the experimental setup excluding the blower was recorded using the same microphone configuration, positioned at the level of the adapter midpoint Specifically, two distinct configurations were measured: one encompassing all side ducts (**figure 6.5-1**) and another involving all center ducts (**figure 6.5-2**).




**Figure 6.5-1:** Microphone positioning for the measurement of background noise for all side duct configurations.



**Figure 6.5-2:** Microphone positioning for the measurement of background noise for all center duct configurations.

# 6.6 Measurement of Design Modification Inside the Vehicle's Cabin

Finally, measurements were conducted on both the original and modified configurations of the side duct of car number one inside the vehicle cabin. This was undertaken to ascertain whether the observed relative difference between the two registers, as measured on the bench, could also be discerned in a real-world scenario.

To facilitate this comparison, the vehicle was transported to the anechoic chamber where the bench measurements were conducted, aiming to minimize the influence of extraneous environmental noise during the measurement process, which could potentially compromise the

accuracy of the results (**figure 6.6-1**). Due to the limited availability of each design configuration, it was determined that the impact of the driver's-side blower would be assessed (**figure 6.6-2**) while sealing the outlet of the passenger-side blower at the section where the duct and the register are interconnected using duct tape, as shown in **figure 6.6-4**. Two microphones were strategically positioned at the location corresponding to where the driver's ears would be situated, as illustrated in **figure 6.6-3**. It is underlined that the results of the car measurements are considered confidential from TME and therefore are cannot be included.



**Figure 6.6-1:** Placement of the vehicle inside the anechoic chamber to minimize the effect of unwanted environmental noise in the measurement.



**Figure 6.6-2:** Driver's view inside the cabin of passenger car number one. The driver's – side register is measured.



**Figure 6.6-3:** Positioning of microphones in the level of the driver's ears.

It is pertinent to note that all measurements were conducted under the accessory mode, denoting a stationary vehicle state with the engine turned off. Each measurement iteration was repeated five times to mitigate the influence of random statistical errors. Additionally, every configuration underwent testing for three distinct volumetric flow rates, denoted as scale 1, 3 and 7, on a range where 1 represents the lowest volumetric flow rate observed in the bench experiment, 3 denotes a medium flow, and level 7 indicates the highest one. Throughout the entire procedure, the HVAC mode was configured to face mode, with a temperature set to $20℃$ (**figure 6.6-5**).





**Figure 6.6-5:** HVAC mode settings. Blower was set to face mode, temperature to $20℃$ and the flux to the respective scale from 1 to 7.

**Figure 6.6-4:** Sealing of the passenger – side blower to avoid impairing the results of the measurement. The duct tape put on the outer casing of the register is to visualize that it has been sealed.

# Chapter 7:

# Calibration of the Steady-State Model with New Experimental Measurements

## 7.1 Post Processing of Experimental Measurements

Following the acquisition of experimental data detailed in **section 6** of this thesis, the subsequent task involved assessing their correlation with the corresponding CFD results. Initially, the pressure signals over time captured by the four microphones for each measurement were transformed into SPL utilizing the methodology outlined in **paragraph 4.1**, leveraging commercial software supplied by TME. The resultant plot is referred to as the Narrowband spectrum, indicating that the frequency range of interest is limited to a relatively small segment of the entire frequency spectrum.

Subsequently, the narrowband spectra underwent conversion into 1/3 octave spectra. This transformation offers a simplified representation, particularly beneficial for handling intricate signals like those observed in the experiment, as it provides a more generalized depiction of the frequency distribution. Furthermore, 1/3 octave bands correspond with the critical bands of human hearing, rendering them more suitable for applications where human perception of sound is a key consideration.

Following the acquisition of the 1/3 octave SPL-frequency curves, the average value from each microphone was computed to simulate the anticipated measurement at the center of the microphone-cross arrangement. This calculation also accounted for any random statistical errors that might have been introduced by relying on the signal from just one microphone.

## 7.2 Investigation of Frequency Range Interest Region

As mentioned in **paragraph 4.1**, determining the OASPL value from a given experimental curve involves integrating the SPL values across a defined frequency range. Establishing the range of integration was found to be crucial for ensuring the accuracy of the proposed model. The objective was to identify a specific range that would yield the optimal alignment between the two quantities. The primary criteria used for evaluation were the linear correlation factor and the maximum discrepancy between the CFD and experimental data, as these factors serve as indicators of the divergence between the two quantities.

It is important to highlight that the initial correlation with the experimental measurements from [36] was established by integrating across the entire frequency spectrum provided by each curve, spanning from 5 to 20,000 Hz. However, it has been observed that the aeroacoustic phenomena

relevant to HVAC measurements typically manifest within a narrower frequency range of 125 to 5000 Hz. For instance, below this range, the current peak tends to distort the results.

## 7.3 Removal of Background Noise

Another significant aspect of investigation pertained to the examination of the impact of background noise on the experimental measurements. Initially, the effect of background noise was deemed relatively insignificant and thus was disregarded during the post-processing. However, it became apparent that particularly in lower frequencies, the measured values of background noise occupied a significant portion of the respective measurement curve, potentially compromising the accuracy of the results. It is important to reiterate that the computational model specifically examines the sound generated within the stationary parts of the blower. Therefore, opting not to exclude all other noise-generating features from the measurements would be a substantial oversight, resulting in a final outcome that does not accurately represent the model's real accuracy. Consequently, the decision was made to subtract the background noise 1/3 octave spectrum from the spectrum pertaining to the measurement of the complete blower assembly in the bench experiment setup.

The process to subtract the background noise followed a specific protocol: SPL values across the frequency spectrum for 1/3 octave spectra were obtained by averaging the readings from the four microphones. For each frequency, the SPL value corresponding to background noise was deducted from the original measurement, resulting in the generation of a new curve that purportedly represents the genuine noise generated by the HVAC duct. This methodological approach is depicted in **figure 7.3-1**.
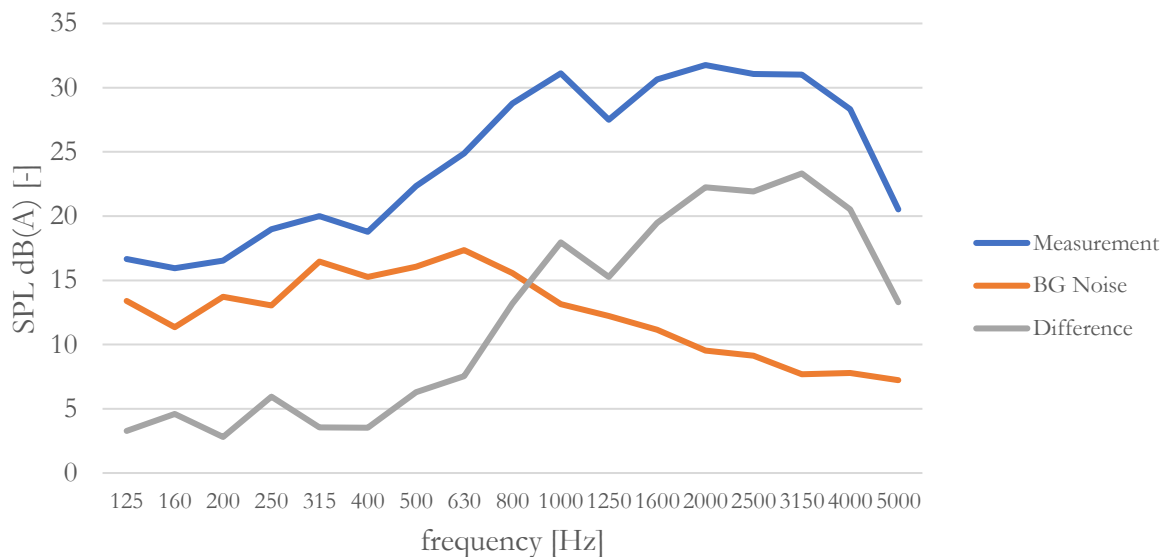


**Figure 7.3-1:** Direct comparison between the 1/3 octave spectrum for the overall blower assembly, the measured background noise and their relative difference for a certain testing configuration at a specific volumetric flow.

Following the post processing method that was described in **paragraph 7.2**, the OASPL value for every tested configuration was calculated by the integration of the latest curve, inside the range of $125 - 5000\ Hz$.

The effect of the background noise extraction can be visualized through the linear correlation factor of the calibration graph of **figure 7.3-2**. It is evident that in the case where the background noise is excluded from the experimental values, the deviation from the interpolation line is reduced, hence benefiting the accuracy of the CFD model as a whole.
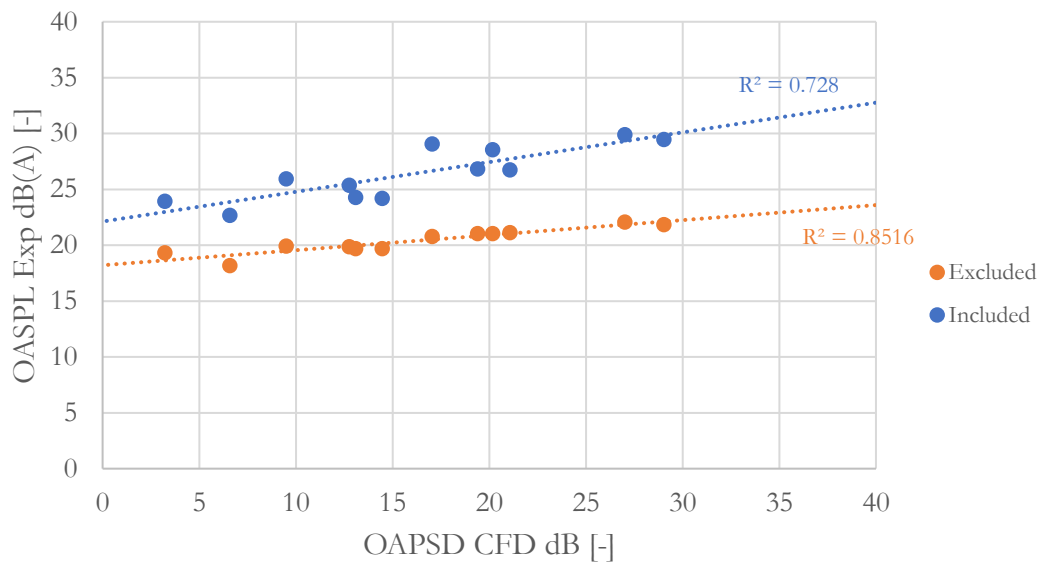


**Figure 7.3-2:** The effect of the background noise expressed by the deviation of the measurement points from the interpolation line.

Eliminating background noise could significantly enhance the accuracy in the work of [36] and might be the primary reason for the discrepancy between the DNC and the experimental results in the high-frequency region, as depicted in figure 4-1.

## 7.4 Calibration of the Steady-State Model with Experimental Measurements

A direct comparison is drawn between the experimental values and those derived from the CFD analysis. It is emphasized that the presented results are based on the averaged curve of the four microphones, with a frequency integration range of 125-5000 Hz, and background noise has been subtracted from all measurements. The graph of **figure 7.4-1** reveals a linear correlation factor of $R^2 = 0.7688$, indicating that the two quantities plotted on each axis exhibit a linear relationship.

**Figure 7.4-2** provides arguably the greatest amount of information regarding the model's ability to predict the aerodynamically induced noise. Specifically, in this graph, the absolute deltas between each testing configuration and the nominal condition of side-duct of car number one are plotted for the experiment and the CFD respectively. Afterwards, their relative difference is calculated by subtracting the experimental delta from the CFD one, therefore obtaining the

absolute error between the two. The latter stands as the indicator for the performance of the CFD model.
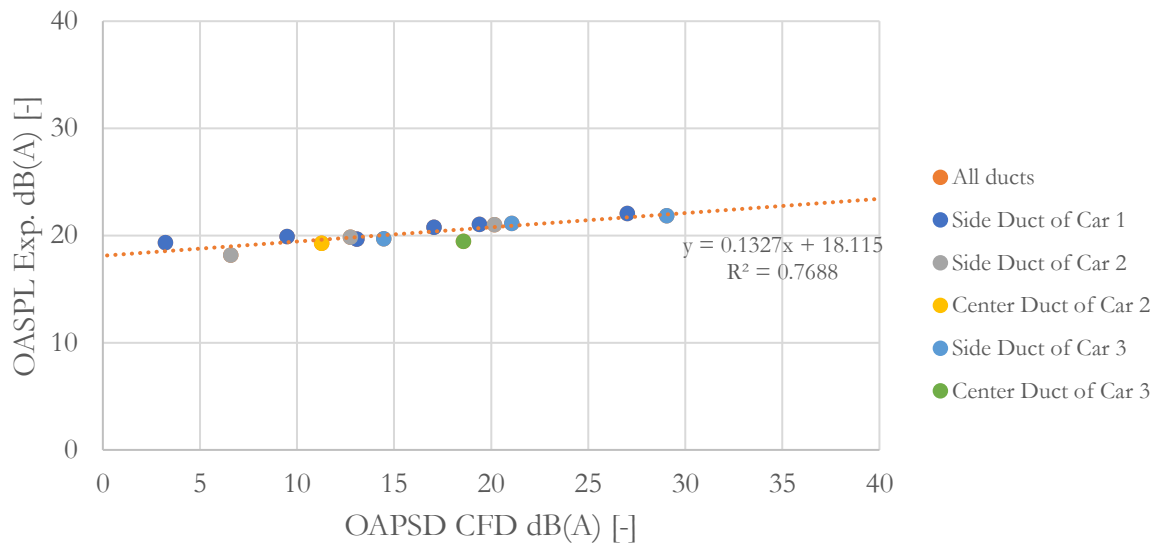


**Figure 7.4-1:** Correlation of Proudman's steady-state CFD model with experimental measurements.
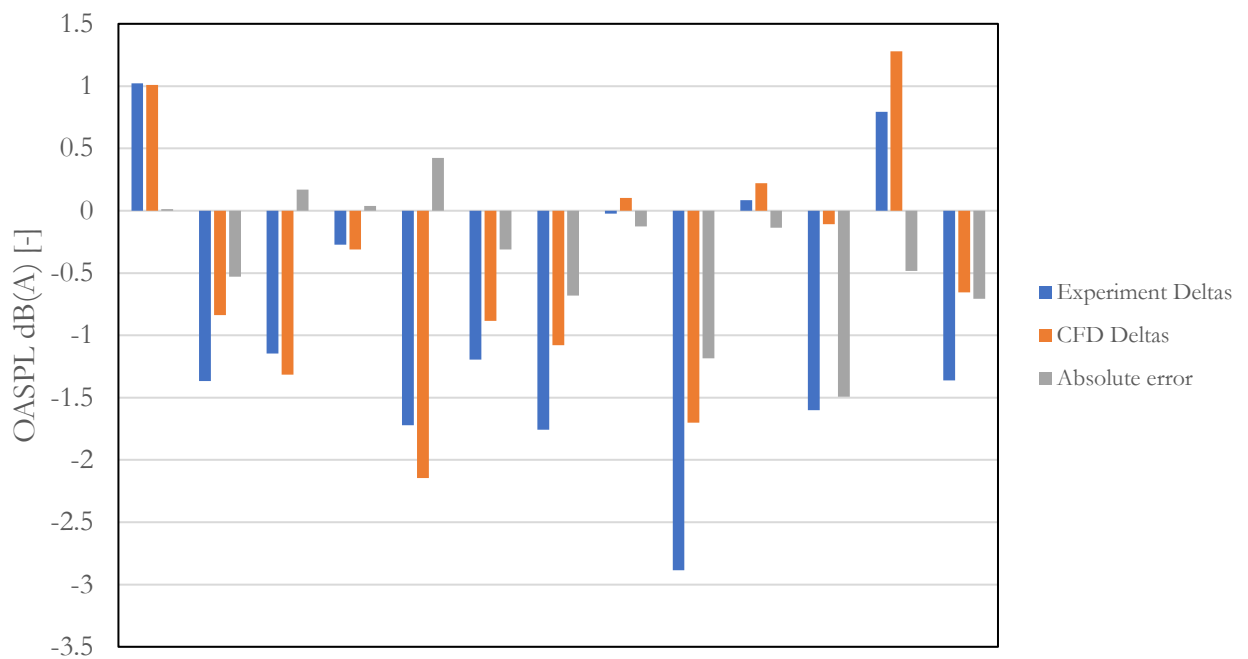


**Figure 7.4-2:** Absolute differences for the experiment and the CFD in comparison to side duct of car number one at the nominal volumetric flow rate. The relative difference of CFD and experiment stands as an evaluation criterion.

In the graph of **figure 7.4-2**, the sign of the experimental and CFD deltas showcases the relative improvement or deterioration of each duct compared to a standard benchmark. It is evident that the sign of these two quantities is the same for every measurement configuration (apart from one particular measurement, where the experimental and CFD deltas are very close to $0$). This is of great importance, as it proves that the trend of relative differences is captured by the steady-state

model, so this means it can classify all ducts from the loudest to the quietest. Finally, the biggest offset between the two quantities reaches up to $1.5\ dB$, therefore defining the accuracy of the model.

Once again, the calibration factors for the volumetric Proudman term as defined in **section 5.3** are defined as follows:

$$G_V = 0.1327, b_V = 18.115$$

## 7.5 Calibration of Proudman's Surface Term with Experimental Measurements

In low-speed aeroacoustics noise is primarily governed by dipole sources. Hence, an endeavor was made to compute the OAPSD directly on the surface of the blower, as outlined in **equation 2.5-3b**. Specifically, the surface Proudman term was integrated across the area encompassing the duct and register, yielding an OAPSD value indicative of the sound emission on the surface originating from dipole noise sources.

**Figure 7.5-1** shows that the dispersion of the points from the linear interpolation equation is significantly less. As a matter of fact, the linear correlation factor value equals $R^2 = 0.8587$, hence stating that the surface integration is a more sophisticated evaluation metric in the case of low-speed aeroacoustics applications, such as the flow inside an HVAC duct.
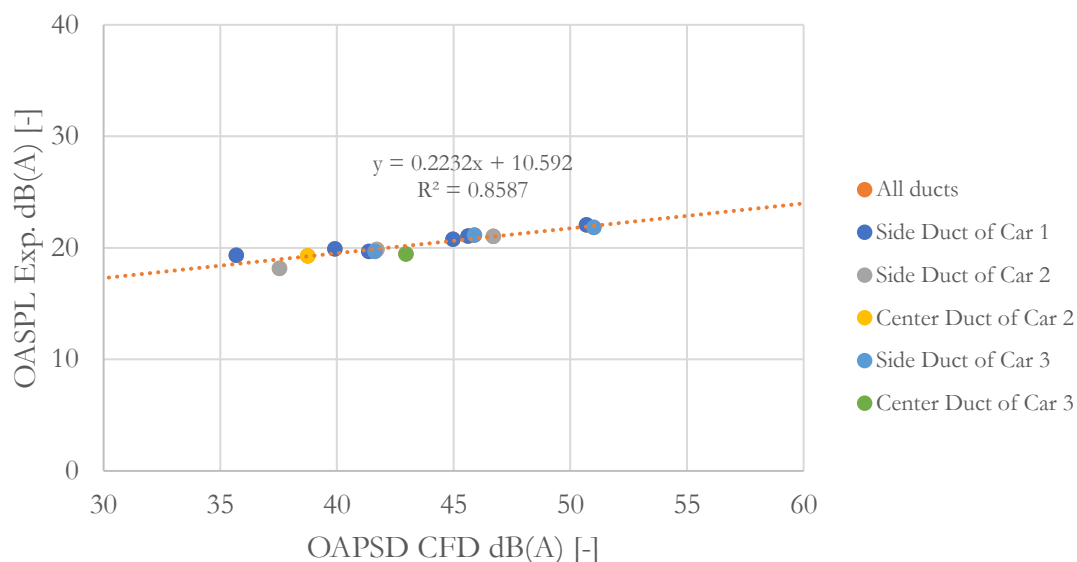


**Figure 7.5-1:** Correlation of Proudman's surface term with experimental measurements.

According to the experimental and the CFD deltas, as shown in **figure 7.5-2**, this time the maximum offset between the two is reduced to $1.1\ dB$, so both evaluation criteria seem to be benefited in the case of the surface term, therefore rendering this metric more suitable.
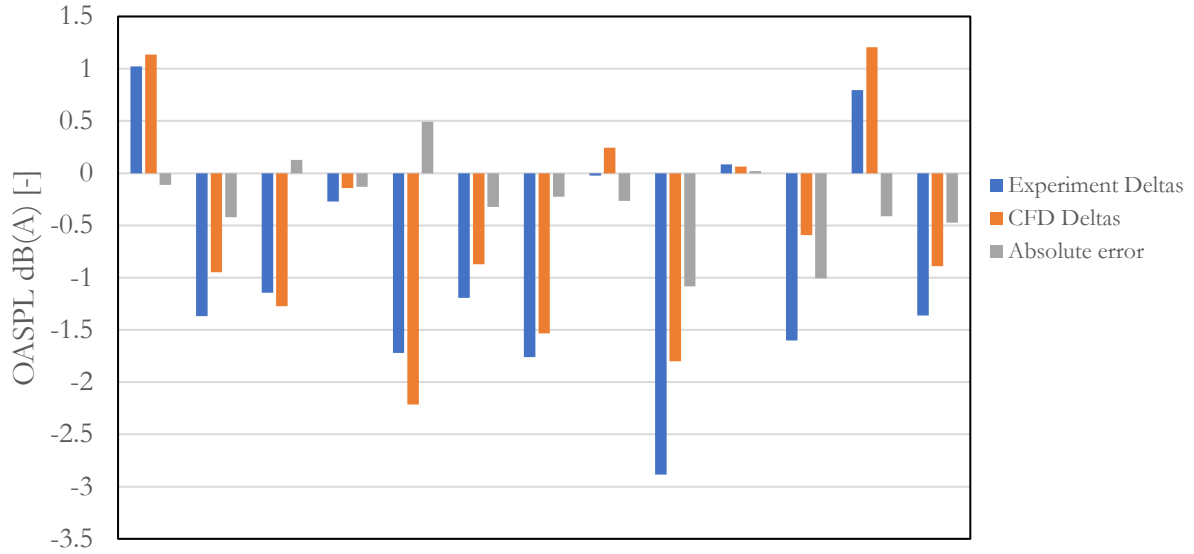
**Figure 7.5-2:** Absolute differences for the experiment and the CFD in comparison to side duct of car number one at the nominal volumetric flow rate for the surface Proudman component.

The calibration factors for the surface Proudman term are defined as follows:

$$G_S = 0.2232, b_S = 10.592$$

# 7.6 Evaluation of Design Countermeasure's Performance

Based on the calibration factors of the surface Proudman term, the relative improvement of the design countermeasure described in **section 4.2** is re-examined. **Table 7.6-1** showcases that between the nominal side-duct of car one and its design countermeasure, the experiment predicts a 1.14 dBA reduction in overall acoustic emission, while the respective value for the CFD is 1.27 dB, which results in a relative accuracy of just 0.13 dB between the two, which is barely noticeable from a human perspective. As far as the relative error of the two is concerned, in the first case, the experiment presents a 5.44% decrease in OASPL, while CFD predicts 6.13%. This results in a 0.69% relative accuracy between the two, which means that the performance of the design countermeasure was accurately predicted.

| Evaluation Method | Experiment | CFD |
|---|---|---|
| Relative reduction | 5.44% | 6.13% |
| Absolute Delta | 1.14 dBA | 1.27 dB |

**Table 7.6-1:** Direct comparison between the experimental measurements and the CFD model for the evaluation of the design countermeasure.

# Chapter 8:

# Conclusions

This thesis delves into the investigation of aerodynamically induced sound phenomena within automotive HVAC systems through the application of CFD. Throughout a six-month industrial placement at TME, a steady-state, incompressible CFD model was devised in the OpenFOAM® software, leveraging Proudman's acoustic analogy to estimate acoustic power. The RANS equations were solved and the $k - \varepsilon$ turbulence model was employed, coupled with wall functions. Notably, this newly developed simulation model achieves a substantial reduction in computational cost, requiring only 1.5 hour on 512 CPUs compared to approximately 4 days with the DNC model of [36]. This is of great importance for an application that involves numerous intermediate design modification decisions, as it manages to speed up the development process significantly.

Furthermore, a technique for visualizing noise sources was devised to aid in the aeroacoustic advancement of HVAC ducts by enabling the quantification of sound generation and its direct association with geometric features. Two visualization techniques were developed, regarding the volumetric and the surface term of acoustic power provided by Proudman's acoustic analogy. Utilizing this tool, a design intervention was implemented in the register of the side-duct of car 1, where a circular perpendicular edge was removed to examine its effect on the generation of acoustic power. This modification yielded a 1.14 dBA relative variation according to the obtained experimental measurements compared to the initial configuration and a 0.13 dBA relative agreement between the steady-state CFD simulation and the experimental results, therefore signifying the ability of the model to provide qualitative and quantitative feedback to the engineer. These post-processing methodologies enable the identification of noise generating features and areas of interest, serving as valuable tools for improving the aeroacoustic performance of a given geometry.

A novel methodology for comparing the outputs of the steady-state CFD model with experimental measurements and unsteady models has been developed. This approach introduces a new metric for evaluating aeroacoustic performance: the Overall Power Spectral Density (OAPSD). In this method, the pressure time signals from an unsteady model or measurements are transformed into Overall Sound Pressure Level (OASPL), which represents the total noise emission at a specific point, thus enabling the direct comparison with the steady-state data derived from Proudman's analogy.

The steady-state CFD model was ultimately validated against experimental data obtained from measuring various HVAC ducts of Toyota passenger cars inside an anechoic chamber. The background noise was measured separately and subtracted from the results, significantly improving the accuracy of the correlation between computational and experimental data. The validation demonstrated a maximum relative difference of 1.1 dBA between the experimental and CFD

results, which is within the acceptable limits set by the company for sound emission. It was noted that the surface term of Proudman's analogy offered slightly better accuracy than the volumetric term, which is expected in a low-Mach number application.

However, the use of a steady-state approach comes at the expense of losing frequency spectrum information, as a temporal solution is required to detect tonal noise. This limitation means that identifying which geometric features are responsible for specific frequency excitations is not possible. Additionally, we cannot determine whether the model underestimates or overestimates the generated noise within the safety margin of 1.1 dB, thus preventing us from accurately ranking ducts or design modifications of the same duct that exhibit very similar noise levels.

In conclusion, this thesis underscores the efficacy of Proudman's acoustic analogy in low-speed aeroacoustic applications of interior flows, aiming to consistently achieve optimal results in minimal time.

Derived from the subject of this thesis, the following fields present great interest for future study and improvement:

- ✓ Use of the steady-state model for shape optimization of a given duct for minimization of the acoustic power over the computational domain, utilizing the adjoint optimization method.
- ✓ In case the engineer wants to detect tonal noise, Curle's analogy should be used, which is less computationally demanding than DNC.
- ✓ Application of Proudman's acoustic analogy to external aerodynamics applications for higher Re numbers (e.g. for a side car mirror).

Εθνικό Μετσόβιο Πολυτεχνείο

Σχολή Μηχανολόγων Μηχανικών

Τομέας Ρευστών

Μονάδα Παράλληλης Υπολογιστικής Ρευστοδυναμικής
& Βελτιστοποίησης

# Υπολογιστικό Μοντέλο βασισμένο σε Χρονικά Μόνιμες Εξισώσεις για την Πρόλεξη Αεροδυναμικά Επαγόμενου Θορύβου σε Συστήματα Κλιματισμού Αυτοκινήτων

Διπλωματική Εργασία

**Ιωάννης Χονδροματίδης**

Ακαδημαϊκός Επιβλέπων:

Κυριάκος Χ. Γιαννάκογλου, Καθηγητής ΕΜΠ

Βιομηχανικός Επιβλέπων:

Antoine Delacroix, Senior Manager TME

Αθήνα, 2024

# Εκτενής Περίληψη Διπλωματικής Εργασίας

## 1 Εισαγωγή

Τα τελευταία χρόνια, στον τομέα της αυτοκίνησης είναι ολοένα κι εμφανέστερη η επιθυμία μείωσης του επιπέδου θορύβου των οχημάτων. Έρευνες δείχνουν πως η συνεχής έκθεση σε θόρυβο οδηγεί στην κόπωση του οδηγού, αυξάνοντας έτσι σημαντικά την πιθανότητα πρόκλησης τροχαίων ατυχημάτων [1], [16] ή ακόμη και καρδιακών παθήσεων [3], [18].

Η τάση αυτή ευνοείται σημαντικά από τη μαζική παραγωγή και πώληση υβριδικών και αμιγώς ηλεκτρικών οχημάτων, ελλείψει της συνεχόμενης λειτουργίας του κινητήρα. Σε αυτά τα οχήματα, σε συνθήκη ακινησίας, ο αεροδυναμικός θόρυβος που παράγεται από το σύστημα κλιματισμού αποτελεί τη μοναδική πηγή θορύβου (βλ. **σχήμα 1**), οδηγώντας τις κατασκευάστριες εταιρίες στη μελέτη και τον ανασχεδιασμό των συστημάτων αυτών.
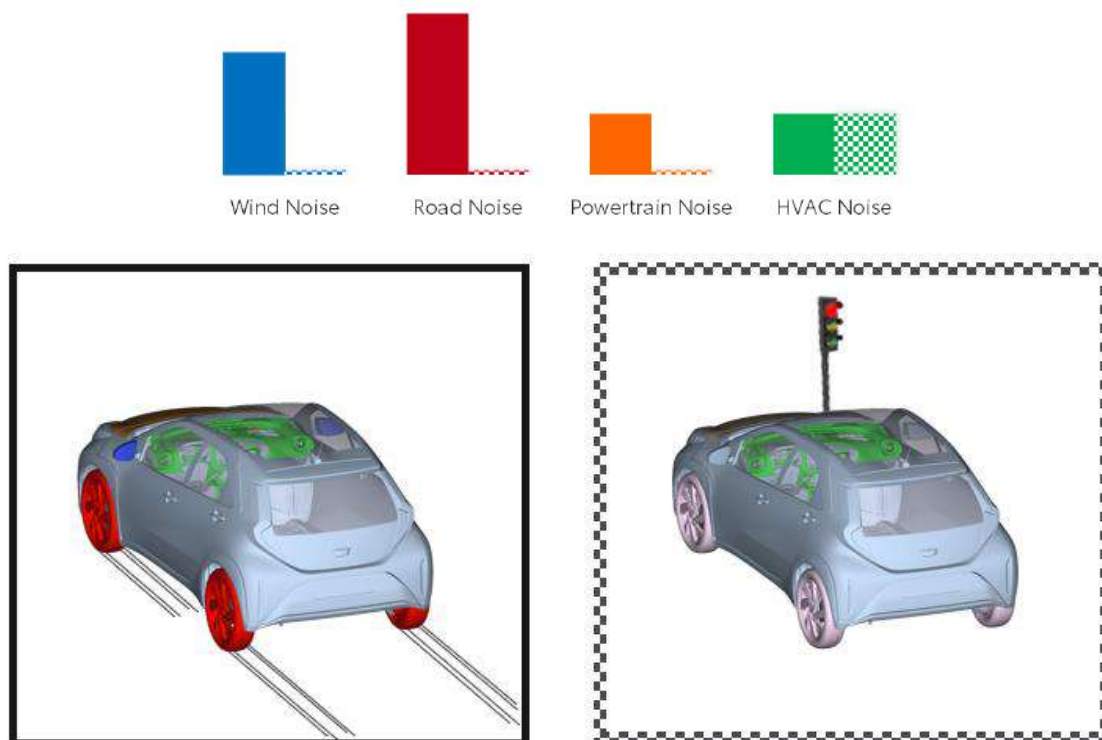


**Σχήμα 1:** *Σύγκριση έντασης πηγής θορύβου για BEVs και HEVs κατά την κίνηση (αριστερά) και σε στατική κατάσταση (δεξιά). Οι συμπαγείς μπάρες αντιπροσωπεύουν τις συνθήκες κίνησης, ενώ οι καρό μπάρες απεικονίζουν τις στατικές συνθήκες. (Σχήμα με πηγή προέλευσης την TME).*

Η διπλωματική αυτή εργασία αφορά τη μελέτη του αεροδυναμικά επαγόμενου θορύβου από τα στατικά στοιχεία του συναρμολογημένου συνόλου του αγωγού κλιματισμού, καταδεικνυόμενα με

πράσινο χρώμα στο **σχήμα 2**. Αποτελεί συνέχεια προηγούμενης διπλωματικής εργασίας που πραγματοποιήθηκε στη Μονάδα Παράλληλης Υπολογιστικής Ρευστοδυναμικής & Βελτιστοποίησης του Εθνικού Μετσόβιου Πολυτεχνείου [36] και αφορά την ανάπτυξη ενός υπολογιστικού μοντέλου βασισμένου σε χρονικά μόνιμες εξισώσεις με χρήση της ακουστικής αναλογίας του Proudman. Το μοντέλο αναπτύχθηκε στο λογισμικό OpenFOAM®.
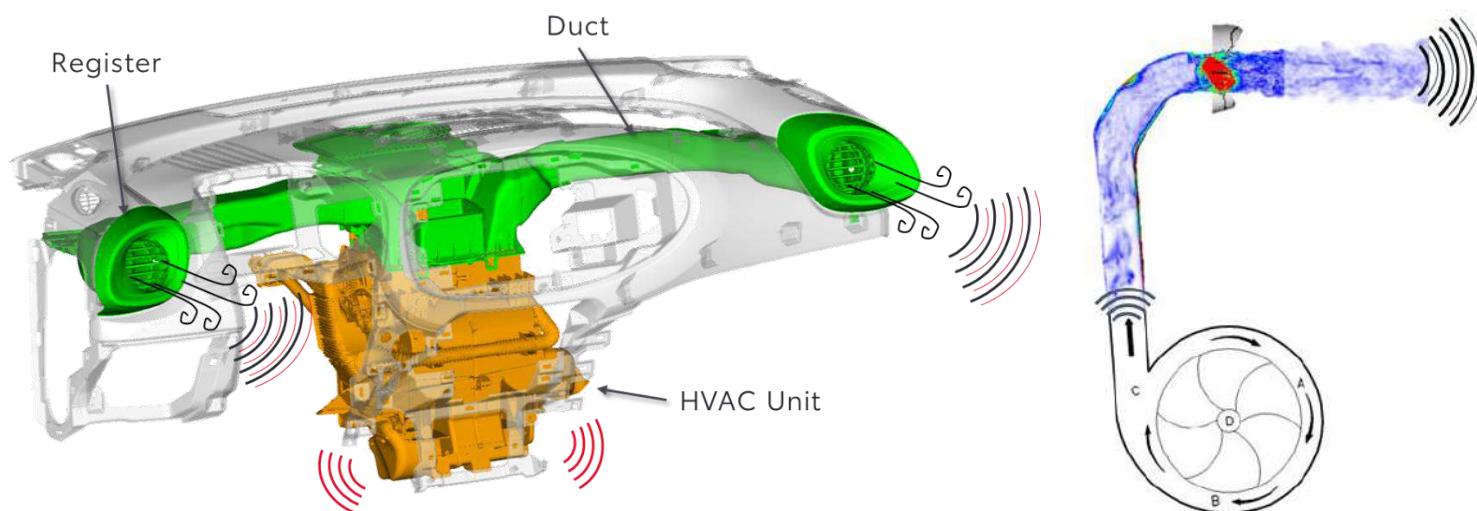


**Σχήμα 2:** *Το συναρμολογημένο σύνολο του συστήματος κλιματισμού και το υποσύστημα των αεραγωγών (αριστερά). Πρόκληση αεροδυναμικά επαγόμενου θορύβου μέσα στον αγωγό (δεξιά). (Σχήμα με πηγή προέλευσης την TME).*

## 2  Αεροδυναμικός Θόρυβος

Ο ήχος στη ρευστοδυναμική εκφράζεται ως διαταραχές μικρού πλάτους των μεγεθών της πίεσης και της πυκνότητας μέσα σε ένα εργαζόμενο μέσο και μπορεί να θεωρηθεί ως μια επαλληλία ακουστικής διαταραχής και αδιατάραχτης ροής [43]. Κατά συνέπεια, η συνήθης προσέγγιση αντίστοιχων προβλημάτων για τον ευθύ υπολογισμό των ακουστικών ποσοτήτων αφορά μη-μόνιμα μοντέλα ροής συμπιεστού ρευστού, τα οποία αυξάνουν σημαντικά το υπολογιστικό κόστος [36].

Εναλλακτική μέθοδο αποτελεί η χρήση ακουστικών αναλογιών, οι οποίες αποσκοπούν στη μείωση των υπολογιστικών απαιτήσεων, με γνωστότερες αυτές του Lighthill [30], του Curle [10] και των Ffowcs Williams-Hawkings [2]. Παρά την επιτυχή μείωση του υπολογιστικού κόστους, οι μέθοδοι αυτές βασίζονται επίσης σε μη-μόνιμες εξισώσεις, γεγονός που δρα περιοριστικά στη χρήση τους σε καθημερινή χρήση.

Η ακουστική αναλογία του Proudman [46], σύμφωνα με την οποία ο ήχος προέρχεται από την ομογενή ισότροπη τύρβη, προσφέρει αναλυτικές εκφράσεις για την εκτίμηση της έντασης του θορύβου από τις ποσότητες της τυρβώδους κινητικής ενέργειας $k$ και του ρυθμού καταστροφής της $\varepsilon$ του μοντέλου τύρβης. Το τεράστιο πλεονέκτημα αυτής της αναλογίας είναι πως οι ποσότητες αυτές μπορούν να αποκτηθούν από μοντέλα ροής που βασίζονται αποκλειστικά στις χρονικά μόνιμες εξισώσεις, μειώνοντας δραστικά το υπολογιστικό κόστος. Το υπολογιζόμενο μέγεθος είναι η παραγόμενη ακουστική ισχύς ανά μονάδα όγκου, η οποία μοντελοποιεί τις τετραπολικές πηγές θορύβου.

Ακόμη, στο πλαίσιο αυτής της διπλωματικής εργασίας, μελετάται ένας επιφανειακός όρος που αφορά αντίστοιχα τις διπολικές πηγές θορύβου, οι οποίες έχουν εν γένει σημαντικά μεγαλύτερη επίδραση σε

εφαρμογές χαμηλού αριθμού Mach, όπως η ροή σε έναν αεραγωγό. Σε σύγκριση με το υπολογιστικό μοντέλο μη-μόνιμου συμπιεστού ρευστού του [36] που υπολογίζει ευθέως την παραγωγή και διάδοση των ακουστικών διαταραχών στο ίδιο υπολογιστικό χωρίο, το μοντέλο που αναπτύσσεται στη διπλωματική αυτή εργασία βασιζόμενο στην αναλογία του Proudman επιτυγχάνει μείωση του κόστους από περίπου 4 ημέρες σε μόλις 1.5 ώρα σε 512 επεξεργαστές. Σημειώνεται πως η ακρίβεια των υπολογισμών θυσιάζεται εντός λογικών ορίων, με τα τελικά αποτελέσματα να περιορίζουν την απόκλιση του υπολογιστικού μοντέλου με την πραγματικότητα σε λιγότερο από 4%.

# 3  Υπολογιστική Μοντελοποίηση

Στο πλαίσιο της εργασίας γίνεται χρήση των χρονικά μόνιμων εξισώσεων Reynolds-Averaged Navier-Stokes (RANS), καθώς και του μοντέλου τύρβης $k - \varepsilon$ [6], [58]. Το τελευταίο έχει αναπτυχθεί ειδικά για επίπεδα στρώματα διάτμησης και ροές με ανακυκλοφορία και είναι συνήθως χρήσιμο για ροές με σχετικά μικρές κλίσεις πίεσης αλλά και ροές όπου οι τάσεις Reynolds είναι οι επικρατέστερες [58]. Ακόμη, γίνεται χρήση συναρτήσεων τοίχου, οι οποίες λαμβάνουν υπόψη την επίδραση των τυρβωδών δυνάμεων κοντά στα στερεά τοιχώματα, επιτρέποντας τη χρήση ενός σχετικά αραιότερου πλέγματος στις περιοχές αυτές, μειώνοντας έτσι το υπολογιστικό κόστος. Για την επίλυση του ροϊκού προβλήματος γίνεται χρήση του αλγορίθμου SIMPLE [7], [40] ο οποίος διατυπώνει και λύνει μια μερική διαφορική εξίσωση για την πίεση.

Το μοντέλο του αεραγωγού μελετάται ανεξάρτητα και εκτός του πλαισίου του αυτοκινήτου. Για τις ανάγκες της προσομοίωσης δημιουργείται μια τεχνητή βολβοειδής γεωμετρία για την παροχή ροής στον αγωγό (**σχήμα 3**). Κατάντι της αναλυόμενης γεωμετρίας τοποθετείται ένα χωρίο μορφής καμπάνας εντός του οποίου πραγματοποιείται η ομαλοποίηση της ροής, που αποτελεί το όριο εξόδου. Ακόμη, γίνεται χρήση ζωνών πύκνωσης του πλέγματος στον ομόρου του αεραγωγού, όπου το πλέγμα γίνεται σταδιακά αραιότερο για εξοικονόμηση πόρων.
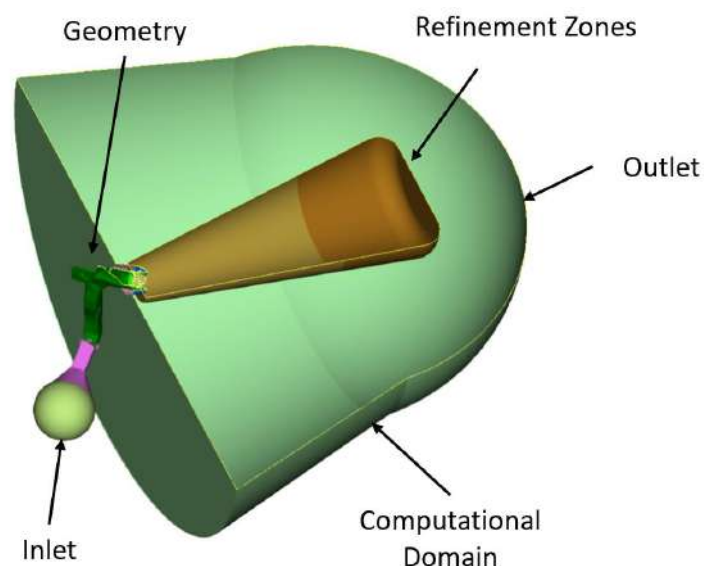


**Σχήμα 3:** Το υπολογιστικό χωρίο. Παρουσίαση της τεχνητής εισόδου βολβοειδούς σχήματος (κίτρινο), της επέκτασης της εισόδου (ροζ), του χωρίου αποφόρτισης (ανοιχτό πράσινο) που αποτελεί το όριο εξόδου και του πλαϊνού-αεραγωγού του οχήματος 1 (σκούρο πράσινο). Ορισμός των ζωνών πύκνωσης 1 (ανοιχτό πορτοκαλί) και 2 (σκούρο πορτοκαλί), με πυκνό και αραιό πλέγμα αντίστοιχα.

# 4 Βαθμονόμηση του Χρονικά Μόνιμου Μοντέλου με Πειραματικές Μετρήσεις

Το προτεινόμενο υπολογιστικό μοντέλο βαθμονομείται, σε πρώιμο στάδιο, με τις πειραματικές μετρήσεις και το μοντέλο συμπιεστού ρευστού προηγούμενης διπλωματικής εργασίας [36]. Βασικό πρόβλημα για τη συσχέτιση των προηγουμένων αποτελεί η απουσία πληροφορίας στο φάσμα της συχνότητας για το μόνιμο μοντέλο, ως αποτέλεσμα της απαλοιφής των χρονικών όρων. Για να καταστεί δυνατή αυτή η σύγκριση, τα μη-μόνιμα αποτελέσματα του [36] υπόκεινται σε μια αναγωγή σε μόνιμες ποσότητες. Έτσι, εξάγεται η ποσότητα της Συνολικής Μέσης Στάθμης Ηχητικής Πίεσης (OASPL), που αναπαριστά τη συνολική ηχητική εκπομπή σε ένα σημείο κατάντι της διάταξης που μελετάται.

Αντίστοιχα, για το μόνιμο μοντέλο του Proudman που αναπτύσσεται στη διπλωματική εργασία, προτείνεται ένα νέο μέγεθος για την εκτίμηση της ηχητικής εκπομπής, η Συνολική Μέση Στάθμη Ακουστικής Ισχύος (OAPSD). Η ποσότητα αυτή υπολογίζεται με ολοκλήρωση της ακουστικής ισχύος του Proudman σε όλο το υπολογιστικό χωρίο και αποτελεί επίσης μια ένδειξη της ηχητικής εκπομπής εντός του εκάστοτε επιλεγόμενου όγκου ελέγχου.

Τα αποτελέσματα των υπολογιστικών μοντέλων του [36] και της παρούσας εργασίας τοποθετούνται σε παράθεση με τις πειραματικές μετρήσεις του [36], όπως παρουσιάζεται στο **σχήμα 4**. Τα μεγέθη των 2 αξόνων παρεμβάλλονται γραμμικά για κάθε μια από τις προηγούμενες περιπτώσεις, παρουσιάζοντας έντονη γραμμική συσχέτιση ($R^2 \approx 1$). Το γεγονός αυτό καθιστά δυνατή την εκτίμηση της αναμενόμενης πειραματικής μέτρησης οποιασδήποτε διάταξης, βασισμένη στο αποτέλεσμα του υπολογιστικού μοντέλου. Βέβαια, στο πλαίσιο της βαθμονόμησης, προκειμένου να προβλεφθεί η αναμενόμενη πειραματική τιμή απαιτείται ένας μετασχηματισμός της ευθείας (στροφή και κατακόρυφη μετατόπισή της), ώστε να προκύψει η διχοτόμος του $1^{ου}$ τεταρτημόριου, όπως φαίνεται στο **σχήμα 5**.
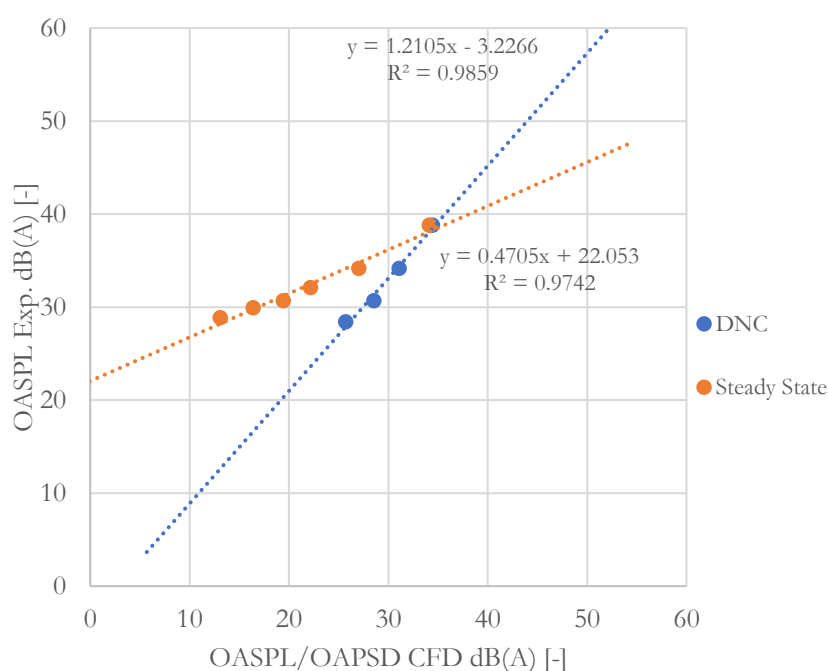


**Σχήμα 4:** *Βαθμονόμηση των υπολογιστικών μοντέλων του [36] (μπλε) και της παρούσας διπλωματικής εργασίας (πορτοκαλί) με τις πειραματικές μετρήσεις του [36].*

$y = 1.2105x - 3.2266$
$R^2 = 0.9859$

$y = 0.9999x + 0.0013$
$R^2 = 0.9742$
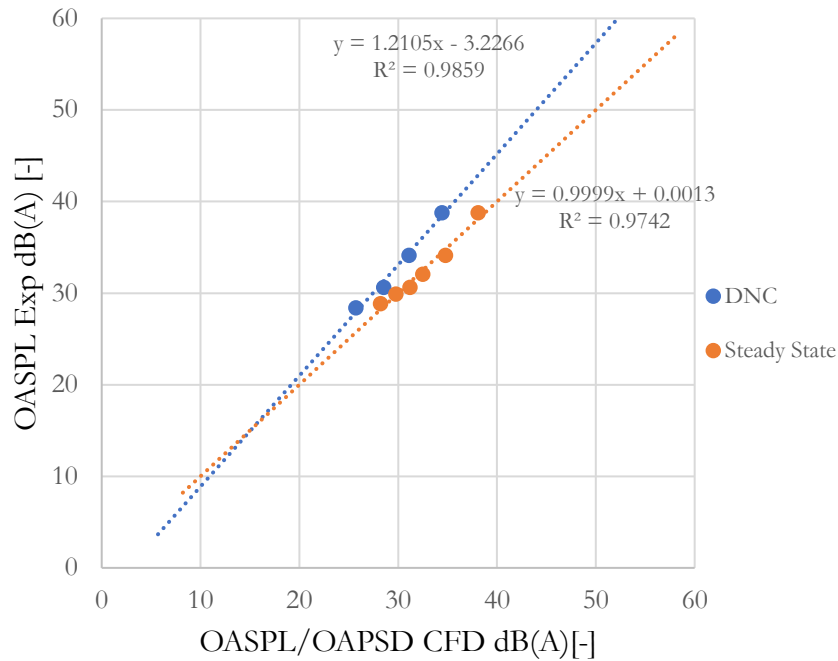
**Σχήμα 5:** Μετασχηματισμός της ευθείας του χρονικά μόνιμου υπολογιστικού μοντέλου.

# 5 Ανασχεδιασμός Αγωγού για Μείωση Θορύβου

Το μοντέλο που προτείνεται στη διπλωματική εργασία επιτρέπει την οπτικοποίηση των πηγών θορύβου, βοηθώντας τον μηχανικό να εντοπίσει τους μηχανισμούς παραγωγής ακουστικής ισχύος και μετέπειτα να επέμβει στον σχεδιασμό του αγωγού ώστε να μειώσει την ηχητική εκπομπή. Η δυνατότητα οπτικοποίησης προσφέρεται τόσο σε μορφή πεδίου σύμφωνα με τον ογκικό όρο της ακουστικής αναλογίας του Proudman, όσο και πάνω στην επιφάνεια της γεωμετρίας.

Παρατηρώντας τα εξαγόμενα πεδία των προσομοιώσεων, διαπιστώνεται πως η κάθετη ακμή αξονικής συμμετρίας (δακτύλιος) που καταδεικνύεται από το βέλος στο **σχήμα 6**, διαδραματίζει ισχυρό αρνητικό ρόλο στην παραγωγή ακουστικής ισχύος. Για τον λόγο αυτό, δοκιμάστηκε η αφαίρεση του στοιχείου αυτού από τη γεωμετρία, όπως φαίνεται στο **σχήμα** 7.
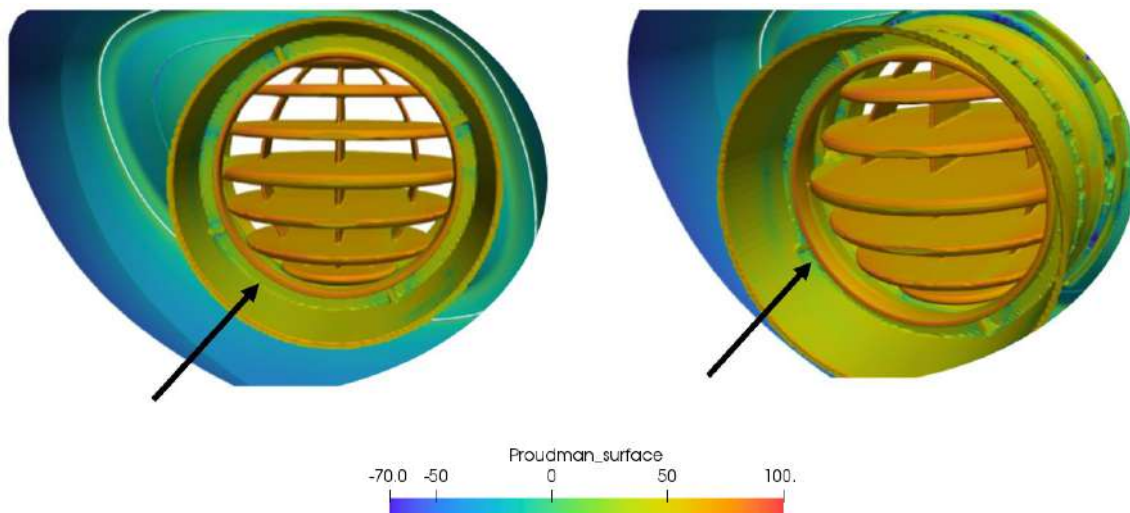


**Σχήμα 6:** Οπτικοποίηση της ακουστική ισχύος κατά Proudman πάνω στην επιφάνεια του αγωγού. Διακρίνεται ο δακτύλιος και η επίδρασή του στην παραγωγή θορύβου.

**Σχήμα 7:** Αρχικό περίβλημα των πτερυγίων του αγωγού (αριστερά) σε σύγκριση με το ανασχεδιασμένο από το οποίο απουσιάζει ο δακτύλιος (δεξιά).

Η αφαίρεση του δακτυλίου αυξάνει τη διατομή στην είσοδο των κατευθυντικών πτερυγίων του αγωγού, οδηγώντας στη μείωση του μέτρου της ταχύτητας ως συνέπεια της εξίσωσης συνέχειας. Καθώς η ακουστική ισχύς είναι ανάλογη του αριθμού Mach στην 5η δύναμη, η μείωση του συνολικού θορύβου γίνεται αισθητή (**σχήμα 8**).
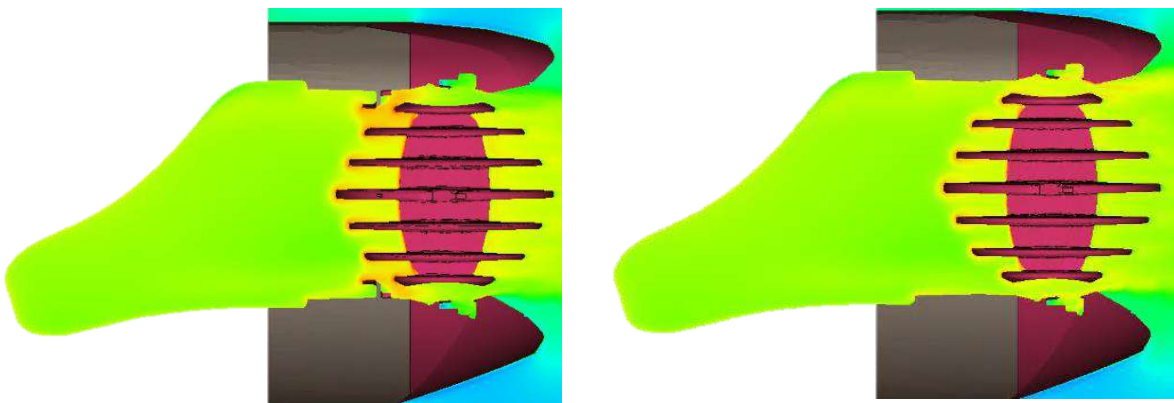


**Σχήμα 8:** Πεδίο ακουστικής ισχύος κατά Proudman στο επίπεδο συμμετρίας. Συνολική μείωση τις ακουστικής ισχύος στην είσοδο των κατευθυντικών πτερυγίων.

# 6  Πειραματικές Μετρήσεις

Στο πλαίσιο της διπλωματικής εργασίας, πραγματοποιήθηκε σειρά από πειραματικές μετρήσεις διαφόρων αγωγών επιβατικών αυτοκινήτων της Toyota, προκειμένου να διερευνηθεί κατά πόσο δύναται να γενικευθούν για διάφορες γεωμετρίες και συνθήκες εισόδου τα αποτελέσματα της βαθμονόμησης του χρονικά μόνιμου υπολογιστικού μοντέλου. Οι αγωγοί μετρήθηκαν απομονωμένοι από το πλαίσιο του αυτοκινήτου, εντός ανηχοϊκού θαλάμου. Στο **σχήμα 9** παρουσιάζεται η σχηματική αναπαράσταση της πειραματικής διάταξης.
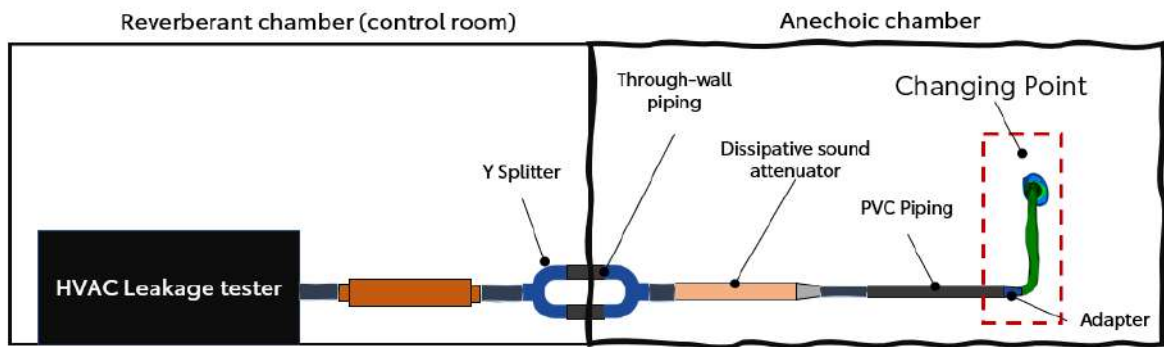
**Σχήμα 9:** Πειραματική διάταξη για τη μέτρηση του αεροδυναμικά επαγόμενου θορύβου εντός αγωγών κλιματισμού επιβατικών αυτοκινήτων.

Για τη μέτρηση έγινε χρήση 4 πολυκατευθυντικών μικροφώνων, όπως καταδεικνύεται στο **σχήμα 10**. Η τοποθέτησή τους και η ευθυγράμμιση της γεωμετρίας πραγματοποιήθηκε με χρήση laser (**σχήμα 11**).



● Microphone locations
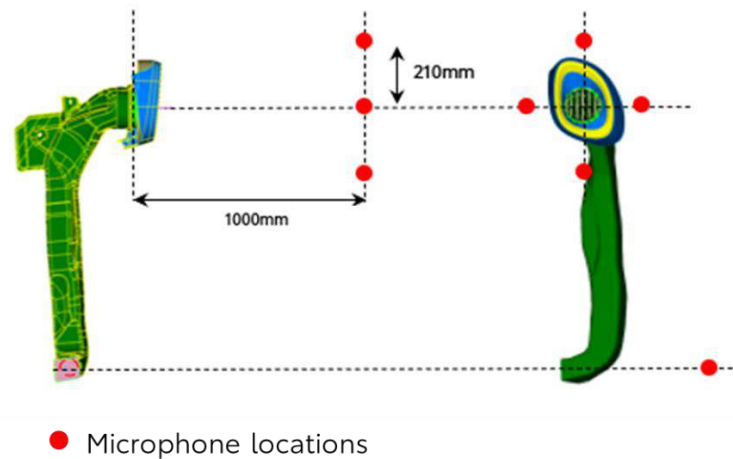
**Σχήμα 10:** Τοποθέτηση των μικροφώνων κατάντι του αγωγού.



**Σχήμα 11:** Ευθυγράμμιση της πειραματικής γεωμετρίας και των μικροφώνων με χρήση laser.

Προκειμένου να συγκριθούν ορθότερα τα υπολογιστικά με τα πειραματικά αποτελέσματα, μετρήθηκε ο θόρυβος βάθους της διάταξης του πειράματος, δηλαδή ο συνολικός θόρυβος που υπάρχει στην περιοχή όταν δε λειτουργεί η ηχητική πηγή του ενδιαφέροντος της μέτρησης. Ο τελευταίος παράγεται κυρίως από τη συσκευή παροχής αέρα αλλά και από τον αεροδυναμικό θόρυβο που δημιουργείται εντός των σωληνώσεων που δεν αποτελούν μέρος του αγωγού του αυτοκινήτου, τα οποία ασφαλώς δεν λαμβάνονται υπόψη και στο υπολογιστικό μοντέλο.

Τέλος, πραγματοποιήθηκαν μετρήσεις του αγωγού εντός της καμπίνας, τα αποτελέσματα των οποίων δεν επιτράπηκε να δημοσιευθούν.

# 7 Βαθμονόμηση του Μόνιμου Μοντέλου με Νέες Πειραματικές Μετρήσεις

Τα πειραματικά δεδομένα που αποκτήθηκαν σε αυτήν τη διπλωματική εργασία δέχονται κατάλληλη επεξεργασία, ώστε να συγκριθούν με τα υπολογιστικά. Προκειμένου να επιτευχθεί η κατά το δυνατόν ορθότερη μεθοδολογία, επιλέγεται η χρήση των δεδομένων εντός του φάσματος συχνοτήτων $125 - 5000\ Hz$, περιοχή που αφορά κυρίως τον αερακουστικό θόρυβο. Ακόμη, αφαιρέθηκε ο θόρυβος βάθους από τις πειραματικές μετρήσεις, καθώς η επίδρασή τους στα αποτελέσματα είναι κάθε άλλο παρά αμελητέα. Παράδειγμα αυτής της επίδρασης παρουσιάζεται στο **σχήμα 12**.
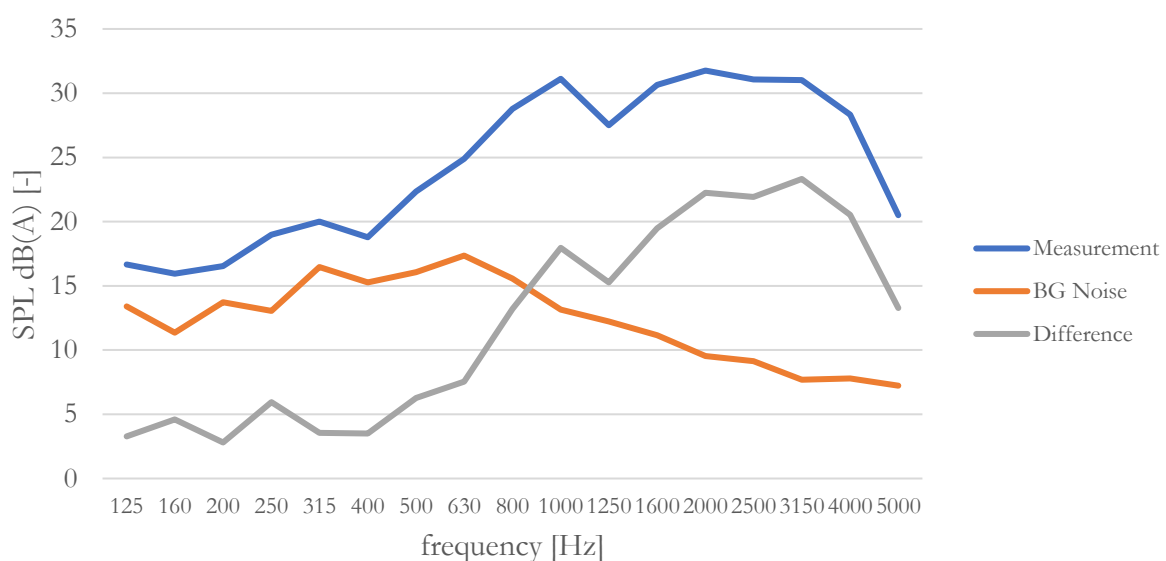


**Σχήμα 12:** *Άμεση σύγκριση μεταξύ του φάσματος του 1/3 της οκτάβας για τη συνολική πειραματική διάταξη, του μετρούμενου θορύβου βάθους και της σχετικής τους διαφοράς για συγκεκριμένη γεωμετρία πειράματος και παροχή όγκου.*

Γίνεται επιμέρους μελέτη της ακρίβειας των αποτελεσμάτων του υπολογιστικού μοντέλου με χρήση του ογκικού και του επιφανειακού όρου της αναλογίας του Proudman, όπου διαπιστώνεται η υπεροχή του δεύτερου, γεγονός που αναμενόταν για εφαρμογές χαμηλών ταχυτήτων. Το διάγραμμα της βαθμονόμησης για το σύνολο των αγωγών που μετρήθηκαν φαίνεται στο **σχήμα 13**, απ' όπου εξάγονται οι συντελεστές της γραμμικής συσχέτισης και του αλγεβρικού μετασχηματισμού.
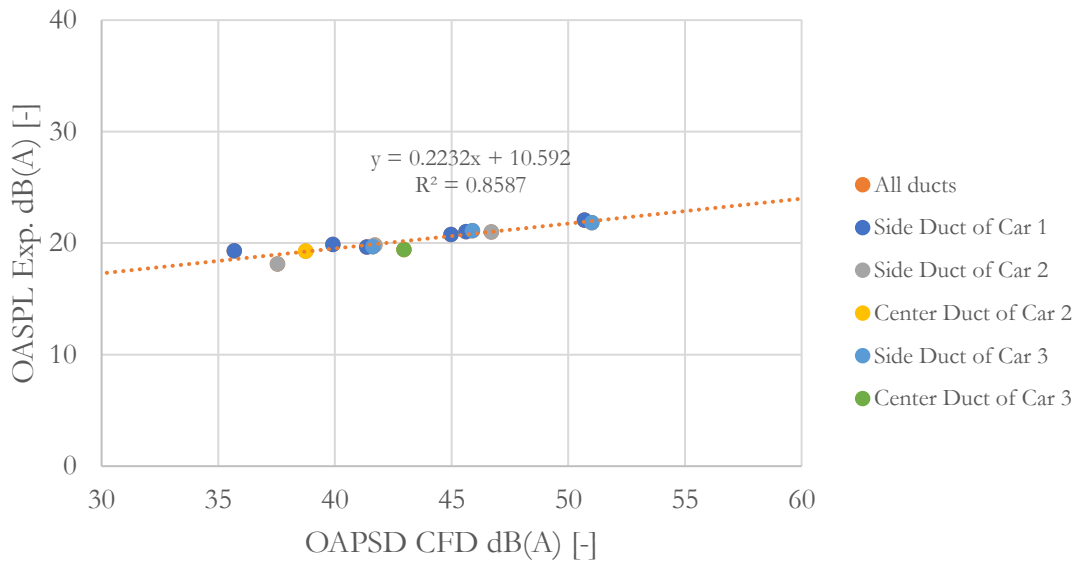
**Σχήμα 13:** Βαθμονόμηση του επιφανειακού όρου κατά Proudman με χρήση πειραματικών μετρήσεων.

Σχολιάζονται οι αποκλίσεις του υπολογιστικού μοντέλου από την πραγματικότητα κατά απόλυτη τιμή για κάθε περίπτωση, όπου και διαπιστώνεται μέγιστη απόκλιση της τάξης του $1.1 \, dB$ (**σχήμα 14**).
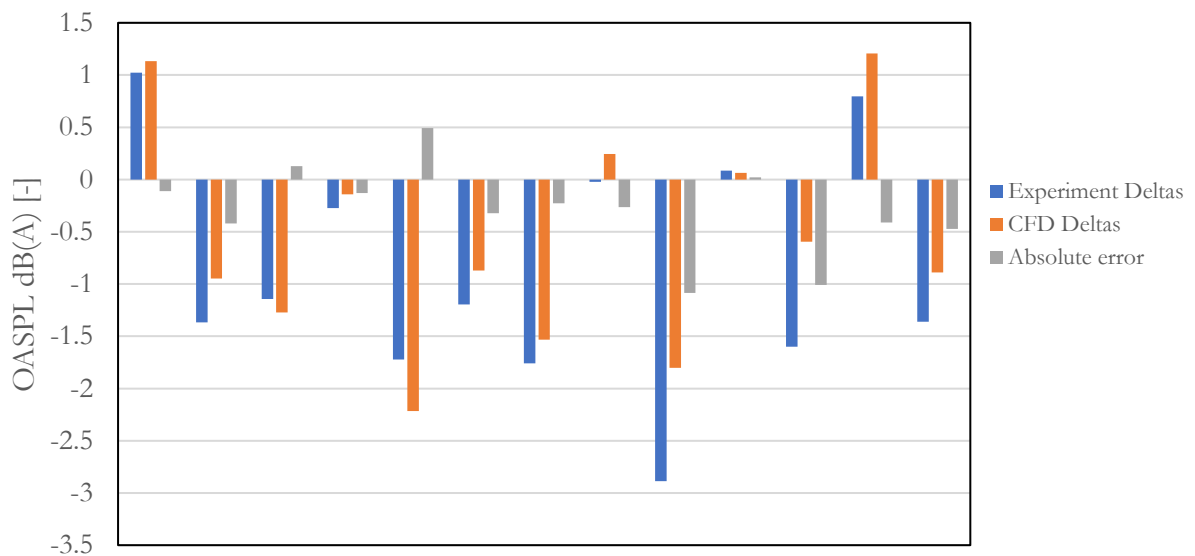


**Σχήμα 14:** Απόλυτες διαφορές για το πείραμα και το υπολογιστικό μοντέλο σε σύγκριση με τον πλαϊνό αγωγό του αυτοκινήτου 1 στην ονομαστική παροχή όγκου για τον επιφανειακό όρο κατά Proudman.

# 8 Συμπεράσματα

Αναπτύχθηκε μοντέλο μη-μόνιμων χρονικών εξισώσεων για την πρόλεξη του αεροδυναμικά επαγόμενου θορύβου, βασιζόμενο στην ακουστική αναλογία του Proudman. Επιτεύχθηκε σημαντική μείωση του υπολογιστικού κόστους σε σχέση με τη μέθοδο που αναπτύχθηκε και χρησιμοποιήθηκε στο [36] για τον ίδιο σκοπό, καθώς ο πραγματικός χρόνος προσομοίωσης ελαττώθηκε από περίπου 4 μέρες σε μόλις 1.5 ώρα σε 512 πυρήνες. Το προτεινόμενο μοντέλο προσφέρει στον μηχανικό τη δυνατότητα να αξιολογήσει ταχύτατα την αερακουστική επίδοση μιας δοσμένης γεωμετρίας, γεγονός εξαιρετικά χρήσιμο σε εφαρμογές καθημερινής συχνότητας.

Παρουσιάστηκε μια μέθοδος οπτικοποίησης των πηγών θορύβου, με χρήση της οποίας ανασχεδιάστηκε ο αρχικός αγωγός, επιτυγχάνοντας τη μείωση του θορύβου κατά 1.14 dBA σύμφωνα με τις πειραματικές μετρήσεις. Τέλος, η ακρίβεια του μόνιμου μοντέλου σε σύγκριση με τις πειραματικές μετρήσεις ανέρχεται σε απόκλιση μόλις 1.1 dB, το οποίο θεωρείται επαρκώς ικανοποιητικό.

# Bibliography

[1]  Amundsen, A., & Sagberg, F. (2003). *Hours of service regulations and the risk of fatigue-and sleep-related road accidents – A literature review.* [online] Available at: https://www.toi.no/getfile.php?mmfileid=5009.

[2]  Antares 2.2.0 Documentation (2024). *Ffowcs Williams & Hawkings Analogy.* [online] Available at: https://cerfacs.fr/antares/src/api/fwh/fwh.html#description.

[3]  Babisch, W. (2000). *Traffic Noise and Cardiovascular Disease: Epidemiological Review and Synthesis.* Noise Health, 2(8), 9-32. PMID: 12689458.

[4]  Bailly, C., Bogey, C., & Marsden, O. (2010). *Progress in direct noise computation.* International Journal of Aeroacoustics, 9(1-2), 123–143. [online] Available at: https://doi.org/10.1260/1475-472X.9.1-2.123.

[5]  CFD direct (2020). *The Architects of OpenFOAM.* [online] Available at: https://cfd.direct

[6]  CFD-Wiki, the free CFD reference (2014). *Standard K-Epsilon Model.* Cfd-Online.com. [online] Available at: www.cfd-online.com/Wiki/Standard_k-epsilon_model.

[7]  CFD-Wiki, the free CFD reference (2016). *SIMPLE Algorithm.* Cfd-Online.com. [online] Available at: http://www.cfd-online.com/Wiki/SIMPLE_algorithm.

[8]  Clark, C., & Stansfeld, S. A. (2007). *The Effect of Transportation Noise on Health and Cognitive Development: A Review of Recent Evidence.* International Journal of Comparative Psychology, 20(2). [online] Available at: https://doi.org/10.46867/ijcp.2007.20.02.10.

[9]  Croaker, P., Skvortsov, A., & Kessissoglou, N. (2011). *A Simple Approach to Estimate Flow-Induced Noise from Steady State CFD Data.* [online] Available at: https://www.acoustics.asn.au/conference_proceedings/AAS2011/papers/p54.pdf.

[10] Curle, N. (1955). *The influence of solid boundaries upon aerodynamic sound.* Proceedings of the Royal Society of London, 231(1187), 505–514. [online] Available at: https://doi.org/10.1098/rspa.1955.0191.

[11] Fahy, F. (2001). *Foundations of engineering acoustics.* Academic, 98–103, 406–410. ISBN: 0122476654.

[12] Glegg, S (2017). *Aeroacoustics of Low Mach Number Flows: Fundamentals, Analysis and Measurement.* Academic Press Elsevier, 2017, pp. 76, 89–90, 254–261, isbn: 9780128096512. doi: 10.1016/b978-0-12-809651-2.00011-4.

[13] Glegg, S., & Devenport, W. (2017). *Measurement, signal processing, and uncertainty.* ScienceDirect; Academic Press. [online] Available at: https://www.sciencedirect.com/science/article/abs/pii/B9780128096512000114?via%3Dihub.

[14] Goldstein, M. E. (2003). *A Generalized Acoustic Analogy. Journal of Fluid Mechanics*, 488, 315–333. [online] Available at: https://doi.org/10.1017/s0022112003004890.

[15] Hardin, J. C., & Hussaini, M. Y. (2012). *Computational Aeroacoustics*. Springer, 52–54. ISBN: 9781461383444. [online] Available at: https://doi.org/10.1007/978-1-4613-8342-0.

[16] Haworth, N. (1998). *Fatigue and fatigue research: The Australian experience*. Accident Research Centre. [online] Available at: https://www.monash.edu/muarc/archive/our-publications/papers/fatigue.

[17] He, Y., Schröder, S., Shi, Z., & et al. (2020). *Wind noise source filtering and transmission study through a side glass of DrivAer model*. Applied Acoustics, 160, 107161. [online] Available at: https://doi.org/10.1016/j.apacoust.2019.107161.

[18] Hiramatsu, K., Yamamoto, T., Taira, K., Ito, A., & Nakasone, T. (1997). *A survey on health effects due to aircraft noise on residents living around Kadena Air Base in the Ryukyus*. Journal of Sound and Vibration, 205(4), 451–460. [online] Available at: https://doi.org/10.1006/jsvi.1997.1011.

[19] Howe, M. S., & Feit, D. (1999). *Acoustics of Fluid–Structure Interactions*. Physics Today, 52(12), 64–64. [online] Available at: https://doi.org/10.1063/1.882913.

[20] Kalitzin, G., Medic, G., Iaccarino, G., & Durbin, P. (2005). *Near-wall behavior of RANS turbulence models and implications for wall functions*. Journal of Computational Physics, 204(1), 265–291.

[21] Kaltenbacher, M. (2018). *Computational Acoustics*. Springer International Publishing, 22–23, 251. ISBN: 978-3-319-59038-7. [online] Available at: https://doi.org/10.1007/978-3-319-59038-7.

[22] Khalighi, Y., Mani, A., Ham, F., et al. (2010). *Prediction of sound generated by complex flows at low Mach numbers*. AIAA Journal, 48(2), 306–316. [online] Available at: https://doi.org/10.2514/1.42583.

[23] Kinsler, L. E., & Frey, A. R. (1951). *Fundamentals of Acoustics*. American Journal of Physics, 19(4), 254–255. [online] Available at: https://doi.org/10.1119/1.1932798.

[24] Kolmogorov, A. N. (1941). *The Local Structure of Turbulence in Incompressible Viscous Fluid for Very Large Reynolds Numbers*. Doklady Akademii Nauk SSSR, 30, 301-305.

[25] Koutsantonis, P. (2018). *Application of the Continuous Adjoint Method for the Aerodynamic Optimization of a Passenger Car*. Dilpoma Theshs, School of Mechancial Engineering, NTUA. [online] Available at: http://velos0.ltt.mech.ntua.gr/kgianna/diplomat/fp/koutsantonis.pdf.

[26] Landau, L. D. (1987). *Fluid Mechanics: Volume 6* (Course of Theoretical Physics S). Butterworth-Heinemann.

[27] Landström, U. (1990). *Noise and fatigue in working environments*. Environment International, 16(4-6), 471–476. [online] Available at: https://doi.org/10.1016/0160-4120(90)90015-x.

[28]Launder, B., & Hanjalic, K. (2011). *Modelling Turbulence in Engineering and the Environment: Second-Moment Routes to Closure.* Cambridge University Press, United Kingdom.

[29]Launder, B. E., & Spalding, D. B. (1974). *The numerical computation of turbulent flows.* Computer Methods in Applied Mechanics and Engineering, 3(2), 269–289. [online] Available at: https://doi.org/10.1016/0045-7825(74)90029-2.

[30]Lighthill, M. J. (1952). *On sound generated aerodynamically I. General theory.* Proceedings of the Royal Society of London. Series A. Mathematical and Physical Sciences, 211(1107), 564–587. [online] Available at: https://doi.org/10.1098/rspa.1952.0060.

[31]Liu, F. (2016). *A thorough description of how wall functions are implemented in OpenFOAM.* In proceedings of CFD with openSource software.

[32]Martínez-Lera, P., Hallez, R., Bériot, H., & et al. (2012). *Computation of sound in a simplified HVAC duct based on aerodynamic pressure.* In 18th AIAA/CEAS Aeroacoustics Conference (33rd AIAA Aeroacoustics Conference). American Institute of Aeronautics and Astronautics. [online] Available at: https://doi.org/10.2514/6.2012-2070.

[33]Martínez-Lera, P., Hallez, R., Tournour, M., & et al. (2011). *Improved simulation technique for predicting the noise radiated by a flap in a simplified HVAC duct.* In JSAE Annual Congress, 20115259, 20.

[34]Martínez-Lera, P., Kucukcoskun, K., Shur, M., & et al. (2016). *Hybrid aeroacoustic computations for flows in ducts with single and tandem diaphragms.* In 22nd AIAA/CEAS Aeroacoustics Conference. American Institute of Aeronautics and Astronautics. [online] Available at: https://doi.org/10.2514/6.2016-2796.

[35]Martínez-Lera, P., Schram, C., Bériot, H., & et al. (2014). *An approach to aerodynamic sound prediction based on incompressible-flow pressure.* Journal of Sound and Vibration, 333(1), 132–143. [online] Available at: https://doi.org/10.1016/j.jsv.2013.08.033.

[36]Mikedis, K. (2023). *Prediction of Aerodynamically Induced Noise in Automotive HVAC Systems.* Diploma Thesis, School of Mechanical Engineering, NTUA. [online] Available at: http://velos0.ltt.mech.ntua.gr/kgianna/diplomat/fp/mikedis.pdf.

[37]Morteza, M., Asouti, V., Trompoukis, X., Tsiakas, K. & Giannakoglou, K. C. (2023). *Aeroacoustic and Aerodynamic Adjoint-Based Shape Optimization of an Axisymmetric Aero-Engine Intake.* Aerospace, 10(9), pp.743–743. [online] Available at: https://doi.org/10.3390/aerospace10090743.

[38]NASA. (1996). *Acoustic Noise Requirement.* Preferred Reliability Practices. [online] Available at: https://www.klabs.org/DEI/References/design_guidelines/design_series/1259.pdf.

[39]OpenFOAM: User Guide: OpenFOAM®. (2024). [online] Available at: https://www.openfoam.com/documentation/guides/v2112/doc/.

[40]Patankar, S. (1980). *Numerical Heat Transfer and Fluid Flow.* Taylor & Francis.

[41]ParaView. (2018). [online] Available at: https://www.paraview.org/.

[42] Phillips, O. M. (1960). *On the generation of sound by supersonic turbulent shear layers*. Journal of Fluid Mechanics, 9, 1-28.

[43] Pierce, A. D. (2019). *Acoustics*. Springer-Verlag GmbH, 93–101, 395, 400. ISBN: 978-3-030-12395-8.

[44] Pierce, A. D., & Saunders, H. (1984). *Acoustics: An Introduction to Its Physical Principles and Applications*. Journal of Vibration and Acoustics, 106(3), 322–323.

[45] Pletcher, R.H., Tannehill, J.C., & Anderson, D. (1997). *Computational Fluid Mechanics and Heat Transfer, Second Edition*. Series in Computational and Physical Processes in Mechanics and Thermal Sciences. Taylor & Francis.

[46] Proudman, I. (1952). *The generation of noise by isotropic turbulence*. Proceedings of the Royal Society of London, 214(1116), 119–132. [online] Available at: https://doi.org/10.1098/rspa.1952.0154.

[47] Ramírez, A. W., & Wolf, W. R. (2015). *Effects of Trailing Edge Bluntness on Airfoil Tonal Noise at Low Reynolds Numbers*. Journal of the Brazilian Society of Mechanical Sciences and Engineering, 38(8), 2369–2380. [online] Available at: https://doi.org/10.1007/s40430-015-0308-6.

[48] Rossing, T. D. (Ed.). (2014). *Springer Handbook of Acoustics (2nd ed.)*. Springer. ISBN: 978-1-4939-0754-0. [online] Available at: https://doi.org/10.1007/978-1-4939-0755-7.

[49] Safe Acoustics (2021). *Frequency of Sound» Acoustic Consultancy» Noise Report» Acoustics*. Safe Acoustics. https://www.safeacoustics.com/frequency-of-sound/.

[50] Schmitt, F. G. (2007). *About Boussinesq's turbulent viscosity hypothesis: historical remarks and a direct evaluation of its validity*. Comptes Rendus Mécanique, 335(9-10), 617–627.

[51] Skvortsov, A., Gaylor, K., Norwood, C., Anderson, B., & Chen, L. (2009). *Scaling laws for noise generated by the turbulent flow around a slender body*. In Undersea Defence Technology: UDT Europe 2009, pp. 182–186.

[52] Sondak, D. L. (1992). *Wall functions for the k-ε turbulence model in generalized nonorthogonal curvilinear coordinates*. Retrospective Theses and Dissertations, 9954.

[53] Strykowski, P. J., & Sreenivasan, K. R. (1990). *On the formation and suppression of vortex "shedding" at low Reynolds numbers*. Journal of Fluid Mechanics, 218, 71. [online] Available at: https://doi.org/10.1017/s0022112090000933.

[54] Van Herpe, F., Vergne, S., & Gaudard, E. (2012). *Wavenumber-frequency analysis of the wall pressure fluctuations in the wake of a rear view mirror using a Lattice Boltzmann model*. In Acoustics 2012, S. F. d'Acoustique, Ed., Nantes, France. [online] Available at: https://hal.archives-ouvertes.fr/hal-00810780.

[55] van Kempen, E. E. M. M., Kruize, H., Boshuizen, H. C., Ameling, C. B., Staatsen, B. A. M., & de Hollander, A. E. M. (2002). *The association between noise exposure and blood pressure and*

*ischemic heart disease: a meta-analysis.* Environmental Health Perspectives, 110(3), 307–317. [online] Available at: https://doi.org/10.1289/ehp.02110307.

[56]Wagner, C., Hüttl, T., & Sagaut, P. (2007). *Large-Eddy Simulation for Acoustics.* Cambridge University Press, 9-11, 30-32, 130. ISBN: 978-0-521-87219-6.

[57]*Wall functions.* (n.d.). Introduction to CFD. [online] Available at: https://cfd.blogs.upv.es/turbulence/wall-functions/.

[58]Wikipedia Contributors. (2019). *K-epsilon turbulence model.* Wikipedia; Wikimedia Foundation. [online] Available at: https://en.wikipedia.org/wiki/K-epsilon_turbulence_model.

[59]Γιαννάκογλου, Κ.Χ. (2004). *Συνεκτικές Ροές στις Στροβιλομηχανές (2nd ed.).* Εκδόσεις ΕΜΠ.

[60]Τσαγγάρης, Σ. (2015). *Μηχανική των Ρευστών.* Εκδόσεις Τσότρας.

[61]Φυκούρας, Π. (2020). *Βελτιστοποίηση Ανεμοθώρακα Αγωνιστικής Μοτοσυκλέτας για Μείωση της Οπισθέλκουσας με χρήση της Συνεχούς Συζυγούς Μεθόδου.* Διπλωματική Εργασία, Σχολή Μηχανολόγων Μηχανικών, ΕΜΠ. [online] Available at: http://velos0.ltt.mech.ntua.gr/kgianna/diplomat/fp/fykouras.pdf.